Department of Precision and Microsystems Engineering

TITLE: STUDIES TOWARDS THE DEVELOPMENT OF A DEVICE FOR THE RAMAN CHARACTERISATION OF THE SARS-CoV-2 ANTIBODY

NAME: EHIKHIOYA IJEMUDIA INNOCENT

Report no : 2021.023
Coach : Urs Staufer
Professor : Urs Staufer
Specialisation : Dynamics and Nanoscience
Type of report : Master Thesis
Date : 31st March 2021

MSc Thesis in the Micro and Nanosystems Engineering Group,
Precision and Microsystems Engineering.
Technical University of Delft.

Studies towards the development of a device for Raman Characterisation of the SARS-CoV-2 Antibody

Ehikhioya Ijemudia Innocent
2021

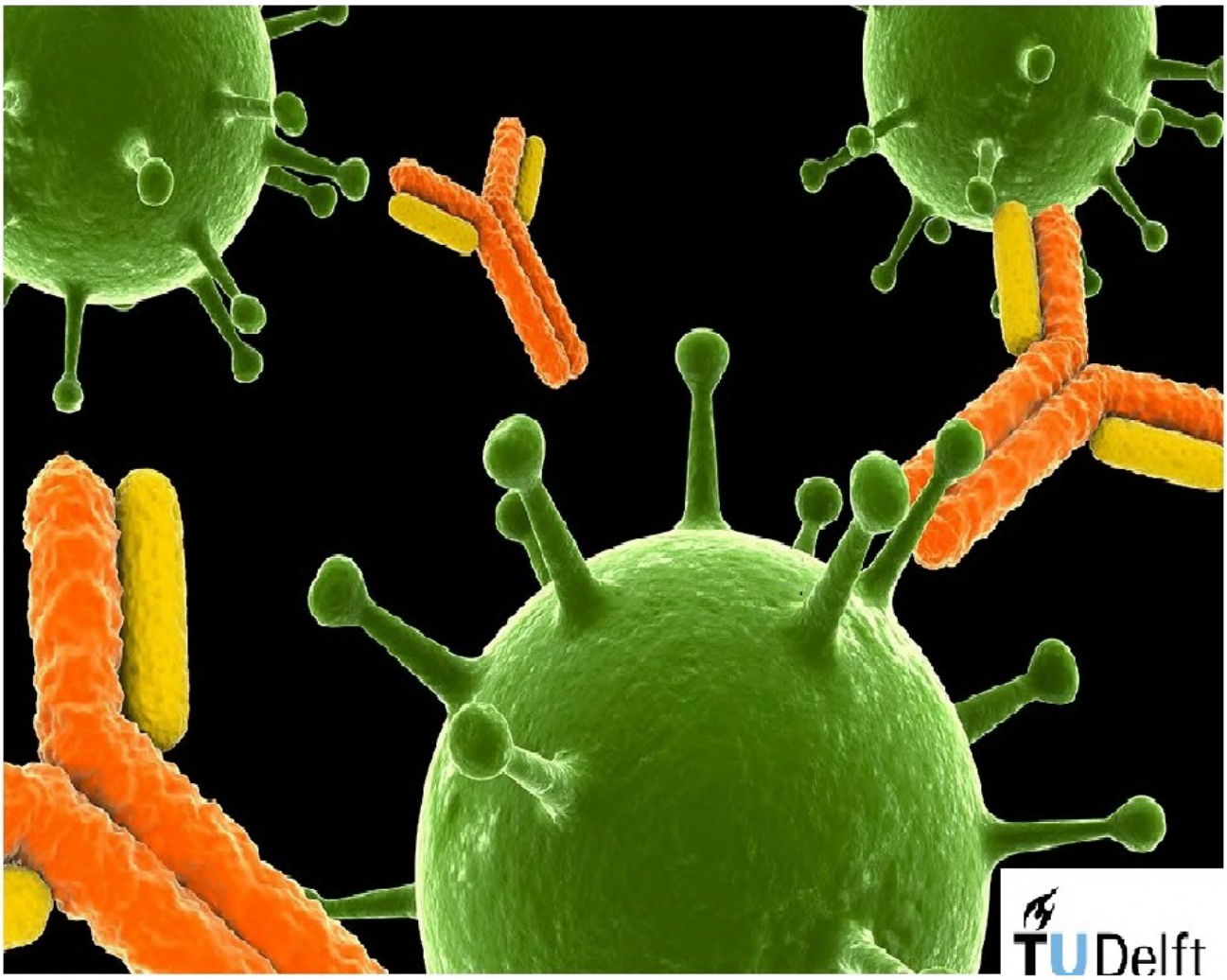

STUDIES TOWARDS THE DEVELOPMENT OF A DEVICES FOR RAMAN CHARACTERIZATION OF SAR-COV-2 ANTIBODY

A thesis submitted to the Delft University of Technology in partial fulfillment of the requirements for the degree of

Master of Science in Precision and Microsystems Engineering
Faculty of Mechanical, Maritime and Materials Engineering

by

Ehikhioya Ijemudia Innocent

March 2021

Ehikhioya Ijemudia Innocent: *Studies towards the development of a devices for Raman Characterization of SAR-COV-2 Antibody* (2021)

ISBN ————

The work in this thesis was made in the:

Micro and Nanoscience Engineering
Department of Precision and Microsystems Engineering
Faculty of Mechanical,Maritime and materials
Delft University of Technology

Supervisors:	Prof.dr. Urs Staufer
Thesis Committee:	Ivan Bjuinsters
	Eduardo Mendes

ABSTRACT

Human Civilization is no stranger to infectious diseases, throughout the abundance of time infectious diseases, famine and wars have been a major threat to human existence and progress. These disease are caused by micrometer to nanometer sized microorganisms like bacteria, pathogens, and viruses. They are of various types, with each having its own unique effect on the infected host.

It becomes self evident that only early detection, quarantine and treatment of the infected can curtail a possible exonential growth rate of infections and the possibility of mutation of a given virus to a more virulent strain.

The emergence of SARS-CoV-2 in december 2019 has brought about a unified global effort to characterise and curtail the virus. This effort has met with some difficulties, the inability to contain the rapid spread of COVID-19 proceeds from the unavailability of simple, reliable, cheap and rapid testing methods. Lab based testing during epidemics cannot cater for the overwhelming number of test to be done.

In such a Pandemic situation, an interplay of the above situational dynamics, begs the need for very sensitive and efficient point of care device that simplifies diagnoses of SARs-CoV-2 virus. The WHO stipulates that all such point of care devices should meet with following standards: (i) affordable; (ii)sensitive; (iii) specific; (iv) user-friendly; (v) rapid and robust; (vi)equipment-free;and (vii) deliverable to end-users [St John and Price, 2014].

In this thesis, an immunoassay based on surface enhanced Raman spectroscopy (SERS) was used to investigate SARs-CoV-2 antibody for its characteristic Raman finger print.

Characterization of SERS substrate like Nanoporous gold, gold nanoparticles deposited on topaz and sputtered on borosilicate glass showed a decent enhancement factor of about 10^3 to 10^4, it was also observed on all SERS substrate that a 1μm height of deposited nanoparticles was sufficient for SERS enhancement.

The immobilization of the Genetex SARs-CoV-2 was done using Cysteamine hydrochloride and Lomants reagent, linkage was only possible only after sufficient cleaning was effected on the SERS substrates, the Raman spectrum obtained was same for both protocols, however noise and substrate instability was observed. The presence of Cysteamine Hydrochloride monolayers was confirmed by the Raman peaks $510, 643, 726, 938, 1015, 2557, 2928, and 2962 cm^{-1}$ each respectively assigned to $\nu(S-S), \nu(C-S), \nu(C-S), \nu(C-C(-N)), \nu(C-C(-N)), \nu(S-H), \nu_{as}(CH_2)$ and $\nu_2(CH_2)$ [Kudelski and Hill, 1999]. The characteristic disufide band, Aliphatic and Aromatic bands, Amide I and Amide III bands were identified for both linking protocols and tentatively assigned. since adsorption of the thiol monolayers was from solution a Langmuir growth model is proposed as the means of thiol growth and orientation.

ACKNOWLEDGEMENTS

In all humility I would like to acknowledge my deepest and warmest gratitude to Professor Urs Staufer, and Saleh Aghajani who is a PHD candidate in micro and nano-systems groups in the Precision and Microsystems engineering department of the faculuty of engineering in the Technical university of delft.

Professor Urs Staufer made this research possible for me, he was very objective and insightful from the first meeting. Weekly meetings with him were invaluable to me during experiments and in the thesis formulation and writeup.

Saleh Aghajani was also of immense help in obtaining SERS substrates for experiments, he suggestions on the best practice for SERS substrate characterisation were priceless, he also rendered guidance on how to measure optimally with the Raman spectrometer.

I am very grateful to the experts and lab support staff who facilitated me during experiments, they helped handle lots of nuances, they include: Ali Ahmadi Dastjerdi, Gideon Emmanuel, Rob Luttjeboer, and Patrick van Holst. Without their patience, participation and input, the experiments could not have been successfully conducted.

Finally, I solemnly express my sincere, heartfelt gratitude to my mother, brothers and sisters for the support and belief in me during the course of the course work and thesis project. My master study would not have been possible without them.

Ehikhioya Innocent

CONTENTS

LIST OF FIGURES

LIST OF TABLES

ACRONYMS

Abn Antibody

AbnAgn Antibody-Antigen Complex

1 INTRODUCTION

Through several centuries Infectious diseases, famines and wars have been a major threat to human existence and progress. The burden of infection is amplified in the light of new epidemics and re-merging once's. Detailed research into these emerging and re-emerging infections provide information on the dynamic connection between microorganisms, their hosts and their active environment, and also on the evolutionary nature of pathogenic microorganisms(possibility of mutation) [Morens et al., 2004]. Figure 1.1 show a the global spread of infectious disease phenomenon.

These infectious diseases are caused by micrometer to nanometer sized microorganisms like bacteria, pathogens, and viruses. They are of various types, with each having its own unique effect on the infected host[Basha et al., 2017]. Six years ago in 2014 the world was caught unawares with the outbreak of the Ebola and Zika viruses which claimed some ten thousand lives in sub-saharan african[Fauci and Morens, 2016; To et al., 2015].

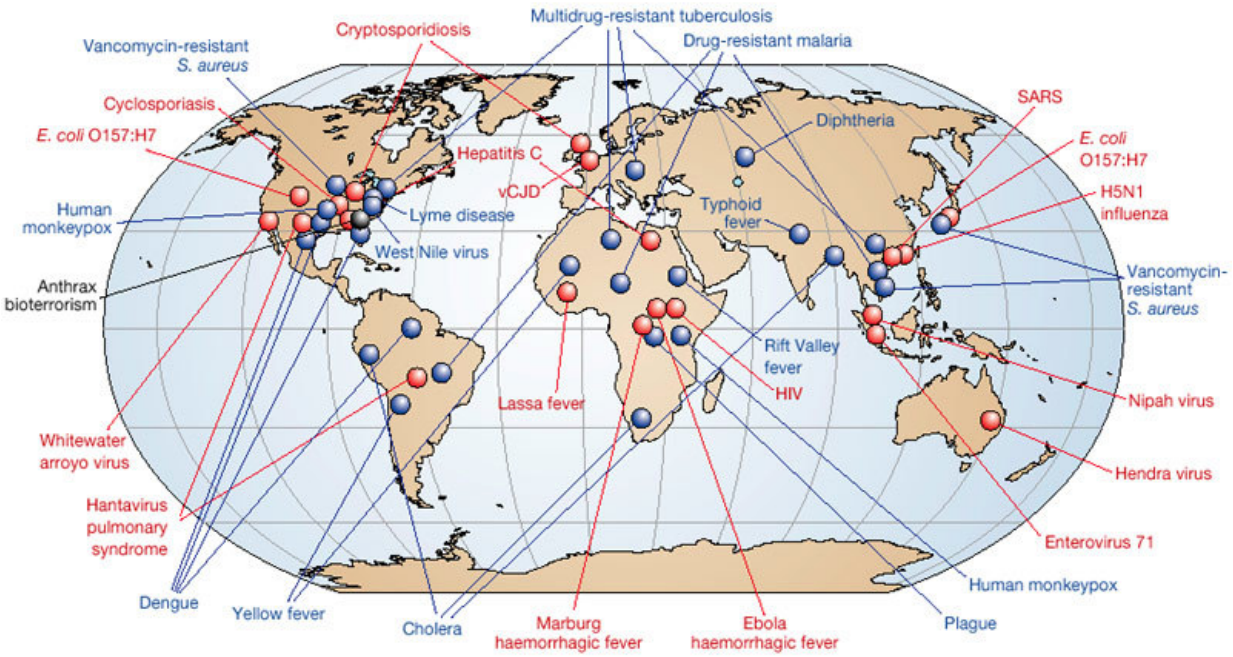

Figure 1.1: The Global Examples of Emerging(Red) and Re-Emerging Disease(Blue) [Fauci, 2001]

As can be inferred from Figure 1.2 infectious diseases are ubiquitous and indeed a global phenomenon with death toll of approximately 15 million (25%) of 57 million annual deaths worldwide [Morens et al., 2004]. It becomes self evident that only early detection, quarantine and treatment of the infected can curtail a possible exponential growth rate of infections and the possibility of mutation of a given virus to a more virulent strain is also reduced.

In both developed and the undeveloped world, infants and the elderly with their developing and weak immune system respectively are the most affected in the event of an epidemic. Butler et al. [2001].

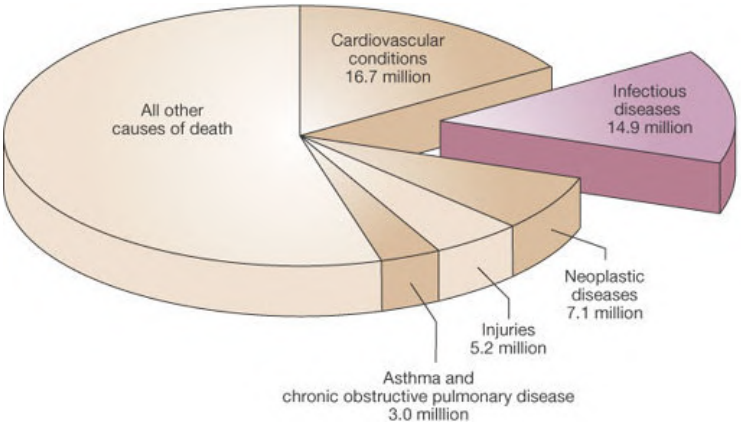

Infectious diseases	Annual deaths (million)
Respiratory infections	3.96
HIV/AIDS	2.77
Diarrhoeal diseases	1.80
Tuberculosis	1.56
Vaccine-preventable childhood diseases	1.12
Malaria	1.27
STDs (other than HIV)	0.18
Meningitis	0.17
Hepatitis B and C	0.16
Tropical parasitic diseases	0.13
Dengue	0.02
Other infectious diseases	1.76

Figure 1.2: Leading causes of death worldwide Zaat [2004]

Late December 2019, in the chinese city of wuhan, in Hubei province, a collection of people sick with pneumonia of unknown cause but similar in symptoms to patients with severe acute respiratory syndrome (acute respiratory syndrome (SARS)) and Middle East respiratory syndrome(Middle East respiratory syndrome (MERS)) [Zhu et al., 2020] was observed, patients exhibited symptoms including cough, fever, chest discomfort, and in severe cases dyspnea and bilateral lung infiltration[Zhu et al., 2020; Gralinski and Menachery, 2020].

The first twenty seven documented hospitalized patients were linked to Huanan Seafood Market, a wet market(for seafood, poultry and live animals) situated in downtown Wuhan. The genomic sequence of the offending virus was decoded and aided the International Committee on Taxonomy of Viruses International Committee on Taxonomy of Viruses (ICTV) to name the virus as Severe Acute Respiratory Syndrome Coronavirus 2 (SARS-CoV-2)(a sub-species of the Coronavirus) as the pathogen responsible for the disease. The World health organisation World Health Organisation (WHO) declared it a public health emergency of international concern Public health emergency of international concern (PHEIC) by January 2020, from December till October 2020 over 34million persons have been infected and a million deaths recored. Figure 1.3 shows a detailed chronology of events.[Hu et al., 2020]

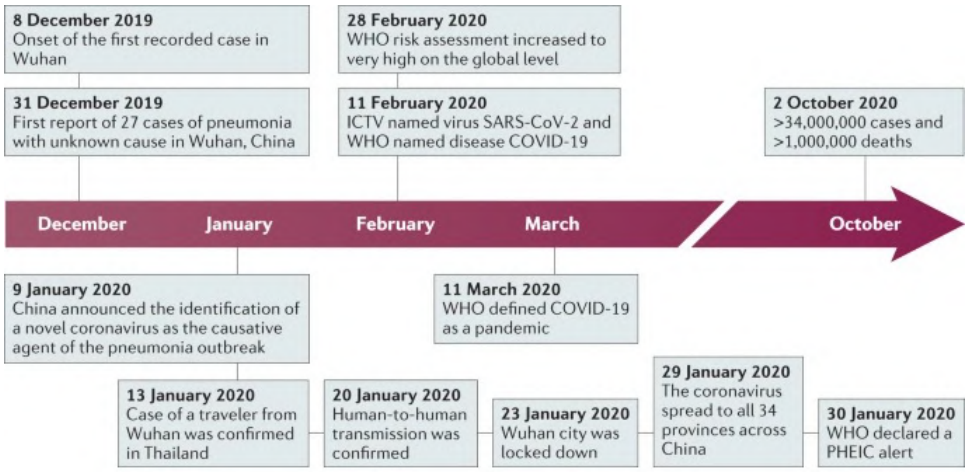

Figure 1.3: Timeline of the key events of the COVID-19 outbreak[Hu et al., 2020]

In a world of enhanced mobility and commerce the risk of a global pandemic becomes real with its consequent strain on medical personnel and health infrastructure. Nations are working around the clock trying to mitigate the spread of the virus by banning or limiting domestic and international travels, introducing social distancing protocols and quarantining citizens. Early testing of infected patients

as well as the general population is key to curbing the spread of the virus and its impact on the economy, testing also guides in understanding the effect of the pandemic and the risks it poses to different age groups within a population. The inability to contain the rapid spread of COVID-19 proceeds from the unavailability of simple, reliable, cheap and rapid testing methods.

Lab based testing during epidemics cannot cater for the overwhelming number of test to be done, lab personnel must transfer test samples from point of care Point of care (POC) to laboratories for testing, this is time consuming, and test result usually take about 24hours to be ready[Bissonnette and Bergeron, 2012]. In such a Pandemic situation, it is not uncommon for lab resource and equipment to stress or become unavailable[Hu et al., 2014]. An interplay of the above situational dynamics, begs the need for very sensitive and efficient POC device that simplifies diagnoses of disease pathogen and drastically improve throughput. The WHO stipulates that all such point of care devices should meet with following standards: (i) affordable; (ii) sensitive; (iii) specific; (iv) user-friendly; (v) rapid and robust; (vi)equipment-free; and (vii) deliverable to end-users [St John and Price, 2014].

Infectious diseases are transferred via contact with body fluid(saliva, blood, urine, spores from nasal and throat passages or stool) of an infected person. Analysis of a given disease pathogen can be achieved by several methods like Enzyme linked immunosorbent assay Enzyme linked Immuno-sorbent Assay (ELISA)[Guarrotxena et al., 2010], western blot, and immunoassay based on surface enhanced Raman spectroscopy Surface Enhanced Raman Spectroscopy (SERS)[Guarrotxena et al., 2010].

Surface enhanced raman spectroscopy involves the focusing of laser(light) on an analyte(pathogenic antigen),or antigen-antibody immunocomplex immobilized on a roughened gold or silver surface and collecting the enhance scatter raman signal, which contains information about specific bond vibration characteristics of the molecular structure of the antigen. The roughen gold and silver surface functions to to amplify the light signal at the surface of the substrate, hence very low Raman scatter signal are amplified by several orders of magnitude for detection.

1.1 CORONAVIRUSES

Coronaviruses were identified as human pathogens in the 1960s. They are enveloped positive stranded Ribonuclei acid Ribonuleic Acid (RNA) viruses in the order of Nidovirales[Davison, 2020]. Under an electron microscope the virions features a crown-like appearance, hence the viruses are called corona, meaning 'crown' or 'halo'.[ECDC, 2020]

Generally, birds, bats, and mammals acts as an intermediate host reservoir for coronaviruses, en-route to infecting humans. Figure 1.4 shows the classification of coronavirues in Order-family-Genus-Sub-Genus-Species and Sub-species. Of the seven coronaviruses known to infect humans(under species in Figure 1.4). Four of them (HCoV-OC43, HCoV-HKU1, HCoV-229E and HCoV-NL63)[Stadler et al., 2003] results in mild to moderate symptoms like cold and bronchiolitis in children[Yin and Wunderink, 2018]. The other three causes more severe health effects, SARS-CoV was responsible for the Severe Acute Respiratory Syndrome (SARS) in 2002, MERS-CoV the Middle East Respiratory Syndrome (MERS) in 2012 and SARS-CoV-2 for the COVID-19 pandemic in 2020.

1.2 STRUCTURE OF SARS-COV-2

The Coronavirus virion consist of four main structural proteins namely the spike (S), membrane (M), envelope (E), and nucleocapsid (N) proteins. The basic structure of

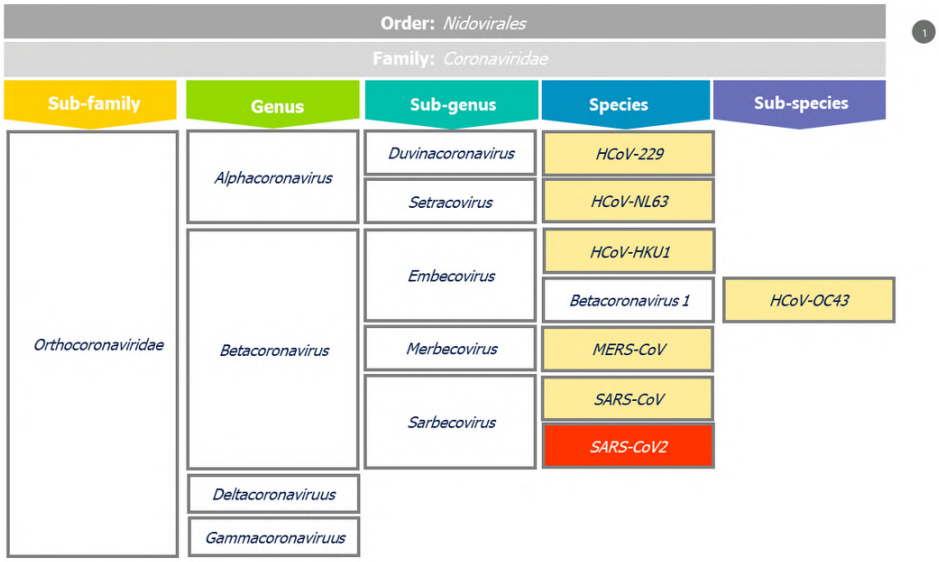

Figure 1.4: Human coronavirus taxonomy
[Davison, 2020]

the coronavirus virion is shown in Figure 1.5, and the main functions of the above named proteins are as follows:

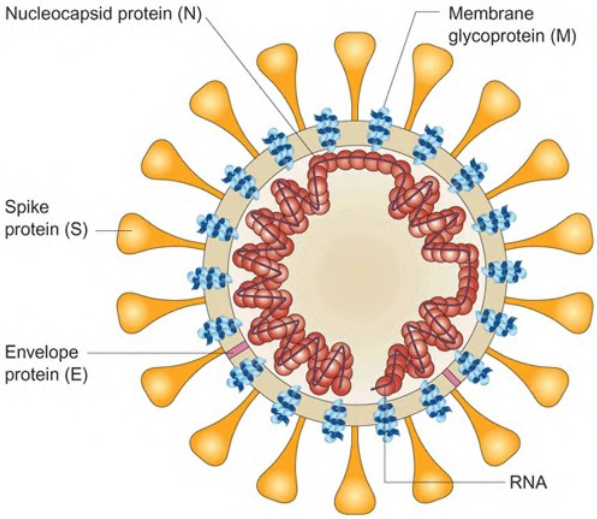

Figure 1.5: Morphology of the SARS-CoV-2 Virus [Stadler et al., 2003]

1. SPIKE (S) PROTEIN: The spike proteins expresses as three identical units of polypetides on the surface of the virus [Fehr and Perlman, 2015]. These proteins are responsible for receptor binding of the disease antigen with a host cell membrane, malignancy of the virus, pathogenicity and determining target-cell specificity[Lai, 2002], With a length of 20nm the S-proteins contains residues that neutralises the all-desirable antibody binding effect, hence antibodies are developed to surmount this opposition and bind with the S-protein.[Enjuanes et al., 1995]

2. MEMBRANE (M) PROTEIN: The M-protein is the most abundant structural protein in the virion. The M-protein expresses as a dimer that can adopt two conformations, in the process determining the shape of the virion. [Fehr and Perlman, 2015].

3. NUCLEOCAPSID (N) PROTEIN: The N-protein is the only protein present in the nucleocapsid (proteins associated with nucleic acid). It complexes with the Ribonucleic acid (RNA) and functions to enhance the efficiency of virus transcription and assembly [McBride et al., 2014].

4. ENVELOPE (E) PROTEIN: The E-protein is present in minute amounts inside the virus, the E protein functions to facilitate the assembly and release of viral RNA [Masters et al., 2006].

While in the Human lung the SARS-CoV-2 virus accesses host cells through the enzyme angiotensin-converting enzyme 2 Angiotensin-converting enzyme 2 (ACE-2).[Verdecchia et al., 2020] The virus uses the "spike" (peplomer) of the glycoprotein to connect to ACE2 and permeate host cell.[Letko et al., 2020] Some have suggested that the density of ACE2 in the lung correspond with the acuteness of the disease in the lung. The COVID 19 virus manifest by causing respiratory failure. The virus also affects gastrointestinal organs because ACE2 is also well expressed in the glandular cells of gastric, duodenal and rectal epithelium[Gu et al., 2020], as well as endothelial cells and enterocytes of the small intestine[Hamming et al., 2004]. Broadly speaking, infection appears to precipitate a chain of vasoconstrictive responses within the body, the event of constriction is viewed as the cause of oxygenation defect in addition to the presence of viral pneumonia[Wadman et al., 2020].

1.3 PROJECT GOAL

The goal of the afore-described literature review is the design of a cost-effective Rapid Virus Detection Assay for detecting COVID-19 using surface enhanced Raman spectroscopy (SERS). The assay will be performed on a microfluidic device, the virus antigen will complex with an appropriate antibody on this microfluidic device. Raman spectroscopy is proposed to be used for detection and identification of the different bond vibrations of proteins in the SARS-CoV-2 molecule.

1.4 REPORT STRUCTURE

The structure of this thesis report is aligned with the systematic analysis procedure. Chapter one details the origins of viruses and disease as well as its prevalence, the structure of the SARS-CoV-2 is also discussed. Chapters 2 to 6 presents the theoretical basis upon which the investigation was conducted. In Chapter 2 the nature of antibody's and antigen is reviewed, immnunoreactions is also discussed. Chapter 3 contains information about Raman Spectroscopy, Raman scattering, penetration peculiarities and instrumentation are aptly presented. The chapter ends with a discussion of SERS substrate and the effects of distance on SERS enhancement. Chapter 4 furnishes information on protein structures and vibration, the different vibrations forms found in proteins are discussed here.

Chapter 5 is a brief but salient introduction to surface roughness and white light interferometry, the principle discussed here found use in SERS substrate characterisation. Chapter 6 was centered on microfluidics, the kernel of this chapter was fluids in motion at low Reynolds numbers, different types on immunoassays were described, and finally this chapter ends with a measured presentation on antibody immobilization. A description of materials and methods used in realising this thesis study is the focus of chapter 7.

Chapter 8 sums in precised details all experiments and results of this thesis work, surface characterisation of SERS Substrate with Rhodamine6G, antibody immobilization and the recorded Raman spectrum are all recorded here. In Chapter 9,

succinct discussion proceeding from the experimental results are presented, the analysis here aims to explain surface reaction and structure of thiols on gold, the mechanism of formatio of SAMS are also discussed, the crux of this chapter is the tentative assignment of wavenumber for the Genetex SARS-CoV-2 Antibody.

Chapters 10 and 11 finalizes this thesis report with conclusions and recommendation respectively. The Appendix section A is reference point for data sheets on important chemical used in the thesis work, while Appendix section B contains details on Raman and white light acquisition parameters.

2 IMMUNOREACTIONS

The human body is a biological workspace of cells, tissues and organs that interacts with its environment in various ways, In the process of interactions, the human body becomes exposed to complex foreign molecules that can promote or inhibits its proper functioning. In an event when such an interaction is with a virus, bacteria, or other chemical toxins, the body needs to protect itself. immunoreactions thus serve as the primary means by which the body protects itself from complex(Antigenic proteins). It is a reversible chemical reaction involving highly specific/affinity bound antibodies and antigens combining to form an antigen-antibody complex[noa, 2020b]. The immunocomplex is transported through the cellular system and destroyed or deactivated. Richard J. Goldberg at the University of WisconsinGoldberg [1952] was the first person to correctly explain the nature of the antigen-antibody reaction. Equation 2.1 shows this all important reaction scheme.

$$\text{Antigen}(\text{Agn}) + \text{Antibody}(\text{Abn}) \rightleftharpoons \text{Antibody} - \text{AntigenComplex}(\text{AbnAgn}) \tag{2.1}$$

In an immuno-response the dendritic cells of the mammalian immune system helps to break down the foreign molecule into smaller parts and present them to B cell lymphocytes(white blood cell antibodies) in the form of antigens. The macrophages cells and the complement system of antibodies also come in useful in an immuno-response. The antibodies and antigen can then combine in a process called agglutination(The crosslinking of antibodies with particulate antigens resulting in a visible clumping of the particle).[Proscience, 2020] For specificity of antibody to antigen, the antigenic determinant(epitope) must be identified and locked unto by the paratope of the antibody, see Figure 2.1.

2.1 OVERALL STRUCTURE OF ANTIBODY

Antibodies also known as an immunoglobulins Immunoglobin (IgG) are a family of glyco-proteins with a molecular weight of about 150 kDa [Janeway, 2001]. These large Y-shaped protein consists of four polypeptides; two heavy Heavy Chain (HC) and two light Light Chain (LC) polypeptide-chains linked by disulfide bond to form a 'Y' shaped molecule. The amino acid sequence present in the antibody light chain varies among different antibodies, this confers its specificity and selectivity to different antigen.[Quinn and Wang, 2008]. Figure 2.1 is a schematic of an antibody, it consist of a variable-region (V_H/V_L) domain of the antibody molecule, namely the hypervariable regions otherwise called complementarity-determining regions CDRs and (C_H/C_L) the constant domain of the antibody.

Figure 2.2 shows the 3D structure and schematic of structure of an antibody, the two variable arms makes up the F_{ab} which is subdivided to the two domains (V_H in the heavy chain and V_L in the light chain)[Edelman and Benacerraf, 1962], and the constant fragment crystallizable region of the antibody F_c which has two domains ($CH1$ and CL). The two F_{ab} region are hinged to the F_C, this allows for conformational flexibility about the hinge. Dimerization of the light and heavy chains functions to create the F_v fragment that carries antigen binding site(paratope). This process of dimerization(addition) also creates hypervariable loops three in each

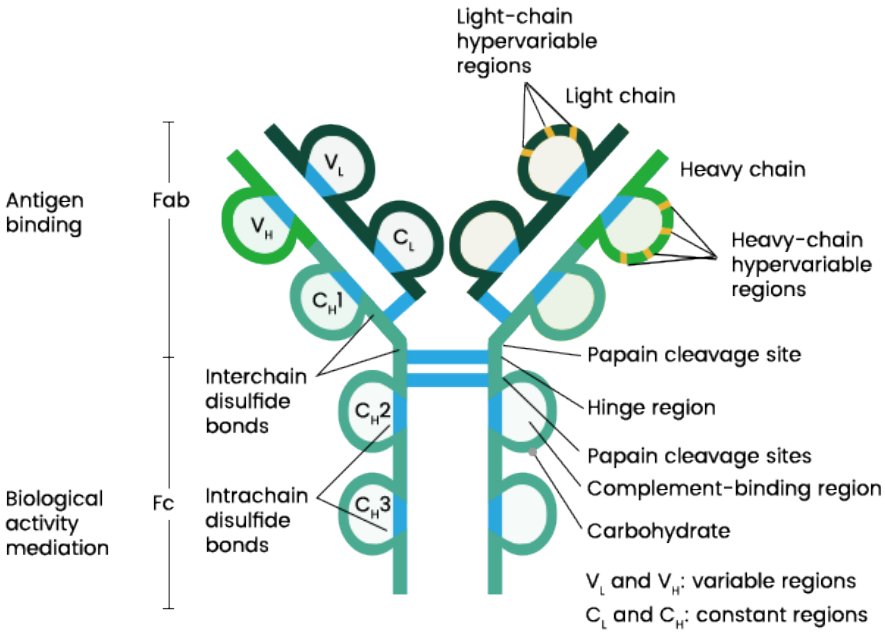

Figure 2.1: Schematic of Antibody showing variable and constant region.[Sinobiological, 2020]

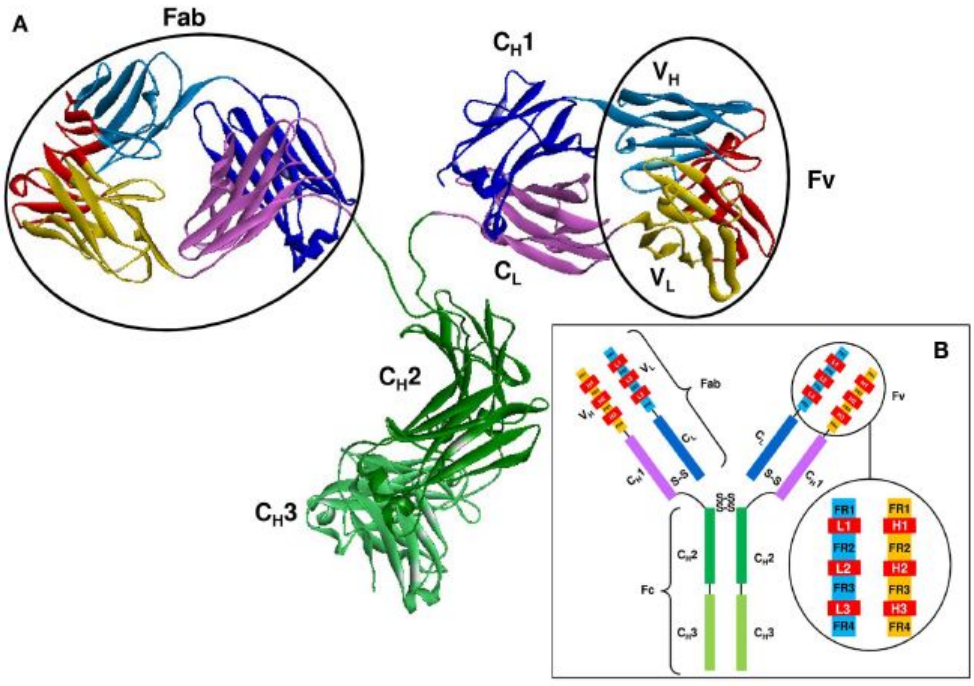

Figure 2.2: (A)Three dimensional structure of an Antibody, (B)Schematic of an Antibody[Sela-Culang et al., 2013]

summed up variable domain, (L1,L2,and L3) and (H1,H2,and H3) respectively. Each of these loop segments are structurally inter-spaced by a conserved framework region Framework Region (FR) of beta-sheets. In the constant region(heavy chain) of the antibody F_c, two additional domains CH2,and CH3 are present for mediating biological activation of the antibody.[Putnam et al., 1979]

Immunoglobin folds consist of 100's of amino acid residues of the light and heavy chains (see Figure 2.3) [Poljak et al., 1973, 1974]. The fold consist of two

tightly packed anti-parallel $\beta - sheets$ β-sheets. One of the two β-sheets of the C domains has three β-strands(↓C ↑F ↓G), and the other has four β-strands(↓A ↑B ↓E ↑D). An intra-domain disulphide bond serves to link the two β-sheets covalently together.[Chiu et al., 2019]

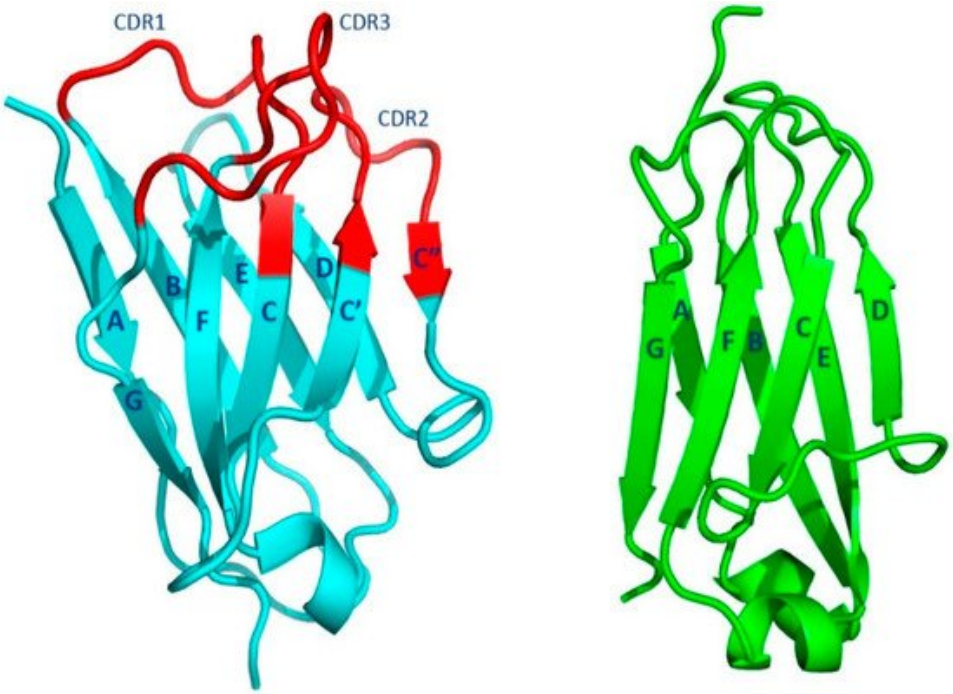

Figure 2.3: The immunoglobulin fold. The left(cyan and red) and right(green) ribbon image represents immunoglobulin folding pattern (V_H of Fab 388, PDBid 5i1a), with CDRs in red.[Teplyakov et al., 2016]

The disulfide bridge can be formed between two cysteine residues in any of the strands of the antibody molecule, these disulfide bridge is key in obtaining a SERS effect and in immobilizing the antibody(to be discussed under Microfluidics).[Chiu et al., 2019]

2.2 AFFINITY AND AVIDITY

The affinity of an antibody is determined by the strength of a single antigen-antibody bond. In such an affinity interaction there are position dependent forces at play, they can be attractive and repulsive, the strength of the affinity is a summation of all such position dependent forces.[Arevalo et al., 1993] Every antibody has least two antigen binding site, hence it is multivalent. Thus antibodies bonding multivalently to antigenic determinants is desirable due to increased bond strength, also the bond energies of such a multivalent binding is more than that of just one antibody-antigen bond. Avidity therefore represents the strength of the bond between multivalent antibody and multivalent antigen.[Kumagai and Tsumoto, 2002]

In an immunoresponse situation, antibody affinity progressively increases towards the target antigen(affinity maturation), multivalency of the antigen and antibody helps to speed up this affinity maturation effect, such that the immune system thwarts the antigen.

For binding to occur the antibody paratope segments will have to come into precise contact with complimentary antigenic determinants(epitope). The specificity of each antibody is governed by the amino acid sequences of its complimentary determining domains(CDRs). CDRs vary across antibodies and at such the shapes of the surfaces created by these CDRs varies too. The structures affined to the dimerized

segments of the antibody are located on the surface of proteins, such surfaces are the product of protein folding of antibody polypetide chains which possess conformational or discontinuous segments.[Sela-Culang et al., 2013]

From quantum mechanical considerations, all chemical bonds are based on electrostatic forces. Antibody-antigen association depends on forces inherent in these chemical bonds, namely Van-der-Waals forces(weak and able to attract molecules of all kind), Hydrogen bonds/ion-dipole bonds(requires oppositely charged atoms) [Reverberi and Reverberi, 2007]. Weak and noncovalent forces like Van der Waals forces, hydrogen bonds, electrostatic interactions and hydrophobic interactions hold the antigen-antibody complex together, ability to tune these interaction opens a window of opportunity to improving specificity, multispecificity and the development of new vaccines.

The antigen-antibody reaction finds ready applications in laboratory diagnostics, including Enzyme-linked immunospot Enzyme-linked immune absorbent spot (ELISPOT), Immunofluorescence, immunoelectrophoresis, immunohaematology and Immunoassays.[Pro-Sci, 2020]

Immunoassays makes use of the immunoreaction done on microfluidic devices to detect either Abs or Ags according to the needs of the experiments. In the context of reaction scheme, immunoassays can be classified as either competitive or noncompetitive(to be discussed further under Microfluidics).[Bojorge Ramírez et al., 2009]

2.3 ANTIGEN–ANTIBODY INTERACTIONS

Antibody affinity interaction denotes it capacity to attach to a given antigen, this interaction with antigen occurs at numerous sites, the higher the interaction the stronger the affinity. In literature Avidity is viewed as a more informative measure of the total stability or strength of the antibody-antigen complex. As discussed in Section 2.2 avidity is influenced by the conformation of interacting parts, antibody epitope affinity, and the valence of both the antibody and antigen.[Steward, 1984] Avidity and affinity are deduced from the dissociation constant of the interactions they describe. A low dissociation constant, signifies higher avidity or affinity, and stronger interaction. From Equation 2.1 above, [Abn] and [Agn] are the antibody and antigen respective concentration in free [Abn] state, and [AbnAgn] is the immunocomplex concentration.[Reverberi and Reverberi, 2007]

An equilibrium constant K measures the effectiveness of a single epitope-paratope binding in a forward reaction,

$$K_{assoc} = \frac{\mathbf{[AbnAgn]}}{\mathbf{[Abn][Agn]}} \tag{2.2}$$

Reciprocally the dissociation constant in a backward reaction will be:

$$K_{dessoc} = \frac{\mathbf{[Abn][Agn]}}{\mathbf{[AbnAgn]}} \tag{2.3}$$

A higher value of the equilibrium constant means a stronger antibody-antigen bond, in order for a reaction to proceed spontaneously, the free energy change shown in Equation 2.4 must be negative.

$$\Delta G = \Delta H - T \cdot \Delta S \tag{2.4}$$

Where H is enthalpy(energy in the chemical bonds of reactants and products), S is the entropy, the symbol Δ represents the change in variable occuring during the

immunoreaction. In immunoreactions many complex multiple epitope-paratope bindings occur, leading to multiple equilibriums, summed up as:

$$\mathbf{K} = \frac{r}{c(n-r)} \tag{2.5}$$

At equilibrium, r represents the ratio of the concentration of bound antibody to total antibody concentration, c is the concentration of free antibody, and n is the maximum number of binding sites per antibody molecule.

For stable binding and a long-lasting effect at physiological temperatures, multiple weak bonds must be present contemporaneously and this requires steric complementarity between the antibody and antigen molecules[Watson, 2014].

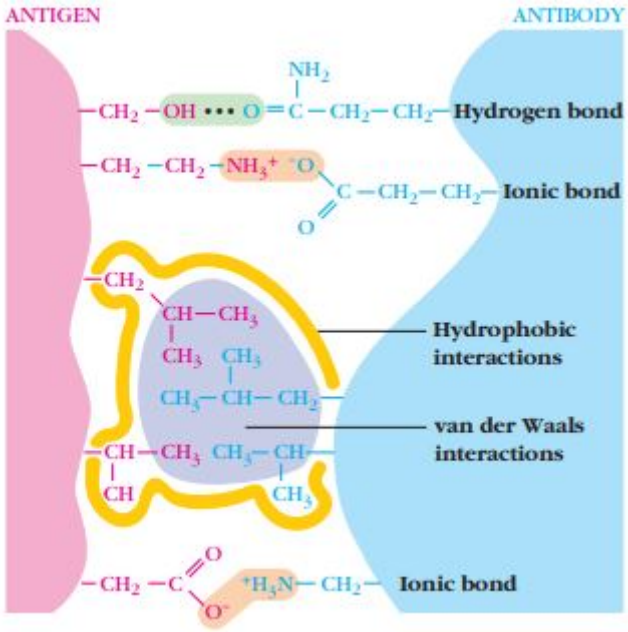

Figure 2.4: Schematic of antibody and antigen interacting via Hydrogen bond, Ionic bond, weak Van der Waals forces and hydrophobic interactions[Goldsby and Goldsby, 2003]

As epitopes and paratope approach each other at a distance of a few nanometers, they are attracted by long range ionic and hydrophobic hydration nullifying force. At a shorter separation distance, Van-der-Waals forces(short-range and decays with the seventh power of the inter-atomic spacing and their total contact area[Zheng and Narayanaswamy, 2011]) predominate, with minor contribution from ionic groups. Steric repulsion's(originates from the arrangement of atoms in a molecule) becomes noticeable at these close distances whilst affecting the overall binding strength and the specificity of the lock and key mechanism. Figure 2.4 shows a schematic representation of the interacting forces between the antibody and antigen.

2.3.1 Van-der Waals Forces

The Van der Waals force is a weak and transient electrical force between atoms and molecules. This effect originates from the fluctuating electron cloud of atoms, creating a temporary electric dipole. complementary dipole can be induced in an atom by a transient dipole in an atom nearby. Atrractive and repulsive van-der-waals can manifest from such complimentary interactions dependence on the distance between the atoms, when atoms are too close together, repulsion results; at an optimal separation distance attraction is observed.[Branden and Tooze, 1999] In general antibody-antigen reaction takes place in aqueous medium, such mediums have very

low interfacial tensions γ_{AbAg} of order ($\gamma_{AbAg} = 21.8mJ/m^2$). Hence, the free energy of interaction ΔG_{AbAg} is always negative and antibody and antigen interaction is attractive.[van Oss, 2000]

The Van-der waalsVan-der Waals (vdW) interactions between antibody and antigen are somewhat additive. When the antibody and antigen are imagined to be flat and facing each other the free energy of interaction $\Delta G_{AbAg}$of the antibody-antigen can be positive (repulsive) or negative (attractive) depending on the value of the Hamaker coefficient **A** (captures the strength of vdW interaction force between Antibody and Antigen[Absolom and van Oss, 1986]) of the liquid medium.

Protein-protein recognition is aided by Van-der waals forces due to their effect in packing of protein polypetide chains into appropriate complementary shapes. In the famous "lock and key" fit of the two molecules, Van der Waals attractions are observed. Van-der-Waals interactions usually accounts for about 10% of the total long range interaction forces, on expulsion of interstitial water from the binding environment, vdW interactions may account for the entire short range of interfacial energy. Pressman and Grossberg[Grossberg and Pressman, 1968] stated that the minimum distance between the epitope and the paratope, can be as small as about 2Å, and in ideal cases can approach 1.6Å

2.3.2 Electrostatic Forces

Multiple ionized sites on epitope and an oppositely charged complimentary sites on the paratope interact to generate Electrostatic Electrostatic force (EL) between Agn and Abn. Typical ionized groups responsible for the EL interaction are the COO^- and the NH_2^+ or NH_3^+ groups present on the amino acids of the Agn and Abn molecules.[van Oss, 2000] Polarized water molecules usually form shells around the charged interacting surface, these shells serves to protect and stabilize the interaction.

As in the case of Van der Waals interaction, electrostatic effects decreases with distance according to :

$$\Delta G^{EL} = \Delta G \exp(-\kappa l) \tag{2.6}$$

where κ represents the electrostatic decay length often called the debye length, l is the distance between interacting molecules[Overbeek, 2008]

Electrostatic interaction can also occur through the calcium bridging effect, this is when a negatively charged paratope binds to a negatively charged epitope by means of a Ca^2+ linkage and moieties. The addition of pluravilent Calcium cations Ca^2+ to the Antibody-Antigen aqueous environment reduces the ζ_o of the negatively charged entities, the plurivalent calcium acting as electron-acceptors strongly attenuates the electron-donicity of the hydrophilic entities making them hydrophobic.([Wu et al., 1994]). Consequently improving affinity and specificity of the immunoreaction.

2.3.3 Hydrogen Bonds

Hydrogen bond is the attractive force between two atoms bearing a partial negative charge and sharing a partially positively charged hydrogen. Hydrogen Bonding between adjacent sections of an amino acid peptide causes it to fold into a specific shape, this fold confers upon the molecule physiological or biochemical function.[Wikipedia, 2020a]

2.4 THE ROLE OF HYDRATION IN ANTIBODY ANTIGEN INTERACTIONS

The antibody and antigen surface becomes hydrated when in contact with water, In this interaction, several hydration states are transversed, the variation in hydration states confers conformational flexibility on the backbone proteins interacting. The aqueous environment functions as a lubricant, facilitating the needed alterations in hydrogen bond patterns the aids conformational fluctuations[Barron et al., 1997].

Three-dimensional structure and packing of antibody and antigen is governed by hydration forces, packing forms and structures are invaluable in mediating their bioactivity. In water, the hydrophobic side chains of antibodies and antigens interact in such a way to be shielded from the aqueous environment, forming a tightly packed convolution of the nonpolar side chain of the backbone protein making the antibody or antigen.[Levy and Onuchic, 2006]

A typical hydrated interfaces of formed complexes consist of about 10 water molecules per $1000\mathring{A}^2$ of interface area[Rodier et al., 2005]. The extent of hydration on the interface of the interacting antibody and antigen correlates to various spatial distribution patterns that depends on the geometry of the interface[Levitt and Park, 1993].

Functioning as part of the recognition code, water mediates interactions that are less favourable in its absence; hydration water ensures improvement of binding interface and in selecting appropriate potential binding sites. Molecular dynamic simulation shows that trapped water enhances affinity/avidity by a gain in free energy occasioned on the higher entropy of trapped water molecules which have more motion freedom than bulk water[Petrone and Garcia, 2004]

In a situation where a less than ideal fit exist, water is not readily expelled from the variable positions of the paratope, such interstitial water will inhibit binding between epitope and paratope at such they combing members will interact at greater than optimum distance. When expelled such loss of water of hydration into the bulk of the aqueous medium increases the entropy of the Agn-Ab reactions. [Absolom and van Oss, 1986] While the knowledge of the "goodness of fit" is useful, experimental evidence points to the importance of the best steric fit between paratope and epitope as the prime condition for realizing the highest Agn-Ab-binding energy[Weatherall, 2011]. Mariuzza et al [Mariuzza et al., 1987] discussed at great lengths the optimal fit hypothesis and the surface accessibility mechanism, a measure of corporatism between both concepts helps induced a better fit of the epitope-paratope complex, however an energy price will have to be payed for enhanced motility of interacting peptides.

2.5 CONFORMATIONAL CHANGES OF ANTIBODY AND ANTIGEN

An ongoing debate in literature concerns the true nature of conformational changes in antibody, antigen or during antigen-antibody interaction. This debate extends to the possibility of the lock and key or the induced fit mechanism been the governor of antibody-antigen reaction. In the lock and key paradigm there are no conformational changes in the interacting proteins, the reacting proteins behave as if rigid[Fischer, 1894]. Induced fit implies conformational alterations for the interaction between antibody and antigen to become, such changes are facilitated by the interplay of several forces as already described in Section 2.3.1 and Section 2.3.3. These forces influence the readjustment of side groups through the movement of the hypervariable loop in the antibody, and the backbone atoms of interacting pro-

teins.[Getzoff et al., 1987] Significant conformational changes occur in the antigen during the binding process[Davies, 1988].

Colman et al [Colman, 1989] suggested that binding of an antigen to an antibody produces a movement of the V_H relative to V_L in such a way that complementarity between the interacting proteins is enhanced, the above mentioned mechanisms for conformational changes are readily observed in experiments.

2.6 ANTIBODIES FOR SARS-COV-2

Antibodies that can recognize and bind to the SARS-CoV-2 spike protein can block virus from infecting human cells, and at such provide an "immunity passport" or "risk-free certificate" that would guarantee no re-infection when individuals begin to travel and return to normal work activity. [WHO, 2020] Indeed, to speed up the development of such a life saving antibodies, several research into vaccines that can trigger the human body to produce the needed antibodies is on going with some success recorded by Pfizer, Astrazeneca and Gamaleya Research institute.[NIH, 2020]

The world health organisation highly recommends laboratory tests that can detect and validate antibodies to SARS-CoV-2 in people, to this effect rapid immunodiagnostic tests can and have been employed to determine their accuracy and reliability.

Dr. Davide Robbiani and Michel Nussenzweig at the Rockefeller University have been able to isolate naturally produced antibodies from the blood plasma of recovered patients. Such antibodies have been subject to much study, it was found that the isolated antibodies could bind to the receptor binding domain Receptor Binding Region (RBD) of SARS-COV-2 virus antigen and at such stop the infection.[Robbiani.et.al, 2020] They also showed that the percentage of potent antibodies recovered from blood plasma of some 149 patient is about 1%, each of the recovered antibodies showing some similarity, binding analysis suggest that COVID-19 antibodies may fall into three groups, each binding to a different part of the RBD.

2.7 FACTORS AFFECTING ANTIGEN-ANTIBODY REACTION

A varied number of factors affect the efficacy of antibody-antigen reaction namely: temperature, ionic strength, pH of solution, time, strong electron-donor polymers and strong dehydrating agents. These factors are further discussed below.

2.7.1 Temperature

Antibodies react optimally with complementary antigens at +37°C. At this temperature, reaction rates are increased[Banes, 2020]. The chemical nature, and the types of bond present in paratope and epitope govern the appropriate thermal optimum for antigen-antibody reaction. [Absolom and van Oss, 1986] Worthy of mention is the fact that equilibrium constant is minimally affected by thermal fluctuations.

2.7.2 Ionic strength

Lewis and Randall in 1921 introduced the idea of ionic strength. Ionic strength measures the concentration of different ions in a given solution. Ionic compounds like $NaCl$, when dissolved in water, dissociate into ions Na^+ and Cl^-. An aqueous medium provides an environment for the partial neutralization of the ionized functional groups of both the antibody and antigen. Lowering the ionic strength of the medium while maintaining osmotic pressure gradient(tonicity) increases the rate of

association of antigens with antibodies, little or no effect is observed on the rate of dissociation.[Banes, 2020]

2.7.3 pH of solution

The pH for optimum antigen-antibody reaction is between 6.5 to 7, at this pH the equilibrium constant for the forward reaction will increase faster, for example anti-D antibodies shows a characteristic maximum of reactivity at this optimal pH, at values higher or lesser the equilibrium constant of the immunoreaction becomes some 100 fold lower. This reduction in reactivity is generated by conformational alterations of the antibody molecules that inhibits complementarity with antigen.[Banes, 2020]

2.7.4 Time

For proper complexing, the antigen and antibody should be incubated for an optimum time for a good antigen–antibody reaction to develop. With the passing of time the Agn-Abn bond becomes stronger as a consequence of secondary interactions. However, the optimum time is what is required not a very long incubation time, so the best balance in time is determine as this also prevents antigen–antibody complexes from dissociating due to extended incubation time.

2.7.5 Electron-Donor Polymers

An electron-donor polymers like polyethylene glycol as a repelling effect on most proteins in aqueous solution, when added in small quantities to Ab-Ag solutions, these polymers can agglomerate the proteins into smaller volumes and dehydrate them in an incipient phase separation. The above stated process facilitates the formation of Ag-Ab complexes. It is worthy of mention that small concentrations of about 3-10% (v/v) be used so as to prevent precipitation of free immunoglobins.[van Oss, 2000]

2.7.6 Strong Dehydrating Agents

The addition of Ammonium sulfate $(NH_4)_2SO_4$ in molar concentrations to an Ag-Ab system favors hydrophobic attraction and decreases epitope and paratope distance, this results from the insolubilization of Ag-Ab complexes by dehydration, However, in an Ag-Ab system that is strongly electrostatic, $(NH_4)_2SO_4$ will function to dissociate such an Ag-Ab complex.[van Oss, 2000]

3 RAMAN SPECTROSCOPY

Raman scattering was theoretical predicted by Smeka in 1923[Vítek et al., 2017] and experimentally confirmed in 1928 by Chandrasekhara Venkata Raman and K.S Krishnan in India and Landsberg and Mandelstam in Russia. Both groups discovered that when electromagnetic energy in the form of monochromatic light(either near ultra-violet, infra-red, visible or x-rays photons) passes through a material in the solid, liquid or gaseous phase, it interacts with the atoms, molecules or particles of the system and gets scattered both elastically and in-elastically. For the in-elastically scattered photons the energy after the scattering event is less than the incident energy, hence their wavelength increases and as such contains information about the material interacting with the incident light. Raman scattering occurs in the order of femtoseconds, florescence is much slower effect, hence timing is can help to discriminate both effects.[Shipp et al., 2017]

This phenomenon of inelastic scattering of incident photons is referred to as the Raman effect (Raman scattering).[Smekal, 1923] In 1953, the first commercial Raman spectrometer became available, it employed a monochromator and a mercury lamp at a wavelength of 435.8nm operating as the light source. It's use for identifying compounds was limited by the light source and coloured samples absorbed mercury radiation.[Mitsutake et al., 2019] With the invention of lasers in 1960, Raman spectrometers could then overcome the above shortcoming and be applied in a faster and reproducible manner.[Porto and Wood, 1962]

Use is made of this effect in "Raman spectroscopy" as it provides chemical and structural information about target molecules, the chemical and structural information are captured in the form of intensity peaks in a spectrum. These peaks are characteristic of the probed molecule hence a "fingerprint". Figure 3.1 shows a detailed pictorial schematic of a typical raman spectrum and how to understand the information it presents. Raman spectroscopy is used in molecular analysis because of the characteristics listed below[Larkin, 2018]:

1. Sensitivity to traces changes in material concentration.
2. No need for time-consuming extraction or drying, which may also alter the chemistry of your samples.
3. Non-destructive and non-contacting.
4. It uses light(wavelengths can be altered for possibly obtaining Plasmon resonance with SERS substrate).
5. Capacity to differentiate Chemical composition and structure of materials even in mixtures.
6. Typically no sample preparation. Works on almost all materials except pure metals.
7. Analysis through transparent containers and windows.
8. You can analyse samples in water.

With all its atrractiveness for sample analysis the Raman spectroscopy is limited by spatial resolution of diffraction optics, subsampling due to a too small sampling area, spherical aberration/refraction and poor signal focus.[Smith et al., 2015]

Figure 3.1 is a schematic of a Raman spectrum with description of the information obtained from any Raman analysis.(The Raman spectrum of proteins to be discussed later in the chapter will illustrate this.)

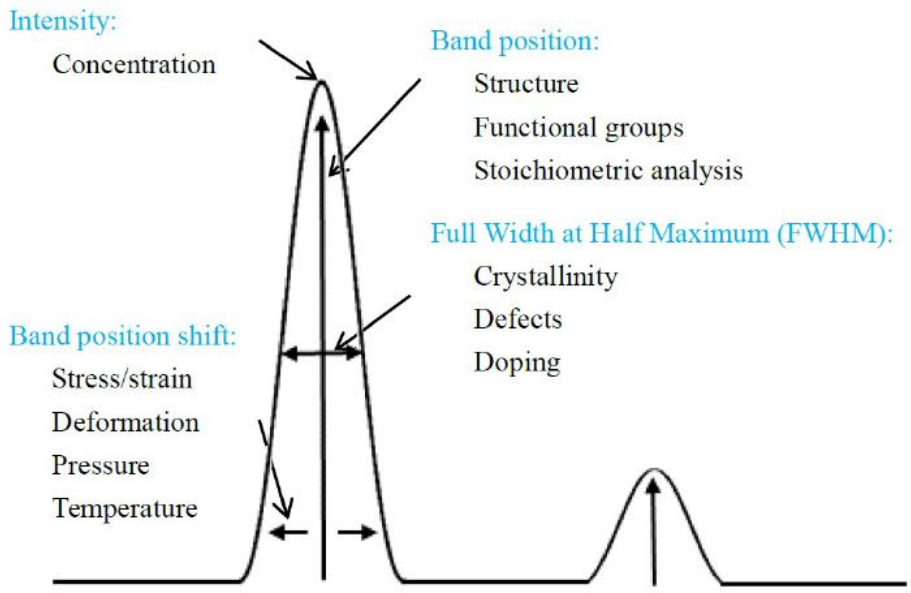

Figure 3.1: Schematic of a Raman spectrum with description of the information obtained from any Raman analysis.[Xu et al., 2018]

Raman spectroscopy differs from infrared spectroscopy in its dependence on electric-dipole - electric- dipole polarizability derivative with latter depending on electric dipole moment derivative.[Colthup, 1990]

The above dependencies influences effective energy transfer to the probed molecule and also predisposes infrared spectroscopy for analyzing polar molecules and raman spectroscopy for analyzing non-polar molecules, the two techniques should be viewed as complimentary and not duplicates.[Raman and Krishnan, 1928]

3.1 RAMAN SCATTERING

The quantum mechanics posits that spatially confined particles/atoms can only take up discrete energy values and transit discrete energy levels/states. For vibrational or rotational energy levels in molecules, this view is valid. Such a molecule is said to be quantized. Two types of scattering process exist, the elastic(Rayleigh) and inelastic scattering process. In the elastic scattering process, energy of the target molecule is unaffected by interaction with the incident photon; hence the energy of the incident photon is conserved(wavelength and frequency remains constant) [Wikipedia, 2020b]. In all scattering event the elastic scattering process is dominant over the inelastic scattering process. see Figure 3.2(a) and Figure 3.3.

The Raman Scattering process entails the interaction of a photon with a molecule, the interacting molecule becomes energized to a higher energy level(virtual state). The molecule may lose energy and relax to a lower vibrational energy state than its initial state, this action produces a photon of a different energy than that of the incident photon.[bwtek, 2021] The polarizability of electron in a molecule, atom or crystal is the prime determinant of the magnitude of the raman effect, when a target molecule is energized by incident photons, polarization of the molecular electron cloud of the target molecule is induced by the oscillating electromagnetic field of the incident photon.[Hammes and Hammes, 2005] The interaction can be viewed

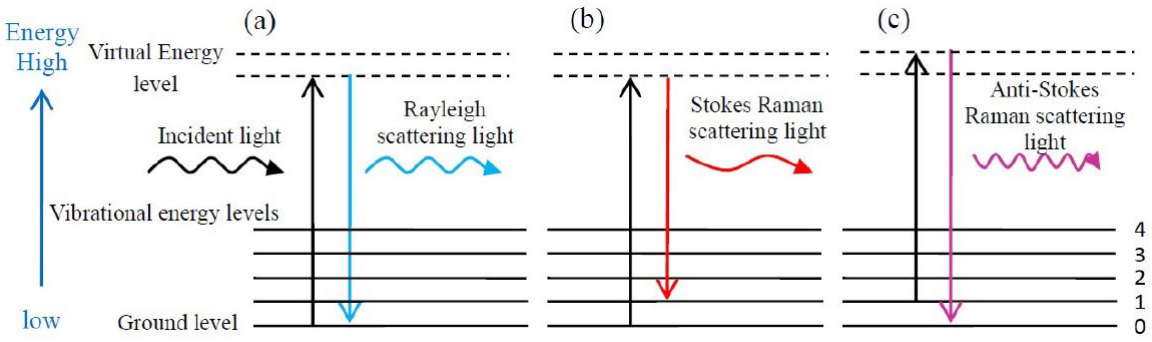

Figure 3.2: Schematic of energy level transitions for:(a) Rayleigh scattering, (b) Stokes Raman scattering and (c) Anti-Stokes Raman scattering.[Xu et al., 2018]

as a short-lived complex of photon and target molecule which is unstable with the photon emitted almost immediately in the form of scattered light.

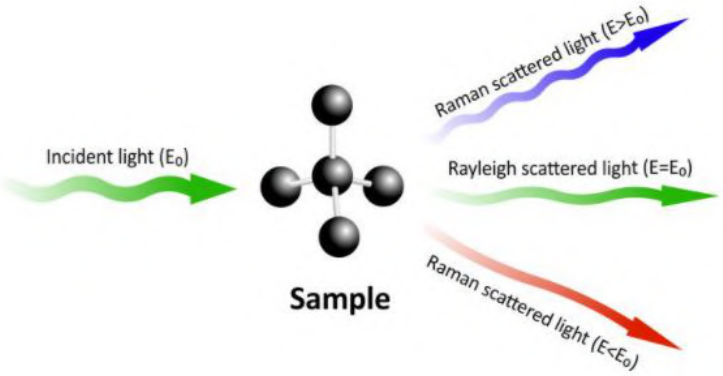

Figure 3.3: Three Scattering processes of light interacting with matter.[integratedoptics, 2020]

Smith and G. Dent recorded in a particular observation that approximately 1 in 10 million photons were in-elastically scattered.[Smith and Dent, 2005]

Inelastic scattered photons manifest in two forms: Stokes and Anti-stokes Raman scatter. These manifestations are according to the energy change between the target molecule and incident photons. Stokes Raman scattering (after G. G. Stokes) occurs when the target molecule gains energy from the incident photons during the scatter, the incident photons loses energy with a consequent increase in wavelength.[Long, 2002] conversely, Anti-Stokes Raman scattering occurs if the target molecule transfers energy to the incident photon, the corresponding energy gained by the incident photon serves to decrease its wavelength, see Figure 3.2(b),(c) and Figure 3.3. In any inelastic Raman scattering event the stokes Based on the Boltzmann distribution, Raman scatter has statistically higher chance of occurrence, hence Raman spectrum majorly represents stokes Raman scatter.[Hammes and Hammes, 2005]

The target molecule under the influence of the incident light absorbs incident photon energy and gets excited to higher electronic state, it then emits a photon and returns to the ground state: A process called fluorescence or phosphorescence.This fluorescence signal should not be confused with the rotational and vibrational state change that results in the Raman effect.

The excitation wavelength influences the scattering wavelength making it impractical to contrast or compare spectrum obtained with incident light of varying wavelength. To remedy this, Raman scatter positions are converted to a Raman shift($\Delta\overline{\nu}$) away from the excitation wavelength.

The Raman shift represents the energy difference between the incident (laser) radiation and the scattered radiation. The energy difference is only related to the

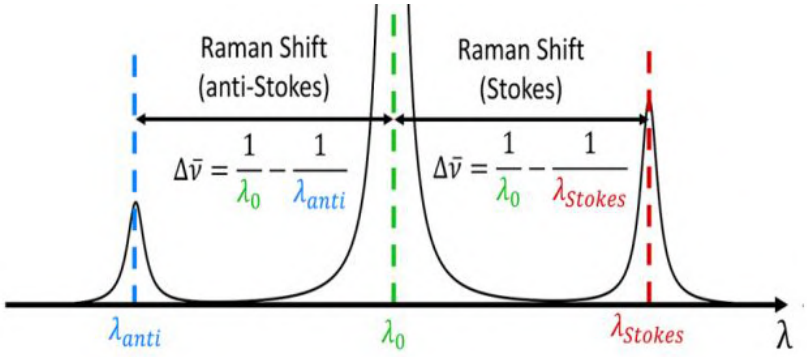

Figure 3.4: Schematic showing offset of Stokes and Anti-Stokes Raman Scatter from the Rayleigh scatter line [Xu et al., 2018]

energetic properties of the target molecules molecular vibrations and hence independent of the laser wavelength. The formula for calculating this Raman shift is shown in Equation 3.1:

$$\Delta\bar{\nu} = \left(\frac{1}{\lambda_o(nm)} - \frac{1}{\lambda_1(nm)}\right) * \frac{10^7(nm)}{(cm)} \tag{3.1}$$

λ_o is the wavelength of excitation light, and λ_1 is the wavelength of the inelastic scatter(alter excitation light), the unit for expressing wavenumber in Raman spectrum is inverse centimeters cm^{-1}. The Raman shifts about the excitation wavelength means that the stokes and anti-stokes scatter peaks forms a symmetric pattern about the Rayleigh line $\Delta\nu = 0$, see Figure 3.4. [Long, 2002]

The rate of transition of a photon from the higher excited state to the lower vibrational state is proportional to E_o(the incident electric field), and scales linearly with incident light intensity.

The Raman scattering cross-section measures the scattering activity of an analyte, a large Raman scattering cross-section implies a large likelihood for an effective measurement. The Raman cross-section $\sigma^{'}$ can be determined from the Equation 3.2

$$I_s = \sigma^{'} \cdot J \cdot N \tag{3.2}$$

where I_s represents the scattered intensity of light in Watts per steradiant, J represents the excitation irradiance in Watts per meter squared, and N is the number of molecules irradiated. Long calculated the typical values for a raman cross-section to be on the order of $5 \times 10^{-35} m^2/sr$.

3.1.1 Wavelength dependence of Laser Penetration Depth

Lasers with different wavelength will have different penetration depth into the probe sample, in a multilayered samples, different wavelength of incident lasers can be used to obtain multiple information from target samples and on different spots on the sample.

Information closer to the surface are readily probed by shorter wavelengths while longer wavelength laser penetrate deeper, caution is needed to ensure that the chosen laser wavelength is not to large or too small as this can lead to loss of information near the surface or deep into the surface respectively. semiconductor[Chafai et al., 2001]. In any Raman spectroscopic analysis, the total scattered light intensity I_s integrated from surface to depth(d) is given as

$$I_s = \int_0^d \exp(-2\alpha_{phtsb}x)\, dx = \frac{I_o D}{2\alpha_{phtsb}}(1 - e^{-2\alpha_{phtsb}d}) \tag{3.3}$$

and the light intensity I_d from depth (d) to infinity is quantified by

$$I_d = \int_d^{\infty} \exp(-2\alpha_{phtsb} x)\, dx = \frac{I_o D}{2\alpha_{phtsb}} (e^{-2\alpha_{phtsb} d}) \tag{3.4}$$

where I_o, $\sigma^{'}$, α_{phtsb} are the intensity of incident light, the Raman scattering cross section and the photoabsorption coefficient, respectively [Loudon, 1965].

3.2 INSTRUMENTATION FOR RAMAN SPECTROSCOPY

The instrumentation needed to implement raman spectroscopy is easy to come by, these instruments include a sample holder, a light source(laser), objective lens, filters(dichroic mirrors, notch filter, bandpass, laser line filter, Edge filter e.t.c) monochromator, detector and a computer system. Various schematic exist for combining these instruments together to achieve raman spectroscopy. Figure 3.5 shows two of such possible schematics. The experimental setup is arranged to ensure that light traveling from the laser is focused on a given sample and the scattered light returning from the illuminated sample is appropriately directed by the dichroic mirrors to a spectrometer for interpretation. In order to focus on a specific point and perform spatial analysis, it is important to use the right microscopic objective and focusing lens.

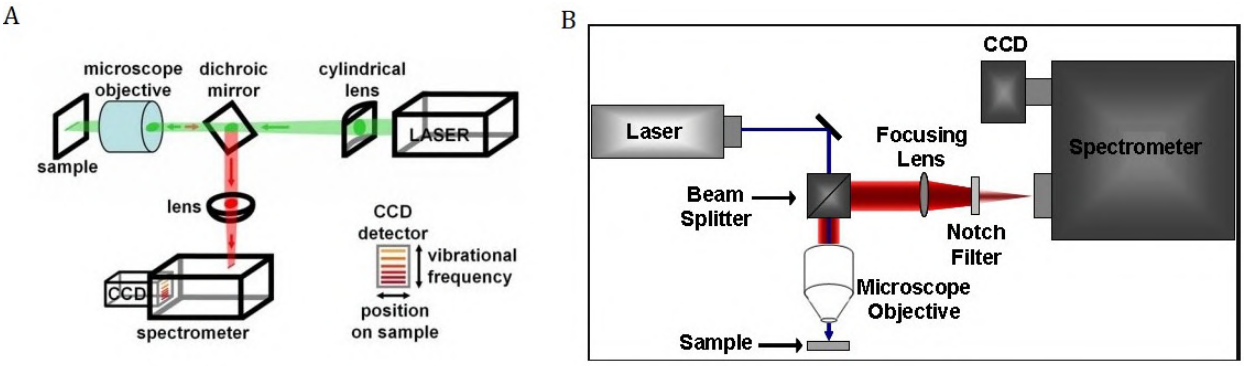

Figure 3.5: Instrumentation schematics for Raman spectroscopy (A)[Downes and Elfick, 2010] and (B)[Sciencefacts, 2015]

SAMPLE HOLDER: Sample holder for the raman spectroscope usually have an XYZ positioning and a rotary stage, the motion of these stages are actuated by piezomotors or linear actuators. The sample holder helps to align the probed sample to the focused laser light. Some sample holders come fitted with a spring-loaded cap that blocks unnecessary exposure to laser irradiation.[inPhotonics, 2020]

LASER: Lasers of various types can serve as the light source for the raman spectroscopy. The bandwidth of the light source directly affects the resolution of the raman spectrum.[Kukura et al., 2007] In operation the laser optical output and wavelength defines the effectiveness of the scattering process. It is important to tune the incident laser wavelength so that the output raman scatter is above that of the baseline scatter for the given material.[ibsen, 2020]

To get higher counts of raman scatter, shorter wavelengths of incident light should be used as this leads to increase $1/\lambda^4$ with and attendant increase in scattering cross-section.[McCreery, 2000] This positive however leads to problem with fluorescence and degradation of samples. At longer wavelengths of about 1100nm, special detectors like Indium Gallium Asernide (InGaAs) are needed.[ibsen, 2020] Continuous wave and pulse lasers can be used for raman spectroscopy, the latter affords more

bandwidth than the former and also finds utility in time-resolved, transient and resonance Raman spectroscopy.

The laser wavelength of 785nm is the most employed in Raman analysis as it is a good balance between fluorescence and scattering for many materials, while covering upto $3650cm^{-}1$. Other laser sources and their corresponding wavelength include Kryptonion laser (530.9 and 647.1 nm), Neodymium–Yttrium Ortho-Vanadate(Nd:YVO_4) (1064 nm), Near Infrared (NIR) diode lasers (785 and 830nm), frequency doubled Nd:YAG and Nd:YVO_4 diode lasers (532 nm), Argon ion laser (488 and 514.5nm), and Helium–Neon (He–Ne)(632.8nm). [Chalmers et al., 2012] The choice of a laser to use depends on cost and the irradiation limit of a given sample.

OBJECTIVE LENS: In Raman spectroscopy the objective lens is the closest optical device to the sample been probed, it focuses laser light on the sample and gathers scattered light from the sample, it can consist of a single optical element or several elements. For proper Raman analysis, all measurement conditions needs to be taken into consideration. An efficient objective lens should have a transmission of 80-90% at a wavelength of 500nm, this value can become 40% or less at a wavelength of 900nm.[WITec, 2020] Other important metric for a good objective lens for raman spectroscopy are spatial resolution, collection efficiency, opportunity to operate under required condition, working distance between sample and objective, capacity to correct imaging errors and depth of focus.

Numerical apeture Numerical Aperture (NA) is a function of the focal length of the objective lens, its also defines the power density of the excitation spot, the higher its value the better the collection efficiency and spatial resolution.[noa, 2020c] HORIBA scientific, a Japanese manufacturer of precision instruments for measurement and analysis provides a range of objective lenses with magnification ranging from 5x to 100x that spans various application in raman spectroscopy. Namely:

1. Ultravoilet A Ultra-violet A (UVA) - (for Deep UV excitations)
2. Ultravoilet B Ultra-violet B (UVB) - (Optimized for 325nm excitation)
3. Near Infrared Near Infrared (NIR) - (for 785 and 830nm lasers)
4. (Ultra) Long working distance Ultra-long Working distance (LWD/ULWD) - (Used in cells)
5. Visible Imaging System Visible Range (VIS) - (Employed in non-contact sampling with red, blue and green, lasers)
6. Reflective 74x Ultra-Violet (UV)-vis-NIR objective
7. Immersion objectives - (Used in biological sampling)
8. Refractive Index Refrative Index (RI) Corrected - (Used for imaging through the depths of cells and other biological samples)[HORIBA, 2020]

FILTERS: Filters are an indispensable component of the raman spectrometer, it has been established that raman scatter signal generated during any illumination event are very low, hence there is need to effectively capture this low raman signal. Several filters like the dichroic mirrors, notch and edge pass helps to increase the signal to noise ratio of the inelastic scattered photons by attenuating/blocking the laser signal from reaching the detector.[Iridian, 2020] A high transmittance (>95%) of the Raman signal, and high reflectance (>95%) of the laser line is desirable in filters. These filters are usually provided according to the wavelength of light that they block out.

DETECTORS: The light of a particular wavelength that has been transmitted by the filter is dispersed by a spectrograph for detection Fourier transform Fourier Transform (FT) method. Advances in electronics lead to the implementation of a raman spectrometer employing several arrays Charge Couple Device (CCD) for signal detection, these CCD can be fine tuned for different wavelength range of interesting[Efremov et al., 2007] The CCD is an array light sensitive sites that converts incoming into electrons, which is quickly moved to a storage or a readout devices. CCD are particularly slow in operation and less effective in the NIR range.

3.3 SURFACE ENHANCED RAMAN SPECTROSCOPY(SERS)

SERS is novel method of analyte detection that involves adsorbing certain molecules on the surface of a roughened/corrugated noble metal like(copper, silver and gold), exposing the prepared surface to a raman spectrometer results in an increase in raman intensity of about $10^8 - 10^{12}$ as compare to adsorbing the molecule on a flat unprepared surface Fleischmann et al [Fleischmann et al., 1974] initially presumed that the enhancement effect of the raman intensity was derived from a large increase in surface area afforded by the uneven metal surface. This was proved incorrect by Jeanmaire et.al[Jeanmaire and Van Duyne, 1977] and independently by Creighton et.al in 1977[Albrecht and Creighton, 1977], for an electrode surface roughened by no more than a factor of 10, they found the corresponding SERS signal to be disproportionately high at that surface roughness, such that another mechanism at to be at play to account for such raman intensity measured.

Moskovits et.al[Moskovits, 1985] submitted that the increased intensities originated from optical excitation of the aggregate motions of surface electrons on metallic nano-sized domains. Subsequent studies of the enhancement mechanism later affirmed that there is an electromagnetic and a chemical facet to the SERS enhancement mechanism. Due to the aforementioned amplification factor SERS is the preferred method for trace analyte detection in POC situations. Multiplexing(simultaneous detection of multiple analyte becomes possible, precised and even faster).

CHEMICAL ENHANCEMENT: The basic kernel of the chemical enhancement process involves either a transfer, exchange or sharing of charges between the analyte molecule and the substrate at active sites, in the process, coordination bonds may be formed with the metal surface atoms [Campion et al., 1995]. This interaction results in a change in the polarizability of the analyte molecule. The chemical enhancement is the dominant mechanism for molecules on small nano-clusters with appreciable band gaps.[Tsuneda et al., 2019]

In comparison to the electromagnetic enhancement, the chemical enhancement is particularly modest with a typical contribution of about 100 times the unenhanced raman signal.[Park and Kim, 2010] The adsorption of the chemical compound at a very small distance from a substrate (a few Angstroms) is needed for significant chemical enhancement.[Deepak, 2018]

Several models to explain the chemical enhancement contributions have been proposed: The ***"static charge transfer"*** model posits that there is polarizability change to the metal-molecule complex which consequently leads to a larger raman cross-section of the complex.[Jensen et al., 2008] A second model, the ***"transient charge transfer"*** model argues that the temporary electron or hole transfer between metal and molecule leads to Raman scattering of adsorbed molecules[Otto, 2005]. A third possible model for chemical SERS enhancement is based on the formation of "intermediate electronic states" at less than the resonant excitation frequency of the molecule, in this model, charge transfer from filled adsorbate orbitals to unfilled metal orbitals leads to intermediate states that enables resonance Raman processes which are absent in the molecule alone.[Lombardi and Birke, 2009]

ELECTROMAGNETIC ENHANCEMENT: The electromagnetic contribution to SERS enhancement comes from the localization of incident laser photons on the surface of the substrate. It also depends on nature of surface features. The Incident radiation creates an electric field on the surface of the substrate which interact with the electronic oscillations on the surface of the substrate and also the valence and conduction band of the metal creating localized surface plasmons, an incident wavelength dependent enhanced electric field emanates from the surface of the substrate.[Jones et al., 2019]

Surface plasmons Surface Plasmons (SPs) are coherent oscillations of free electron gas of metals at the interface between any two material.[Wikipedia, 2020] For surface plasmons to be excited the incident plane wave must have its frequency and parallel momentum conserved, this constraint is not obtainable in air or vacuum, hence surface plasmons are confined to the metal surface with its intensity decreasing exponentially away from the surface.[Moskovits, 1985] Surface plasmons resonance is an electromagnetic effect that occur on the flat surface of a good conductor. The frequency and parallel momentum of surface plasmons must obey the dispersion relation shown in Equation 3.5

$$\kappa_{||}^2 = (\frac{\omega}{c})^2 \mathbf{Re} \frac{\epsilon_o \epsilon}{\epsilon_o + \epsilon} \tag{3.5}$$

where ϵ_o is the dielectric function of the conductor, c is the speed of light, ω is the frequency of the surface plasmons and ϵ that of the ambient. The localized surface plasmons do not radiate except gratings are made on the substrate, by gratings it is meant that certain roughness or an ordered set of surface corrugations of different cross-section geometry be implemented. Surface corrugations of dimensions smaller or similar to wavelength of incident wave have electromagnetic resonances similar to surface plasmons at such can excite plasmons having symmetric time varying dipole that can radiate.[Jones et al., 2019]

This outward radiation is the genius of the SERS technique, Metiu and Das(1984)[Metiu and Das, 1984] observed that large signal amplification are possible when grating/-surface corrugated structure absorbs incident photons, store the electromagnetic energy into surface plasmons, due to the gratings and the new conservation rule that they introduce the plasmons are delocalized in the parallel direction of the surface and localized in the perpendicular direction.

3.4 SERS SUBSTRATES

SERS substrates are the flat physical platforms in which antibody-antigen reaction takes place, in other to achieve trace level detection of analyte on these substrate, it is therefore desirable that intricate design paradigms be developed to enable both chemical and electromagnetic enhancement of raman signals from the surface. SERS substrates also can be modified with appropriate amine/thiol/carboxyl chemistry to become capture substrates, the unmodified substrates can be metallic, non-metallic or a suspension of silver and or gold nano-particles in solution.[Wang et al., 2017]

Hydrophobic surface structures of multiple evenly spaced nano/micropillars for concentration of analytes can be incorporated onto the SERS substrate. More recently Graphene has been successfully implemented as a SERS substrate for signal reproducibility. Nanostructuring of noble metals on metallic or non-metallic surface is possible with the aid of micro-lithographic techniques like Electron beam induced deposition Electron beam Induced deposition (EBID).

Chemical properties of different SERS substrate vary, gold nano-particles immobilized on a surface manifest as neutral gold atoms that binds readily with the thiol and carboxyl group, however silver nano-particles express themselves as a posi-

Substrates	Linkers/Spacer	Range(nm)
Rough Ag Film [Pilot et al., 2019]	Polymethylmethacrylate (PMMA)	0-12
Ag Islands[Pilot et al., 2019]	Langmuir-Blodgett films of Arachidic Acid	0.85-14
Ag Nanorod [Pilot et al., 2019]	DNA Oligomer	1-6
Rough Ag Film [Pilot et al., 2019]	linear Aliphatic Thiols	0.8-2.5

Table 3.1: Various spacers/linkers available for immune substrate modifications

tively charged silver ion that can accept an electron to form a coordination bond, making it more reactive and potentially unstable.[McNay et al., 2011]

3.4.1 Effects of Distance on SERS Enhancement

The proper understanding of the effects of distance is crucial for obtaining a sufficient electromagnetic SERS enhancement, the electromagnetic theory of SERS enhancement predicts that adsorbate have to be within a a given sensing volume for efficient enhancement. In antibody-antigen reaction spacers and linker molecules are employed to immobilized antibodies to the SERS substrate or to immobilize the raman active labels to noble metals[Dick et al., 2000]. see table 3.1 for a table of spacers for substrates and their effective range.

The magnitude of the electric field that extends from the SERS surface due to the excitation of the localized plasmons decreases exponentially with increase in the distance of the molecule from the surface increases. Theoretically, the field enhancement around a nano-sized noble metal decays with r^{-3}, the overall distance dependence scales as r^{-12} with Electric field(E). Experimentally with increase in surface area due to shells of molecule aggregating, a r^{-10} dependence is observed.

Roberto et al. estimated that the target molecule should be at a distance of 10nm or less for plasmonic effect to result in maximum electromagnetic enhancement[Pilot et al., 2019].

4 PROTEIN STRUCTURES AND VIBRATIONS

In Section 2.1 it was established that the SAR-COV-2 virus is a protein, broadly speaking viruses and toxins are proteins. Each of these viruses have a structure, some similar and others different. This chapter aims to detail the basics of protein structure and the resulting inelastic vibrations of such a structure when probed with a laser.

Amino acids are a collection of compounds that serves as sub-constituents or building blocks of peptides and proteins. An amino acid consists of a central carbon knows as the α-Carbon, to this central carbon an amino group and a carboxyl group is attached(see Figure 4.1 for a schematic of amino acid structure).[noa, 2020a] Variation in different Amino acids is conferred R groups know as the side chain. The R group for each amino acids usually differ in structure, electrical charge, and polarity. see Figure 4.2 for the complete chart of amino acids building blocks. Protein

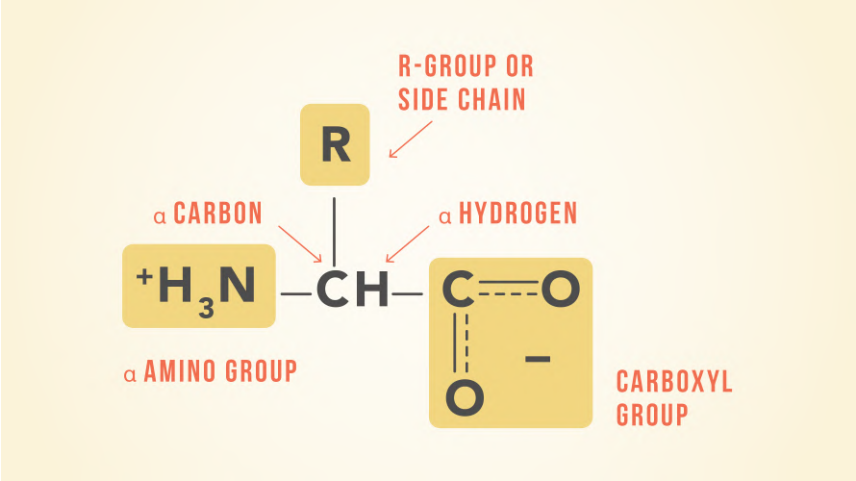

Figure 4.1: Schematic Structure of Amino Acids[Networks, 2021]

structures are formed when an amino acid acting as a monomer(repeating unit) is arranged into a three-dimensional structure. Proteins are formed by a condensation process, whereby amino acids lose a water molecule per reaction in order to create a peptide bone with another amino acids. By convention, a chain of 30 amino acids and above is identified as a protein and less a peptide. [Networks, 2021]

4.1 PROTEIN CONFORMATION

Protein conformation entails the entire arrangement of its constituent atoms in space, conformational arrangement is brought into existence by bonds(Hydrogen bonds, Van der waals.) within the interacting amino acids. Changes in conformational arrangement are driven by environment conditions like pH, temperature, hydrophobicity and hydrophilicity of medium. [Blackstock, 1989]

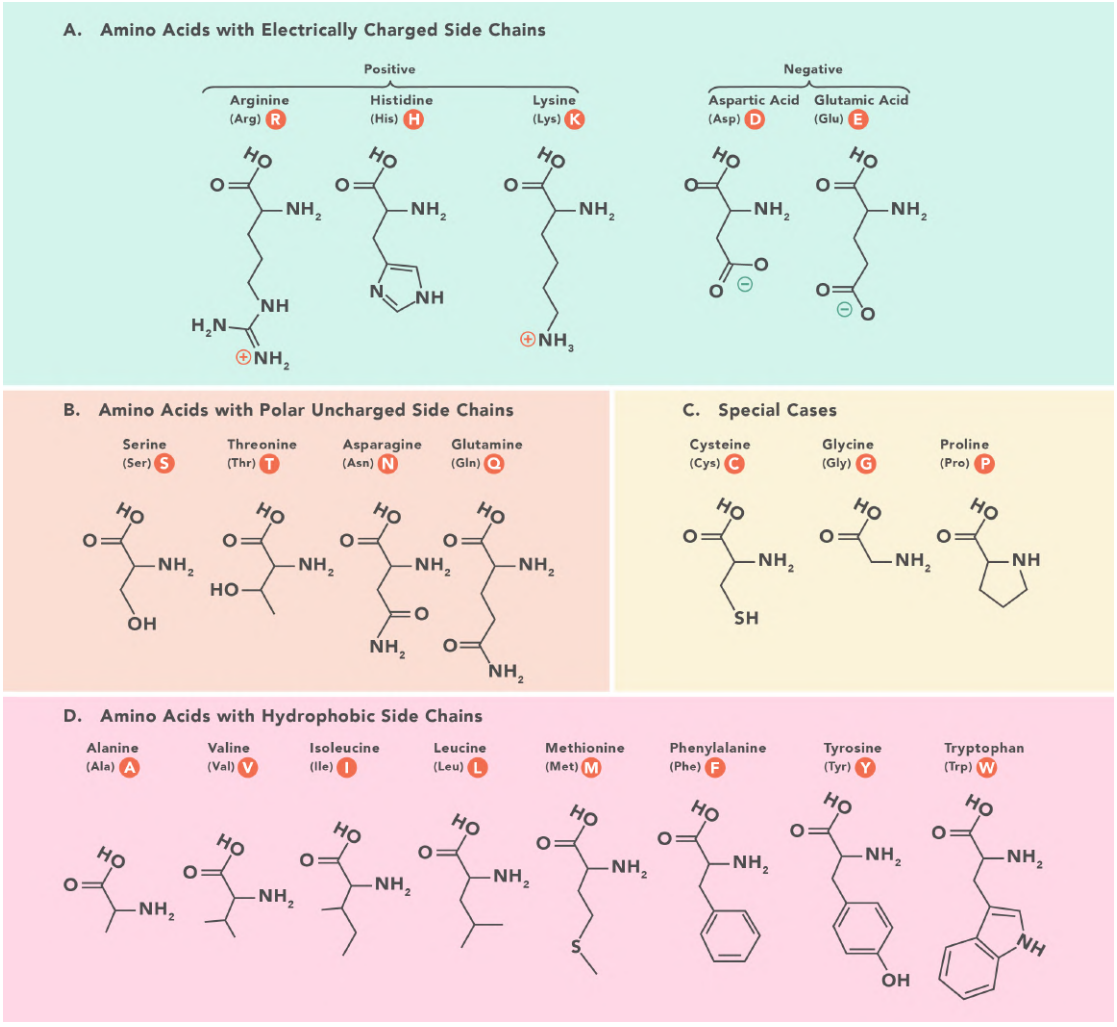

Figure 4.2: Chart of Amino acid building blocks[Networks, 2021]

4.1.1 Secondary Structure

Adjacent Amino acids in the polypeptide backbone(The backbone is the amino acid chain without the aliphatic group R) can interact via hydrogen and weak van der waals forces to give secondary structures like the α-helix and β-pleated sheet see Figure 4.3, these secondary structures are formed by hydrogen bond between the carbonyl O of one amino acid and the amino H of another.

In an α-helix conformation, the protruding R group interacts freely, the helical(curled ribbon) morphology of this protein conformation comes the bonding of carbonyl group (C=O) of one amino acid to the hydrogen bonded of an amino group H (N-H) of an amino acid that is four steps down the chain. Within each turn of the helix in this conformation are found 3.6 amino acids.[KhanAcademy, 2021]

The pleated sheet conformation proceeds from hydrogen bonding between the carbonyl and the amino groups of two or more segments of polypetide chain align next to each other. The R groups in this conformation extends above and below the plane of the sheet. [bioinformatics, 2021]

4.1.2 Tertiary Structure

The overall three-dimensional structure of monomeric and multimeric protein molecules as shown in Figure 4.4 is embodies in the tertiary structure. Morphologically this structure consist of α-helixes and β-pleated-sheets folded into a compressed glob-

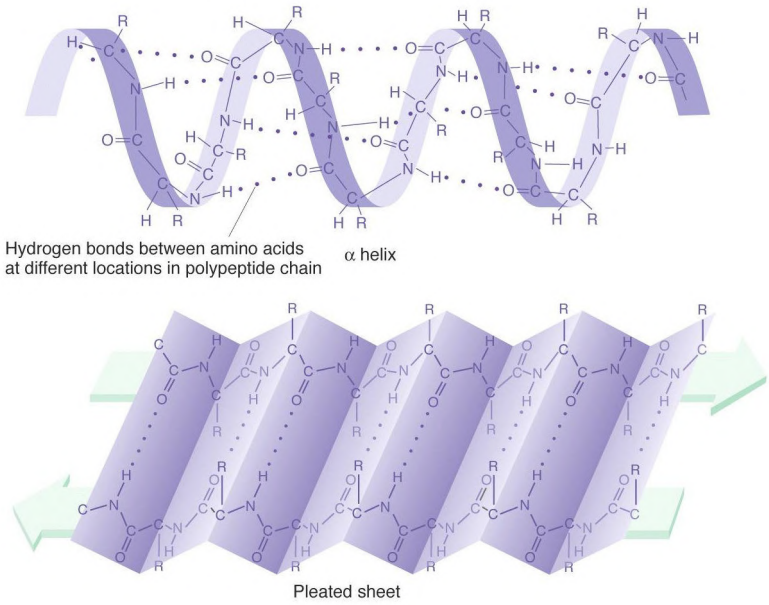

Figure 4.3: α-Helix and β-plated sheets[Carr, 2021]

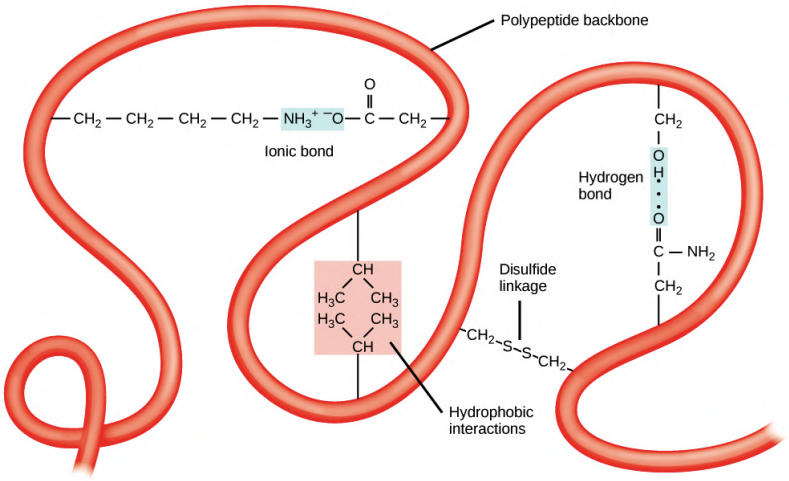

Figure 4.4: Schematic of the tertiary Structure of Proteins[KhanAcademy, 2021]

ular structure. The folding and stability is governed by the whole gamut of no-covalent bonds and non-specific hydrophobic interactions.[Lubrizolcdmo, 2019]

4.2 VIBRATION OF PROTEINS

Proteins are biomolecules held together by different kind of bonds, namely, covalent, hydrogen, Van-der-Waals bonds e.t.c A molecular bond can be idealized as a spring connecting two masses. Such as system will have a spring of K, equilibrium distance between nuclei of each atom in the bond to be x. The potential energy(U) of such a system is given by

$$U_{PE} = \frac{1}{2} \cdot K_{spring} \cdot x^2 \tag{4.1}$$

To define the Vibrational energy of this idealized system, the Erwin schrondinger (Equation 4.2) from wave mechanics is applied to the potential of the molecular bond.

$$\frac{-\hbar}{2m} \cdot \frac{d\psi^2 u}{dx^2} + \frac{1}{2} \cdot K \cdot x^2 \psi = E_{vib}\psi \tag{4.2}$$

ψ is the wave-function of the system, E_{vib} is the vibration energy, and mass m represents the reduced mass of the atoms involved in the vibration, given by

$$m = \frac{m_1 \cdot m_2}{m_1 + m_2} \tag{4.3}$$

Solving Equation 4.2 reveals that molecular vibrations and energies are quantized. The vibrational energies are given by

$$E_v = (\nu_{qnum} + \frac{1}{2}) \cdot \hbar\sqrt{\frac{K}{m}} \tag{4.4}$$

where ν is the quantum number of the vibrational mode.

Biomolecules vary in size, mass, and equilibrium spacing of atom. Bonds involving larger atoms or groups of atoms will vibrate with lower vibrational energy due to increase in the reduced mass.[Shipp et al., 2017]

The vibrational energy of the carbon-hydrogen (C-H) bond with equilibrium spacing between nuclei of 109pm is $411Kj/mol$ while carbon-carbon (C-C) vibrations with equilibrium spacing of 154pm has a bond energy $346Kj/mol$.

Double and triple bonds vibrations can be idealized as a system with a higher stiffness as compared to single bonds, higher stiffness translates to higher bond strength.

Carbon double(C=C) and triple bond($C \equiv C$) vibrations have bond strengths of $602Kj/mol$ and $835Kj/mol$ respectively. The aforementioned bond types are not the only bonds found in bio-molecules, several bond types with different vibrational mode exist, modes like stretching, rocking, bending, twisting, scissors, wagging and out-of-plane have be observed. For effectiveness of raman scattering several bonds have to be involved in a vibrational mode. In-phase stretching or shortening enables constructive interference of electric dipoles formed by the molecule, this in-plane constructive interference is seen in the breathing of nucleic acid base and ring shaped molecule like benzene [Turrell and Corset, 1996].

Raman spectrum of biological samples can be differentiated into three sub-regions. The fingerprint, silent and high wavenumber region. The fingerprint region encompasses 600 and $1800cm^{-1}$, this region is characterized by a diversity of narrow peaks and other localized features that fingerprints the biomolecule. It is the region of a raman spectral most useful for chemometric analysis. Any band below the $600cm^{-1}$ wavenumber region is usually attributed to very large non-biological atoms. The Silent region spans from 1800 to $2500cm^{-1}$. Small atoms lead to high energy vibrations in the region from 2500 to $3400cm^{-1}$

The Raman Spectrum of a protein molecule show some characteristic features that are inherent of its constituent molecular structure, since proteins are built up from repeating units of amino acids, the observed spectrum of several proteins show some unique features summarised as the Amide I, Amide II and the Amide III bands, other bands on the Raman spectrum can be due to Disulphide bonds, Cysteine, Tyrosine, phenylaniline, Tryptophan and Aliphatic side chain groups. Details of these bands, vibration mode and their corresponding wavenumber will be discussed below.

4.2.1 Disulfide Bond

The local environment of the protein can be analyzed via the stretching vibration of the cysteine sulfhydryl(S–H) bond. The sulfhydryl Raman bands occurs in a region

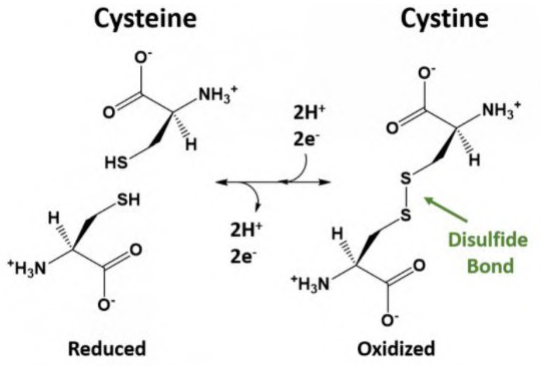

Figure 4.5: Cysteine Oxidation to Produce Disulfide Bonds[Chemistry, 2021]

Band Frequency	Vibrational Mode	Local Environment and Conformers
>2585[Wen, 2007]	Free S–H stretch	Exposed
2575[Wen, 2007]	Weakly H-bonded	Partially exposed
2565[Wen, 2007]	Moderately H-bonded	Partially exposed
<2560[Wen, 2007]	Strongly H-bonded	Buried
704[Wen, 2007]	C–S stretch	Trans conformer
655[Wen, 2007]	C–S stretch	Gauche conformer
540–545[Wen, 2007]	S–S stretch	TGT conformer
523–528[Wen, 2007]	S–S stretch	GGT conformer
508–512[Wen, 2007]	S–S stretch	GGG conformer

Table 4.1: Raman frequencies assignment of the Sulfhydryl with correlating Hydrogen Bonding Status and Disulfide Bond conformations Different Conformers. [Wen, 2007]

of the spectrum (2500 to 2600 cm^{-1}), correlations between sulfhydryl hydrogen bonding and the S–H stretching frequency are detailed in the Table 4.1 below.

Free cysteines are oxidized and linked as shown in Figure 4.5 to form disulphide bonds. Raman markers of disulfide bonds are found in the low frequency region of 450 to 700cm^{-1}. The CCSSCC moiety at the connection point influences the frequency of the C–S stretch and S–S stretch mode of the disulfide bridge. Several conformations of the disulfide bridge are possible, Table 4.1 summarises these possibility. The Gauche-Gauche-Gauche Conformation of Cysteamine Hydrochloride (GGG) isomer is the most stable and the Gauche-Gauche-Trans Conformation of Cysteamine Hydrochloride (GGT), Trans-Gauche-Trans Conformation of Cysteamine Hydrochloride (TGT) isomers the next.[Wen, 2007]

4.2.2 Amide Conformation Bands

The Amide Conformation band in the fingerprint region of a protein Raman spectrum is key to determining the secondary structure of protein (-helix, -sheet, turn, random coil e.t.c). Amide bands are grouped into amide I, amide II(difficult to detect), and amide III bands. Table 4.2 details the different designations and correlations of the amide bands. [Krimm and Bandekar, 1986].

Band Frequency	Amide Bands	Vibrational Mode	Secondary Structure
1680[Wen, 2007]	Amide I	H-bonded C=O stretch	β-turn
1670–1680[Wen, 2007]	Amide I	H-bonded C=O stretch	β-sheet and β-barrel
1650–1655[Wen, 2007]	Amide I	H-bonded C=O stretch	α-Helix
1640[Wen, 2007]	Amide I	H-bonded C=O stretch	loose β-sheet
1300–1340[Wen, 2007]	Amide III	N–H and C–H bend	α-Helix
1260[Wen, 2007]	Amide III	N–H and C–H bend	Disordered
1235–1250[Wen, 2007]	Amide III	N–H and C–H bend	β-sheet
930–950[Wen, 2007]	Skeleton	$N–C_{\alpha}–Cstretch$	α-Helix

Table 4.2: Raman Band Frequencies of Amide Conformation bands. [Wen, 2007]

Band Frequency	Amide Bands	
0.30	Donor of strong H bond	[Siamwiza et al., 1975]
1.25	Donor of strong H bond	[Siamwiza et al., 1975]
930–950	Skeleton	[Siamwiza et al., 1975]
6.70	No hydrogen bond and hydrophobic	[Arp et al., 2001]

Table 4.3: Correlation of Tyrosine Hydrogen Bonding and the Fermi Doublet Intensity Ratio

4.2.3 C-C Stretching Vibrations

The secondary structure can also be characterize by looking at the C-C stretching vibrations near 890–1060cm^{-1}, the bands from 890–945cm^{-1} and 1020–1060cm^{-1} correlates to α-Helix and β-sheets respectively.[Herrero, 2008]

4.2.4 Tryptophan

Raman bands identifying the Tryptophan residue are not sensitive to structure, wavenumbers identifying Tryptophan includes 544, 577, 760, 879, 1014, 1340, 1363, 1553, and 1582cm^{-1} [Aubrey and Thomas, 1991; Combs et al., 2005]. When the ratio of intensities I_{1360}/I_{1340} is low it indicates that the tryptophan is involved in the Hydrogen bonding in a hydrophilic environment, a high ratio indicates an hydrophobic environment.

4.2.5 Tyrosine

The presence of tyrosine is indicated by peaks at 850 and 830cm^{-1} of a protein Raman spectrum. The peaks at I_{850}/I_{1830} forms a tyrosyl doublet [Siamwiza et al., 1975], Siamwiza established the correlation between the tyrosyl doublet and the hydrogen bonding state of the phenolic group.

4.2.6 phenylaniline

Phenylalanine can be viewed as a phenyl group in place of a terminal hydrogen of alanine , its vibration is captured as a benzyl ring breathing mode, it shows a Raman band at 1003–1006cm^{-1}. The ring breathing mode is insensitive to its inherent conformation environment making phenyaniline useful for the normalization of protein Raman spectrum [Barrett et al., 1987].

4.2.7 Aliphatic Side Chain

Aliphatic side chains are non-polar and hydrophobic, Figure 4.6 shows the possible vibration modes of these groups. The bending vibrations of CH_2 and CH_3 is observed near $1450cm^{-1}$. (Lippert et al., 1976). The C-H stretching bands [CH_2 groups ($2860cm^{-1}$, $\nu_s CH_2$), $\nu_{as} CH_2$ and $\nu_s CH_3(2935cm^{-1})$, and $\nu_{as} CH_3(2970cm^{-1})$]. [Verma and Wallach, 1977].

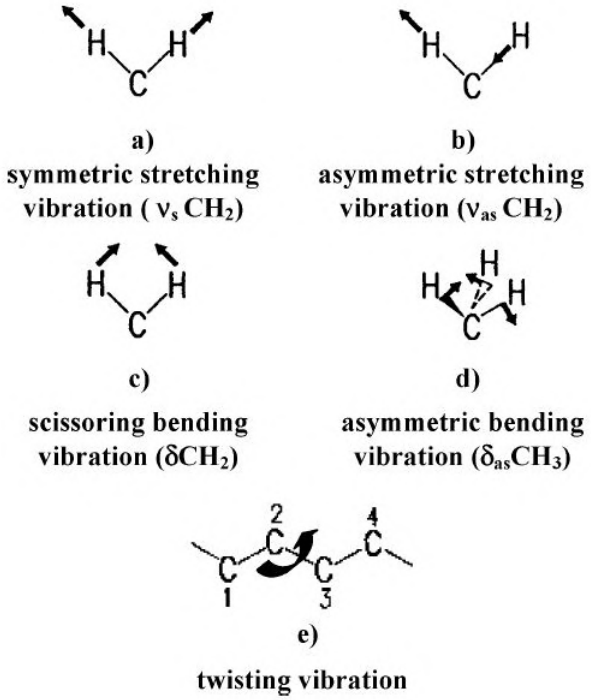

Figure 4.6: Pictorial scheme of Aliphatic vibration modes of proteins a) and b) symmetric and asymmetric stretching vibration; c) and d) scissoring and asymmetric bending vibration; e) twisting vibration.[Herrero, 2008]

5 SURFACE ROUGHNESS AND HEIGHT PROFILOMETRY

In immunoreactions a surface is required for the antibody and antigen to interact, since this surface is exposed to the environment, it can be viewed as a solid–gas or solid–liquid interface. Regardless of the method of Solid Surfaces preparation, it is definitely going to contain irregularities, undulations and protrusion [Bhushan et al., 1995]. These irregularities can be of micro and nano length scales, since there is variation of heights across the surface, a rough surface results. In some cases this is unwanted, but in SERS based studies a rough noble metal coated surface is desirable. A sufficient spread of roughness allows for appropriate SERS signal enhancement off the noble metal surface.

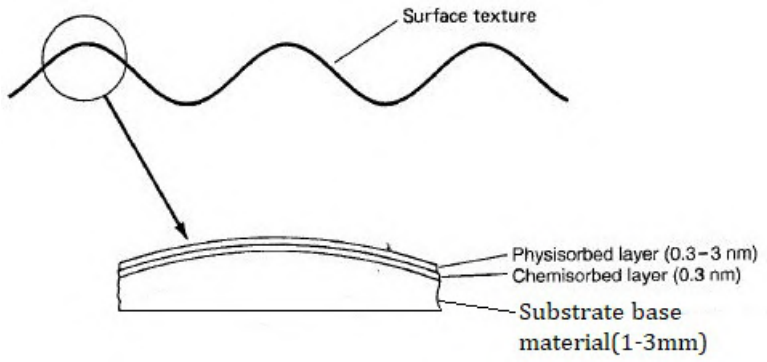

Figure 5.1: Typical surface layers[Bhushan, 2000]

Noble metals are chemically unreactive until activated, like metals and alloys, oxide layers form on the surface noble metals while in air, and in other environments they are likely to form layers of sulfides and chlorides [Bhushan, 2000]. Other specific layers can be intentionally attached on the noble metal surface to achieve a given function, thus leading to an overall surface morphological alteration.

5.1 ANALYSIS OF SURFACE ROUGHNESS

The three-dimensional topography of a surface is captured in the random or repetitive deviations from the nominal surface texture, surface texture includes (1)lay, (2) waviness, (3) roughness (nano- and microroughness), and (4) flaws. Figure 5.2 is a pictorial representation of a surface texture with unidirectional lay, Lay embodies the principal directional vector of the main surface pattern. Waviness are a product of vibrations, chatter and heat treatment during manufacturing or in finishing of stock material, irregularities produced by waviness have spacing's that are greater(longer wavelengths than micro-roughness) than the characteristic roughness sampling scale for the given surface.[Tripp, 1998] Nano- and microroughness are surface irregularities of short wavelengths, it is a collection of peaks and valleys with varying amplitudes and spacings.

Flaws are unintended and unwanted corrugations and or deformations in the surface texture.

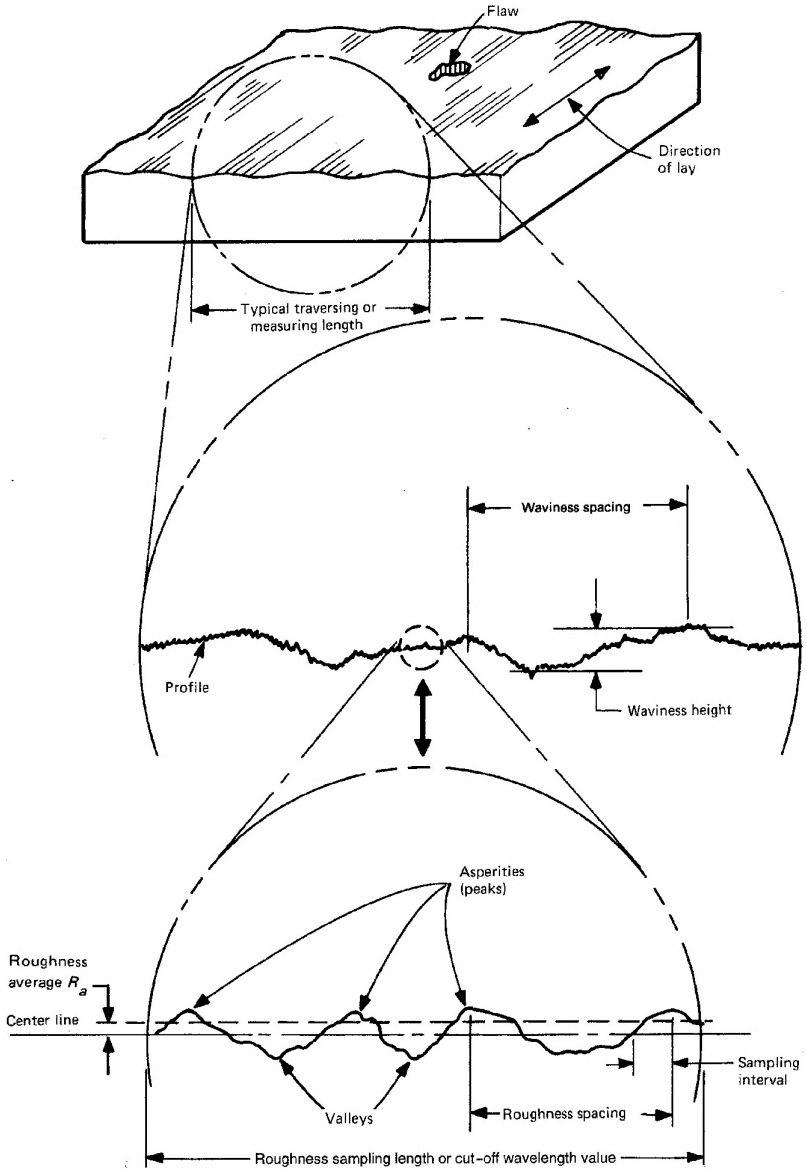

Figure 5.2: Pictorial representation of surface texture. [ASME, 2020]

Surface textures of noble metals used in SERS based immunoreactions usually random, can be isotropic or anisotropic, and either Gaussian or non-Gaussian. The very nature of such surface height distribution depends upon the cumulative production steps and the nature of the processing method.

5.1.1 Average Roughness Parameters

Quantification of Surface roughness is essential in order to have measures for comparing surfaces. This quantification is usually done with respect to a reference plane(surface maps) or along a single line profile. These heights and roughness measurements are done withe aid of white light inteferometry, Atomic force microscope(Atomic Force Microscope (AFM). The American National Standards Institute American National Standards Institute (ANSI) and the International Standardization Organization International Standards Organisation (ISO) have put forward two statistical height descriptors, namely (1) R_a , Center line Average (CLA) (center-line average), and (2) the standard deviation or variance (σ), or root mean square Root Mean Square (RMS) R_q. Other measures of height descriptions like R_z(average peak-

to-valley height) R_p (maximum peak height), R_v (mean-to-lowest valley height or maximum valley depth), and R_{pm}(average mean peak height) exist but are seldom used. Figure 5.3 is an idealizd profile z(x), with profile heights measured from a reference line.

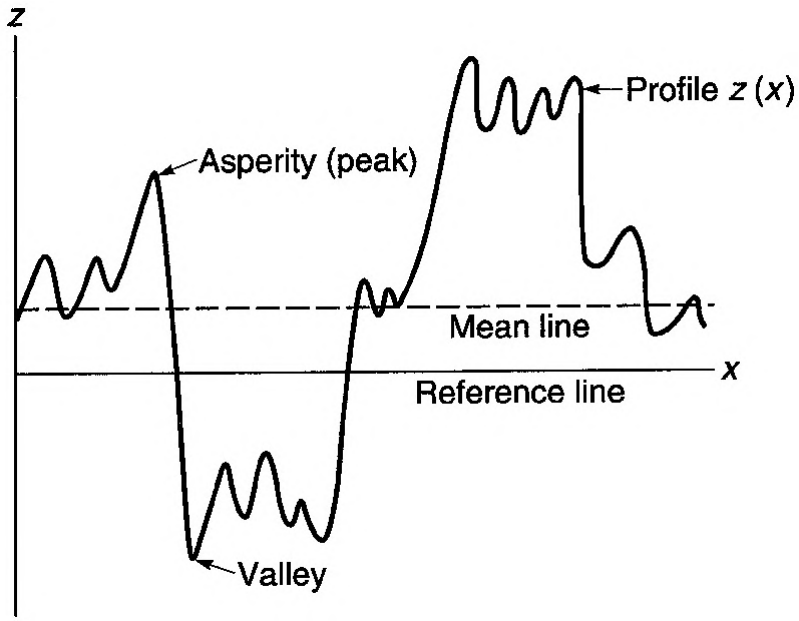

Figure 5.3: An Idealized surface profile z(x).[Bhushan, 2000]

The center line is defined in such a way that the area above and below the main line with respect to the bounding profile z(x) is the same. By this definition R_a, CLA becomes the arithmetic mean of the absolute values of all local maximum and minimum from the mean line through the profile. A standard deviation σ is calculated as the square root of this arithmetic mean.

Mathematically :

$$R_a = \frac{1}{L}\int_0^L |z-m|\,dx, m = \frac{1}{L}\int_0^L z\,dx \tag{5.1}$$

L is the Sampling length of the profile, The variance of height referenced from the mean line is calculated as,

$$\sigma^2 = \frac{1}{L}\int_0^L (|z-m|)^2\,dx = R_q^2 - m^2, \tag{5.2}$$

σ and R_q is given by

$$R_q^2 = RMS^2 = \frac{1}{L}\int_0^L z^2\,dx \tag{5.3}$$

Table 5.1 details other parameters for quantifying a surface, four broad parameter groupings can be identified namely height, spatial, hybrid and functional.

5.2 WHITE LIGHT INTERFEROMETRY

White light interferometry uses polychromatic light of wavelength range 400 to 750nm to effect measurements[Kino and Chim, 1990].

Classical interferometry employs fringe analysis and phase shifting interferometry Phase Shifting Interferometry (PSI) techniques. The PSI measurement range

Category	Parameter	Description
Height parameters	Sq	Root mean square height
	Ssk	Skewness
	Sku	Kurtosis
	Sp	Maximum peak height
	Sv	Maximum pit height
	Sz	Maximum height
	Sa	Arithmetical mean height
Spatial parameters	Sal	Auto-correlation length .
	Str	Texture aspect ratio
	Std	Texture direction
Hybrid parameters	Sdq	Root mean square gradient
	Sdr	Developed interfacial area ratio
Functional parameters	Smr(c)	Areal material ratio
	Smc(mr)	Inverse areal material ratio
	Sk	Core roughness depth
	Spk	Reduced peak height
	Svk	Reduced valley depth
	Smr1	Peak material portion (percentage of material that comprises the peak structures associated with Spk).
	Smr2	Valley material portion (percentage of the measurement area that comprises the deeper valley structures associated with Svk).
	Svq	Slope of a linear regression performed through the valley region .
	Spq	Slope of a linear regression performed through the plateau region.
	Sxp	Peak extreme height.
	Smq	Relative areal material ratio at the plateau to valley intersection.

Table 5.1: Surface Texture parameters[Chittaranjan Sahay, 2018]

is limited in practice to $\lambda/4$, for samples with surface features exceeding this limit(Spatially difference in feature height across and along adjacent sampling points), surfaces discontinuities cannot be captured as fringe ambiguity occurs.

White light is employed to measure surface roughness hence its importance in industry for metrology and quality control [Koch, 1998]. Coaxial illumination and observation ensure that deep cuts and holes can be measured, also no shadows appear. Height profile and roughness of Large measurement areas can be captured through lateral scanning of a partition surface an subsequent stitching of the partition acquisitions [Dresel et al., 1992]. Measurement uncertainty in white light interferometry is about $1\mu m$ and is largely influenced by the nature of the object surface.

5.2.1 Measurement in a White Light Interferometer

White light interferometry makes use of Michelson interferometer [Kino and Chim, 1990]. This setup is schematically illustrated in Figure 5.4(a), A beamsplitter splits white light from a source into two beams, one beam reflects off the reference mirror and the other off the object mirror. The reflected beams are added together and directed to a screen. Altering the object mirror in the z-axis direction results in variation of light intensity on the screen(A relation called Correlogram) [Larkin, 1996]. Figure 5.4(b) shows the intensity dependence on the position of the object mirror.

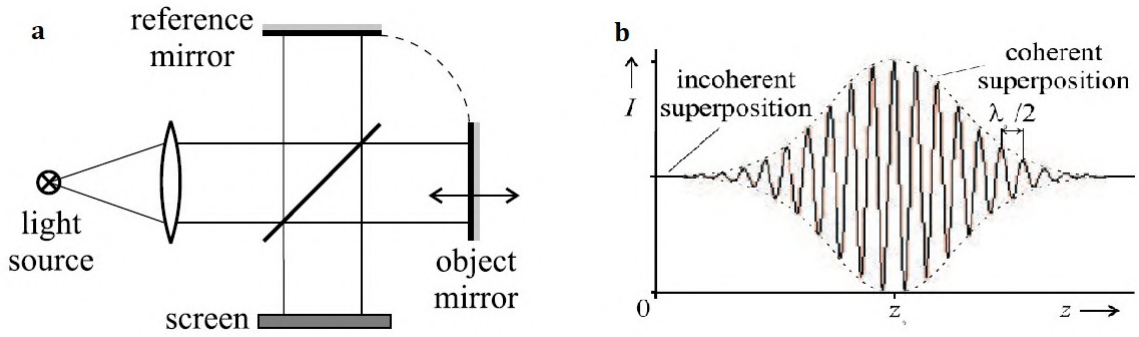

Figure 5.4: (a)Michelson Interfereometer Setup (b)Intensity dependence on the object mirror position.[Bhushan, 2000]

Coherent superimposition of white light is only possible at the Z_0 position, where the optical paths of light from the beamsplitter to the reference mirror and to the object mirror are the same.

Modulation of light intensity proceeds from the correlogram width, this width is is determined by the vertical distance span of the object mirror, Light source with large spectral width are desirable for white light interferometry because they allow for a correlogram width having a broad period of the intensity modulation.

With a reference to a light source with a Gaussian distribution, the relationship between the coherence length, spectral width and correlogram width is derived from the normalized spectral density which takes takes the form of Equation 5.4:

$$g(\nu) = \frac{1}{2\sqrt{\pi}\Delta\nu} \cdot exp[-(\frac{\nu - \nu_o}{2\Delta\nu})^2] \tag{5.4}$$

$\Delta\nu$ stands for the effective band width. The degree of coherence becomes:

$$\gamma(\tau) = exp(-4\pi^2\tau^2\Delta\nu^2)exp(-i2\pi\nu_o\tau) \tag{5.5}$$

The summed up light at the detector is written as

$$I(z) = I(0)1 + exp[-(\frac{Z - Z_o}{l_c})^2]cos(4\pi\frac{Z - Z_o}{\lambda_0}) \tag{5.6}$$

where l_c is the coherence length

$$l_c = \frac{c}{4\pi\Delta\nu} \tag{5.7}$$

$\lambda_o = c/\nu$ represents the mean wavelength and c the speed of light. Equation 5.6 is the equation of the correlogram.

6 MICROFLUIDICS

In the spirit of the miniaturization movement, Andreas Manz et al[Convery and Gadegaard, 2019].presented a seminal paper in 1990, they proposed a device that could automatically perform several of the functions in biological analysis: functions like sampling, transport of the analytes, analyte preparation, analyte separation, chemical reactions, cleaning, as well as detection. Manz and his team immediately appreciated that such a system will function better if it is physically realised on the micro-scale, they identified that many channels fabricated onto an appropriate substrate will lead to faster reactions, simultaneous biological analysis and a larger surface to volume ratio for proper mixing of analytes. Hence they coined the term "miniaturized Total Analysis System" μTAS for such a system.[Manz et al., 1990] This influential paper of Manz and his team proved the possibilities of microfluidics devices and laid the groundwork for the current paradigm of microfluidics device used in POC testing and other lab on chip applications Lab on Chip (LOC).[Jenkins and Mansfield, 2013]

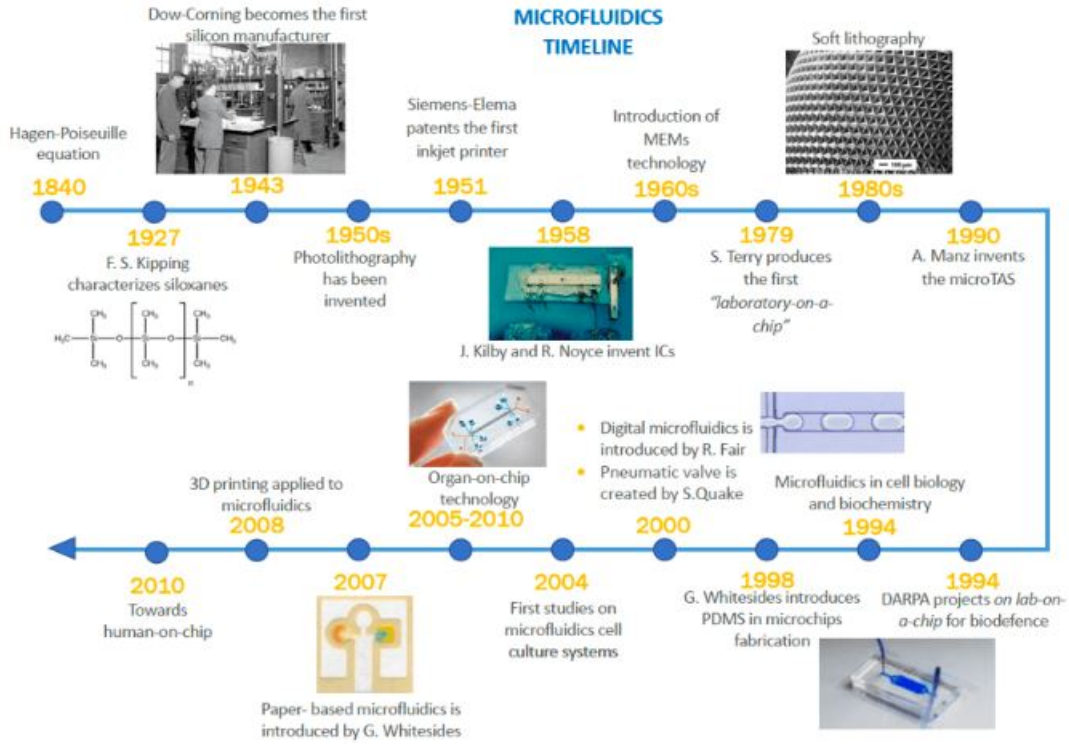

Figure 6.1: Microfluidics timeline[Elveflow, 2021]

Microfluidics is a multidisciplinary field combining advances in physics, biology, chemistry, nanotechnology and biotechnology.[Ducrée, 2012] Microfluidic chips are portable devices of a few centimeters that usually contains valves, micro-channels, reaction chambers, pressure systems, and detection systems/surface. The inherent micrometer sized micro-channel guarantees that only low amounts(of the order of a $\leq$ few micro-liters) of sample/analyte will be used for the intended assay, leading to fast analysis.

The flow of samples/analytes in any given microfluidic channel is laminar(to be discussed later in this chapter) From a standpoint of safety, microfluidic chips are safe platforms for chemical, radiological, and biological studies due to low volume of sample.[Simpson et al., 1998] This serves to ensure that POC device are safe for use in the context of global health. Microfluidics has found widespread application in DNA chips, lab-on-a-chip technology and point of care devices. [wikipedia, 2020a]

Figure 6.1 shows the evolution of microfluidic devices from 1840 with the derivation of the Hagen-Poiseuille equation to 2010 where attention is now moving towards human-on-chip applications. In other to be able to achieve the lofty heights of total biological analysis microfluidic systems are embedded with some action components like valves, pumps, mixers, reaction chamber, detectors e.t.c.

6.1 FLUID AT SMALL SCALE

Fluid flowing in microfluidic channels are confined(length, breadth and height) in structures of micrometer scale(structures with dimensions less than one meter). The dominant forces at play in these dimensions are different from those in the macro-scale, most often intricate flow and force behaviours are utilized to perform functions in the microfluidic devices.[Purcell, 1977]

Fluids usually refer to liquids and gases. Density(ρ)-which is the mass per unit volume serves to characterize different fluids. A second property crucial to understanding flow response of fluids is viscosity(μ)-which is a measure of the tangential reluctance of fluid elements/layers to flow with respect to each other or a boundary. Viscosity is directly proportional to shear stress(τ) in the fluid. Equation 6.1 is a linear relation that defines the shear stress of Newtonian fluids, where du/dy is the velocity gradient between adjacent layers of fluid elements.[Beebe et al., 2002]

$$\tau = \mu \cdot \frac{du}{dy} \tag{6.1}$$

A majority of biological Macro-molecules such as blood and aqueous solutions of proteins show a non-linear relationship between shear stress and viscosity and the velocity gradient, hence they are termed non-Newtonian fluids. [Inc, 2021]

Most fluid flow in microfluidic channels are in-compressible, that means fluid density remains constant throughout the length of the micro-channel, hence the background reference pressure cannot affect flow dynamics. The incompressiblity assumptions holds true even when a pressure change of a few atmospheres is observed. In long microfluidics channels where fluid pressure can decrease by as much as 20%, compressiblity becomes important.

To better understand the dynamics of in-compressible fluid flow in macro and micro-channel the velocity field has to be resolved by solving the Navier-Stokes equations.(see Equation 6.2 and Equation 6.3)

$$\frac{\partial u}{\partial t} + (u \cdot \nabla)u = \frac{-1}{\rho}\nabla p + \nu\nabla^2 u + f \tag{6.2}$$

$$\nabla \cdot u = 0 \tag{6.3}$$

u represents the fluid velocity field, ρ is stands for density, p is the pressure field, ν is the kinematic viscosity and f is the external acceleration field.[Fluigent, 2021]

In microfluidics dominant effects include laminar flow, fluidic resistance, Surface area Effect, surface tension, diffusion and convection.

6.2 REYNOLDS NUMBER(RE)

Reynolds number is an important dimensionless number in fluid mechanics. It is used to characterize different flow regimes in macro and microchannels. Derived as the ratio of inertia forces to viscous forces in a fluid due to differential fluid velocities. Reynolds number is not an inherent property of a fluid but a statement of force interaction and the consequent effect of such interactions.[wikipedia, 2020c]

$$Re = \frac{\rho \cdot U \cdot L}{\mu} \tag{6.4}$$

where ρ is the density, U repersents the velocity, μ is the dynamic viscosity of the fluid in motion and L is a characteristics geometric properties (L).

Reynolds number predicts two regimes of fluid flow, the laminar and the turbulent regime. In microfluidics, laminar flow is the predominant flow regime, in this regime Re<2300 as calculated by Equation 6.4 is always less than 2300. In the laminar region the right size of the navier stokes equation prevails(see Equation 6.5).

$$\nu \nabla^2 u = \frac{-1}{\rho} \cdot \nabla p - f \tag{6.5}$$

as the Re increases towards 2300, a transition region manifest where an observable progression to chaos is identified, beyond this Reynolds number, that is when Re>2300 flow becomes turbulent and unpredictable(see Equation 6.6). [Sharp et al., 2005].

$$\frac{du}{dt} + (u \cdot \nabla)u = f \tag{6.6}$$

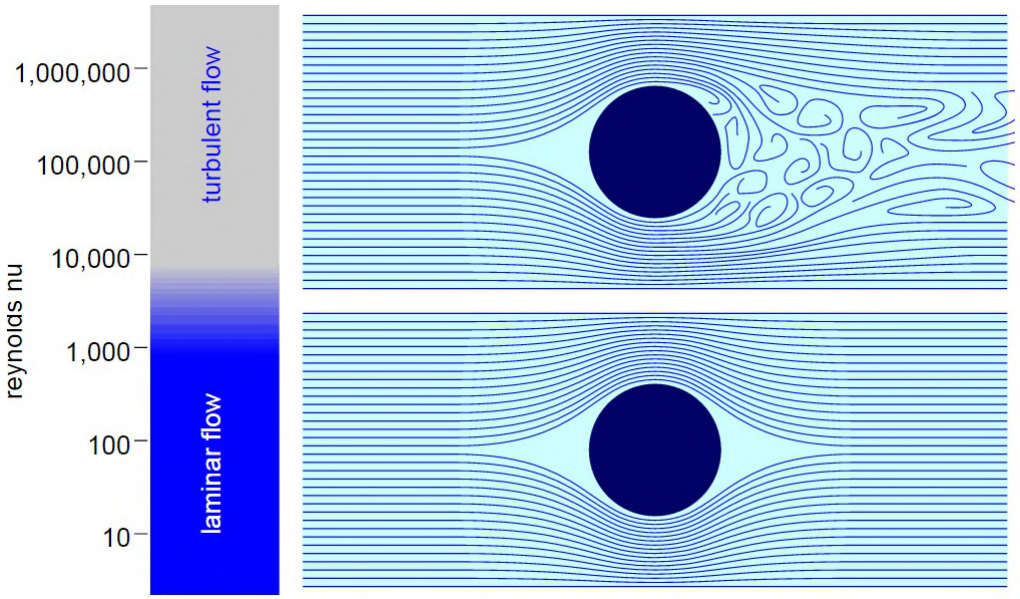

Figure 6.2: Schematics of Laminar and Turbulent flow in a channel [Physics, 2021]

Figure 6.2 shows a schematic representation of the aforementioned fluid flow regimes.

DIFFUSION: In the context of immunoreactions, Diffusion is the process by which antibodies and or antigen will move from a source area to the functionalized area for chemisorption via Brownian's motion. Brownian's motion is the random motion of particles dissolved in solution as a result of their collision with fluid molecules.[noa, 2021] In one dimension, diffusion can be modeled by

$$d^2 = 2 \cdot Dt \tag{6.7}$$

where d represents the distance a particle moves in a given time t, and D is the diffusion coefficient of the particle. The distance transverse by a particle per time is directly proportional to the square root of the diffusion coefficient. With a decrease in diffusion distance as observed in microfluidics, diffusion coefficient(a measure of particle transport) is significantly lowered, and time for adequate/complete diffusion is greatly increased.[Beebe et al., 2002]

Since particle concentration changes with time, Adolf Fick in 1855 proposed a law of diffusion that captures this time evolution of the diffusion process, Fick's first law as it is now called states that flux moves high concentration to a sink at at a lower concentration with a magnitude that is directly proportional to the spatial derivative of concentration.[wikipedia, 2021b]

$$\mathbf{J} = -D \cdot \nabla n \tag{6.8}$$

J is the diffusion flux, D represents the diffusion coefficien, n(for ideal mixtures) is the concentration, x is the characteristic length or position.

Fick's second law predicts diffusion mediated concentration changes with respect to time. see Equation 6.9

$$\frac{\partial n(x,t)}{\partial t} = \nabla \cdot (D \nabla n(x,t)) = D \Delta n(x,t) \tag{6.9}$$

In diffusion studies two length scales are of importance:

1. From an Impulsive source: The mean squared displacement from this point source, given by

   $$\sqrt{2nDt} \tag{6.10}$$

   n is the dimension of this Brownian motion.

2. From a focused source of constant concentration: A single dimensional diffusion length, given by

   $$2\sqrt{Dt} \tag{6.11}$$

6.3 MICROFLUIDICS FOR IMMUNOASSAYS

In the past four decades, immunoassays have been used in laboratory environment, hospitals and in research to analyze biological systems by tracking the presence of, reaction of, separation of and binding of proteins, hormones, and antibodies. It involves the process of immobilization of antibodies on a substrate and its subsequent complexing with an antigen. In other to increase the surface area of reaction of the antibody and antigen, microfluidics devices are used, the channels of microfluidic device functions to guide reagents to specific location for sensing, the transport process plays a critical row in the effectiveness of the assay, as the competing process of diffusion and convection dictate this reaction kinetics and capture rate of antigen.

The immunoassay method is very versatile, new antibodies can be incorporated into an already developed microfluidic based assay method will little modification

to the microchannel design, also the assay process is fast. These potential advantages and the relatively low cost of the tools, instruments, and reagents makes the immunoassay methods, the methods of choice in many areas of bio-molecular analysis. For an assay to be said to be complete a detectable signal must be recorded as proof of the required antibody-antigen complexing.

According to different separation and detection process SERS-based immunoassays can be classified into heterogeneous or homogeneous assays. These assay types can be implemented competitively or non-competitively. The choice of a format is based on labeling chemistry, type of the analyte, and the desired dynamic range, sensitivity, and precision of the assay.[Darwish, 2006]

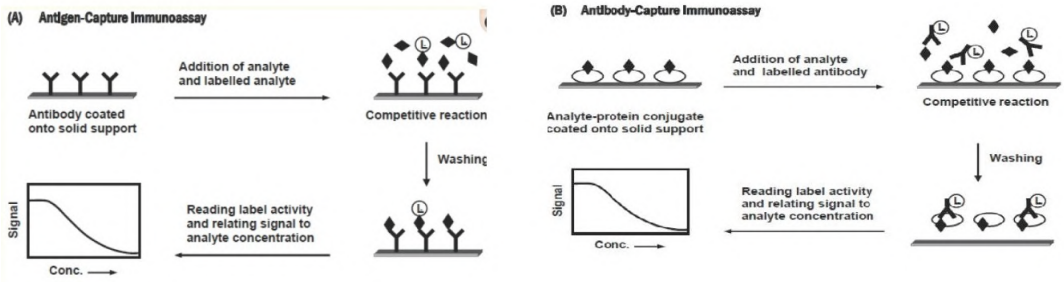

Figure 6.3: Schematics of Heterogeneous Immunoassays (A)Antigen Capture and (B)Antibody Capture Immunoassay [Darwish, 2006]

6.3.1 Heterogeneous Immunoassays

The heterogeneous immunoassay involves the use of a solid substrate or liquid micro-beads to separate bound and unbound SERS nanoprobes. A SERS probe/-marker is a SERS enhancing noble metal(Au, Ag, Cu) coated with insolubilizing linker/receptor molecules and antibodies, this conjugate reacts with a substrate coated with another insolubilizing receptor to form a solid complex of antibody and antigen. Heterogeneous immunoassay provides an excels in detection performance, reproducibility and sensitivity, but requires repetitive separation procedures.

6.3.2 Homogeneous Immunoassays

In Homogeneous immunoassays both analyte bound and unbound SERS probes compete for binding with antibodies in solution. A Binding event in this case served leads to a change in SERS-activity such that the participating samples are qualitatively and quantitatively characterised. Homogeneous assays are prone to non-specific antibodyantigen cross-reactions.

In the Competitive design of immunoassays the solid substrate can be coated with antigen or antibody such that two schemes of antigen-capture and antibody-capture are possible. The antigen-capture scheme(as shown in Figure 6.3 A) entails competition between analyte in sample and noble metal conjugated analytes for binding to a limited amount of antibodies coated on a solid substrate. After equilibration and separation, a signal can be measured from the solid substrate that is inversely related to the concentration of analyte in the sample.[Cirimele et al., 2003] In antibody-capture scheme (as shown in Figure 6.3 B), analytes in sample competes with immobilized analyte for the binding to a limited amount of antibody. In this case, the measured SERS signal from the capture substrate correlates inversely to the concentration of the analyte.

The non-competitive design is employed for binding analytes with multiple epitopes on the molecule. Hence, at least two antibodies that can bind to separate distinct epitopes is required. One of the two antibodies is bound to a substrate and the other is SERS activated with noble metal for detection.

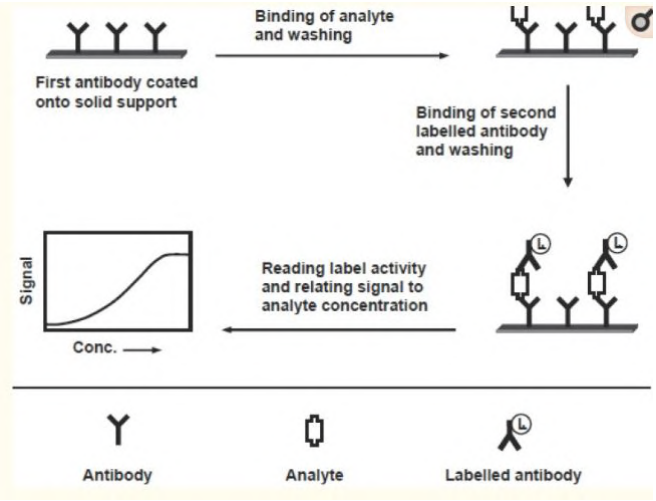

Figure 6.4: Schematics of Non-Competitive Immunoassays[Darwish, 2006]

Figure 6.4 shows the schematic of the non-competitive assay. After the desired analyte binds to the immobilized antibody, a washing step is implemented, and the washed substrate is incubated with an excess of the SERS activated noble metal coated antibody, this ensures that the remaining epitope binds to the complimentary paratope of the antibody.

On a use basis competitive immunoassays are most suitable for detecting small molecules like ion, peptide, and hormones; while the noncompetitive immunoassays is employed to analyze large macro-molecules like proteins. The sensitivity, reproducibility and dynamic range of the noncompetitive immunoassay is better than the competitive immunoassay.[Wang et al., 2017]

6.4 ANTIBODY IMMOBILIZATION

Antibody Immobilization is crucial step in the preparation for an immunoreaction, it entails the attachment of functionalizing molecules to a substrate such that the given molecule loses mobility.[Rusmini et al., 2007] The way in which proteins are immobilized affects their functionality, the performance of a POC substrate is compromised if electron transfer between antibody and antigen is not guaranteed or if the protein undergoes significant structural and conformational changes.[Faccio, 2018]

Immobilization strategy is selected based on the physical and chemical properties of both the protein and immobilization surface. The main immobilization techniques developed in the past years are based on three mechanisms: physical, bio-affinity and covalent immobilization.[Rusmini et al., 2007] Granted that immobilization process vary, bio-activity and stability proceeds from a well researched and implemented immobilization process. A careful study of several surface material, coatings, and the proteins to be immobilize can guide the tuning of surface interactions such that binding can be done using rigid or flexible linkers so as to prolong functionality through several use cycles[Mateo et al., 2007].

Indeed optimal immobilization is a complicated venture, sometimes requiring trial and error to obtain a high affinity substrate for the analyte. Orientational immobilization of proteins have proved effective in ensuring maximal exposure of bio-recognition moieties, e.g. antigen-binding sites in antibodies [Trilling et al., 2014], also it is possible to minimize the protein unwanted interaction with the substrate.

6.4.1 Physisorption

Physisorption(physical adsorption) is the simplest strategy for immobilizing proteins on a surface. It involves adsorption of proteins to various surface via weak interactions like electrostatic forces, hydrophobic interactions, van der Waals, and hydrogen bonding interactions, or combination of those.[Israelachvili, 2011] The immobilizing surface is usually dipped in an incubating solution of protein or a continuous flow of the same to achieve a chemistry-less adsorption. Physisorption is weaker, adsorbed layers of proteins are generally less stable as compared to layers formed by covalent or bio-affinity binding. The physisorbed layer of protein is morphological heterogeneous and randomly oriented.

The random orientation of immobilized binding site may lead to inaccessibility of some binding site and conformational changes that can reduce protein activity.[Rusmini et al., 2007] Over-packed surface sites can result in sterically blocked active reaction sites, hence Polyethylene glycol(PEG) has seen wide application has a spacer for reducing steric hindrance. Surfaces functionalized by physisorption have uncoated spaces that may participate in non-specific interactions, blocking of un-coated segments of such a surface is therefore performed with bovine serum albuminBovine Serum Abumin (BSA)

6.4.2 Electrostatic Interaction

Charged functional groups like protonated amine NH_3^+, quaternary ammonium cationsNR_4^+ carboxylic acid $-COO^-$) and sulfonic acid$-RSO_3^-$ are involved in the electrostatic interaction between proteins and surfaces. Electrostatic interactions finds utility in protein immobilization in microfluidic based assays. [Kim and Herr, 2013]

6.4.3 Hydrophobic Interactions

An hydrophobic surface is one that repels water molecules, this ability serves to immobilized protein molecules as water is expelled to allow for the binding of protein terminal group. In recent years microfluidic devices for POC applications are made to be hydrophobic.[Chin et al., 2007] Bhattacharyya and Klapperich introduced a microfluidic chip for a C-reactive protein immunoassay.[Bhattacharyya and Klapperich, 2007]

6.4.4 Physical Entrapment

Physical entrapment is a protein immobilization strategy that involves encapsulating protein in a nano-porous structure. Nano-porous structures of pore sizes of less than a few tens of nanometers are possible[Bhatia et al., 2000], but a compromise in pore size is often required in immunoreactions where large antibodies can be prevented from complexing with corresponding antigens due to slow diffusion through the nano-porous pores. Hydrogels are suitable for generating nanoporous structures and have seen extensive use in bio-analytics.[Zhan et al., 2002]

6.4.5 Covalent Interaction

Covalent Interactions are very well used as immobilization mechanism in microfluidic assays if high and stable protein coverage is desired. The mechanism involves activating an immobilization surface with reactive reagents, bi-functional spacers are then employed to create irreversible bonds with the activated immobilization surface on one end and the amino acid residue on the exterior of the protein at the opposite end. hydroxylamine,[Lee et al., 2012] BSA, or lysin[Yakovleva et al., 2002]

are used to prevent non-specific interactions of un-reacted active functional groups. The inherent chemistry of covalent linkage is complicated[Hermanson, 2008] and covalent bonds can be formed on active reaction sites of proteins thereby reducing activity and increasing incubation time.

A varied and rich assortment of covalent immobilization chemistries are available. Some of the most important chemistries for microfluidic devices are Amine-glutaraldehyde-Amine, Amine-N-hydroxysuccinimide N-Hydroxysuccinimide (NHS), Amine-In-situ generated aldehyde, Carboxylate + NHS + EDC-Amine, Amine/-Sulfhdryl Epoxide, Carboxylate—1-ethyl-3-(3-dimethylamonipropyl) Carbodiimide 1-Ethyl-3-(3-dimethylaminopropyl)carbodiimide (EDC)—amine, and Amine Isothiocyanate [Kim and Herr, 2013].

6.5 TRANSPORT MECHANISMS IN MICROFLUIDIC IMMUNOASSAY

Transport immediately communicates controlled or uncontrolled motion to the mind, In immunoassay microfluidics diffusion and convection are the principal transport Mechanisms.

The transport of analyte in microfluidics is a complex process exhibiting rich and a varied set of behaviours, multiple phenomena interacts and compete for dominance, target molecules convecting along the microfluidic channel diffuse randomly and sometimes downwards to the capture substrate, bound target molecule may dissociate from the immobilization surface back into the convected flow.

The uncertainty in association and dissociation of target molecules during transport process raises questions as to when the effects of the fundamental limits will become limiting. Multiple factors like: number of target molecules that will bind, extracting kinetic parameters from measured binding rates, time of first target molecule binding, designing a system for rapid detection of target molecule needs to be better understood to furnish some semblance of certainty into transport mechanisms and its effect on sensitivity.[Squires et al., 2008] Based on theoretical calculations Sheehan and Whitman[Sheehan and Whitman, 2005] submitted that the diffusive transport of subpicomolar concentration of target molecules solutions to small sensors would require unrealistic long time scales (hours to days).

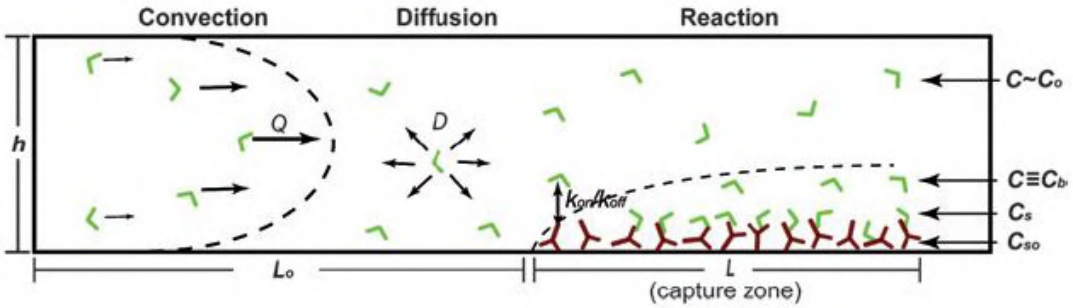

Figure 6.5: Schematic diagram showing analyte convection, diffusion and reaction)[Parsa et al., 2008]

Figure 6.5 shows this convection and diffusion process along a microfluidic channel with the reaction taking place at the capture zone. An area of limited analyte presence called depletion zone forms on the sensing area as analtye captures instantiates [Sethu et al., 2006]. Convection stop the growth of the depletion zone, resulting in a depletion zone of the right length for the delivery of target analyte, in the process diffusive flux balances convection flux. When the depletion zone

becomes smaller than the nominal value, the diffusive flux will dominate the convective flux hence analyte transport will occur in diffusion and be limited by the depletion zone. [Squires et al., 2008]

The Peclet number Pe, mass transport flux and the Damkohler number finds utility in the quantification of microfluidic channel flow performance. [Huang et al., 2013]

Consider a microfluidic channel of width of 2B, length L, mean flow velocity U and a diffusion constant D. When two fluids are brought into contact in this channel, diffusion happens perpendicular to the convecting flow, we can estimate transverse diffusion time over an entire cross-section of species to be $t_D = B^2/D$; in such a flow scenario the diffusion process is one dimensional. A residence time is defined to be the time it takes for a fluid particle to transport from inlet to outlet of microchannel, mathematically given as L/U. Tuning the values of the diffusion and residence time is useful in optimising microfluidic channel for a given performance. For concentration homogenisation in microchannel, the ratio of diffusion time to residence time

$$\frac{BU}{D} \cdot \frac{B}{L} = \frac{PeB}{L} \tag{6.12}$$

must be comparable, this equation implies that the length of a channel required for homogenisation is of order $OPe \cdot B$, hence this ratio will find utility in estimating microfluidic channel length. For application where binding of analyte is primary the diffusion time should be larger than the residence time, it is made possible by introducing flow mixers in the microfluidic channel.

7 MATERIALS AND METHODS

In section Section 1.3, it was mentioned that the goal is to detect the Raman vibrations of the Genetex SARS-CoV-2 antibody, to actualize this some reagents in powdered and liquid forms are required. Some of the needed reagents include Cysteamine-Hydrochloride, dithiobis(succinimidyl propionate) (DSP)(dithiobis(succinimidyl propionate)), Dimethyl sulfoxide (DMSO)(Dimethyl Sulfoxide), Acetone, Isopropranol, Distilled water and Phosphate Buffer Saline (PBS)(Phosphate Buffer Saline). Specific processes needed to attain the stated goal include substrate cleaning, height profilometry, Raman Measurement, Scanning electron microscopy, Sputter deposition of gold, Aliquoting of SARS-CoV-2 antibody, Sonication, Antibody immobilization and O_2 Plasma cleaning.

7.1 RHODAMINE 6G

Rhodamine 6G is a highly fluorescent dye with a large cross-sectional area. Due to its large cross-sectional area Rhodamine dyes fluoresces can be detected easily and inexpensively.[Wikipedia, 2021] Rhodamine 6G in the context of the already stated project goals was employed to characterise the SERS substrates(i.e to determine the electromagnetic enhancement and limit of detection). It also finds other application in fluorescence microscopy, fluorescence correlation spectroscopy, flow cytometry and ELISA. Rhodamine 6G chloride powder as the chemical *Formula* : $C_{28}H_{31}ClN_2O_3$ with chemical strcture shown in Figure 7.1(a)

7.2 AMINOTHIOL LINKER REAGENTS

Aminothiol Linker Reagents contain the -SH group that can bond to gold surface to form the Au-S bond, which in turn allow for bioconjugation of proteins to the gold surface via the sulfhydryl residues in proteins. In the course of experiments Cysteamine Hydrochloride and DSP were used for the aforementioned purpose.

7.2.1 Cysteamine Hydrochloride

Cysteamine Hydrocholride also known as mercaptoethylamine hydrochloride salt that is biosynthesized in mammals. It is synthesized via pantetheine formation by degradation of coenzyme A. Pantetheine is then reduced into cysteamine and pantothenic acid. Cysteamine is a white, water-soluble solid, with molecular *Formula* : C_2H_7NSHCl, and a molar mass of $113.61 g/mol$, with chemical structure shown in Figure 7.1(b), it is best stored desiccated at 4°C. see Section A.1 for more information of Cysteamine Hydrochloride.[goldbio, 2021]

7.2.2 DSP(dithiobis(succinimidyl propionate))

DSP(Lomant's Reagent) is a homo-bifunctional N-hydroxysuccimide ester (NHS ester) crosslinker that is thiol-cleavable, It possess the primary amine-reactive NHS ester on both ends of its 8-carbon spacer arms, NHS ester can reacts with pri-

mary amines to form stable amide bond with the N-terminus of each polypeptide of a given protein(antibody). DSP is non-sulfonated and water insoluble, it is first dissolved in an organic solvent(e.g DMSO), since DSP can be hydrolyzed and in the process loose its crosslinking activity, it is advice to equilibrate the refrigerated vials containing it to room temperature for about 30 to 40 minutes at room temperature conditions. It has a molecular *Formula* : $C_{14}H_{16}N_2O_8S_2$, a molar mass of $404.4g/mol$, and a spacer arm length of $12Å$. Its chemical structure is shown in Figure 7.1(c). it is best stored desiccated at 4°C. see Section A.2 for more information on DSP.[Covachem, 2021] A sulfonated analog of DSP, DTSSP (3,3'-dithiobis(sulfosuccinimidyl propionate)) (DTTSP)(3,3'-dithiobis(sulfosuccinimidyl propionate)) is water soluble.

7.3 SOLVENT

In the course of the experiments three broad classes of solvent by functionality were used namely Organic, buffer and cleaning solvents. The Organic Solvent consisted of DMSO(Dimethyl Sulfoxide) and Dionized water, PBS(Phophate buffer Saline)was the main buffer used for stablizing the antibody, and the cleaning reagents were Acetone and Isopropyl alcoholIso-Propyl Alcohol (IPA), Deionized Water (DI)Dionized water was always handy for cleaning and dissolving different cysteamine hydrochloride solutions.

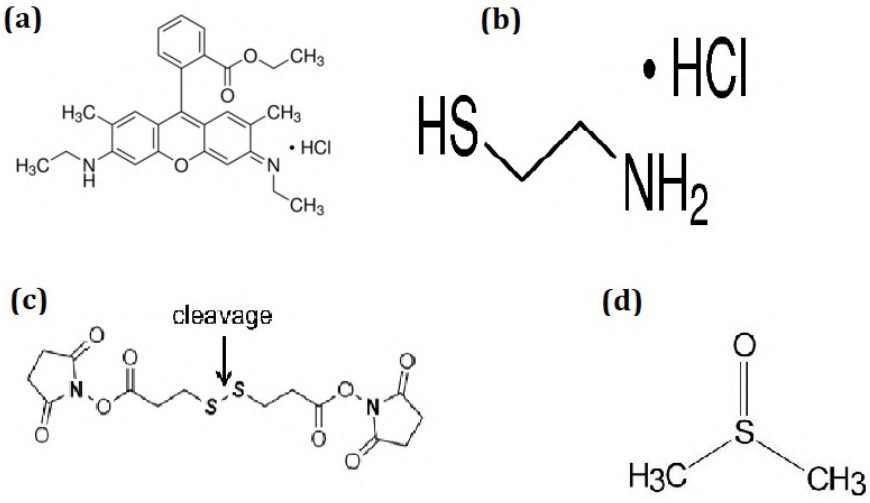

Figure 7.1: Chemical structure of main reagents for antibody immobilization (a)Rhodamine 6G (b) Cysteamine Hydrochloride(c) DSP(dithiobis(succinimidyl propionate)) (d)DMSO(Dimethyl Sulfoxide)

7.3.1 DMSO(Dimethyl Sulfoxide)

DMSO is an aprotic(No hyrogen or proton) polar solvent that has no O-H or N-H bonds. Its aprotic nature confer upon it lesser toxicity than other members of its class like dimethylformamide, dimethylacetamide, N-methyl-2-pyrrolidone, and Hexamethyl-Phosphoramide (HMPA)Hexamethyl-phosphoramide [mpbio, 2021]. DMSO is finds ready application as a solvent for chemical reactions involving salts and nucleophilic substitutions. DMSO is miscible with water (1ml DMSO + 1ml H_2O), and very hygroscopic liquid, it should be protected from exposure to moist environment.

It has a molecular *Formula* : $(CH_3)_2SO$, and a molar mass of $78.132g/mol$. Its chemical structure is shown in Figure 7.1(d) it maintains stable from 25°C to 100°C. see Section A.3 for more information.

7.3.2 Deionized Water

Deionization is a chemical process that entails involves using ion-exchange resins to exchange hydrogen and hydroxide ions for dissolved minerals(iron, copper, chloride and sulphate) and then recombine to form water. It should be noted that uncharged organic molecules, viruses, or bacteria are not reoved by deionization, except by incidental trapping in the proprietary resin. Deionization is effected continuously and cost-efectively by electrodeionization.[wikipedia, 2021d]

7.3.3 PBS(Phosphate Buffer Saline)

Phosphate-buffered saline (PBS) is an isotonic water-based salt solution that finds application in maintaining a constant pH of (7.2-7.5) in many biological research applications. [wikipedia, 2020b] In the course of the experiments to be described in later chapters, one tablet of PBS tablet from Sigma-Adlrich was dissolved in 200ml of DI water to produce a buffer solution with a pH range of about 7.2-7.6, 5μ liters of Gentex SARS-CoV-2 antibody was pH stabilized in this PBS solution for longer storage at -20°C.

7.3.4 Acetone

Acetone is a colourless, volatile and highly flammable organic compound with the molecular *Formula* : $(CH_3)_2CO$. Low-grade acetone finds utility in academic laboratory as a glasswares/substrate rinsing agent, it removes residues and solids before a final wash. Care must be taken with Acetone, as dried residues of it are harmful to substrates and glasswares.[wikipedia, 2021a]

7.3.5 Isopropyl Alcohol

Isopropyl alcohol is a colorless an flammable chemical compound with chemical *Formula* : $(CH_3)CHOHCH_3$, just like acetone it a strong odour. [wikipedia, 2021c] It is used in tandem with Acetone for cleaning substrates and glassware in the laboratory.

7.4 GENETEX SARS-COV-2 ANTIBODY

In other to obtain the Raman spectrum for a SARS-CoV-2 antibody, Genetex SARS-CoV-2 Antibody was purchased and stored at -20°C. for more information see appendix Section A.4.

7.5 GLASSWARES

Ultra-violet tight glasswares were used to store Antibody solution to prevent light mediated protein denaturation, other glasswares and plastic wares used in the course of experiments include plastic 2ml conical tubes, petri-dishes, borosilicate glass slides, and beakers. Tweezers were employed to carry and hold the substrates for varying processes, an eppendorf pipette was used to measure very small and ac-

curate volumes of reagents. see Figure 7.2 for a pictorial representation of glassware used.

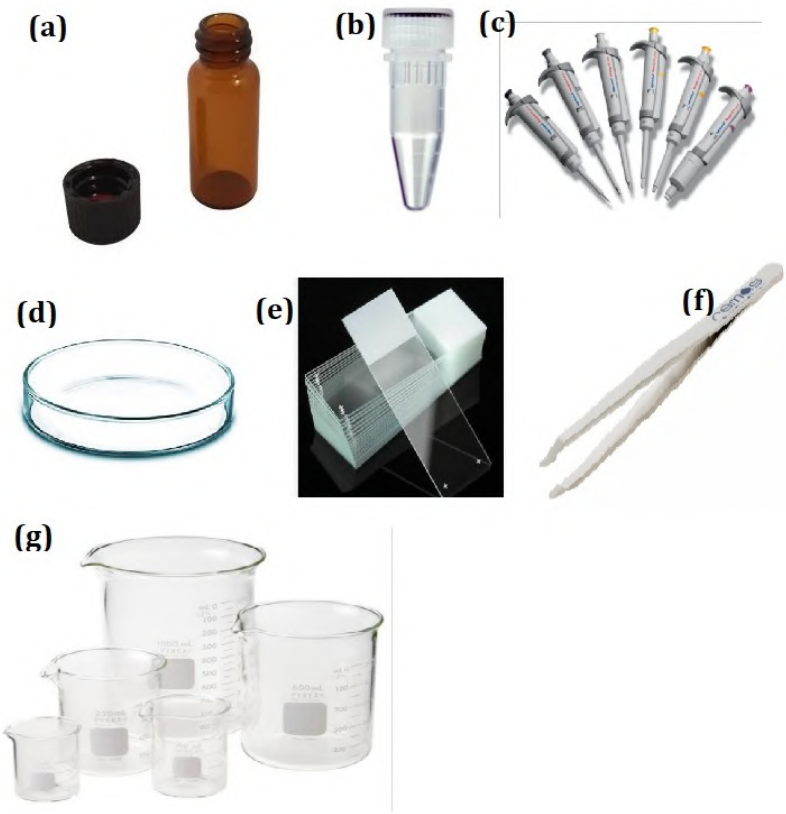

Figure 7.2: (a)Ultra Violet tight Vials, (b) Plastic Conical Vials,(c) Eppendorf Pipette of various size range,(d)Petridish,(e)Borosilicate Glass Slides,(f)Tweezers,(g)Beakers of Various size,

7.6 CLEANING PROCESS

In other to effect cleaning, Piranhia, Acetone, IPA and DI water were used in addition to sonication and O_2 plasma. The cleaning action is described below.

PIRANHIA: Piranha solution is a 3:1 mixture of sulfuric acid and 30% hydrogen peroxide. It is a solutions used to remove organic residues from substrates in chemical labs. In my case both sulfuric acid and hydrogen peroxide were mixed before application on to substrates and glassware's. [Princeton, 2021]

Piranha solution is exothermic and may result in explosion and thermal burns, hence pyrex glass was used as a mixing container. The preparation and mixing of the piranha solution was done in a cleaning hood, utilizing the hood as a safe barrier between me and the piranha solution. Acid resistant lab coat, gloves and face covering were also worn. Hydrogen peroxide was added slowly to sulfuric acid while gently stirring.

All rinsed and dried containers and substrates were placed slowly into piranha baths. After the cleaning step the used piranha was diluted by first adding it to water and then neutralizing the diluted solution with sodium hydroxide inside the fume hood while stirring. When the solution was within a pH range of 4-10, the solution was disposed of via a drain.

SONICATION: Sonication involves the application of sound energy to agitate particles on a substrate or surface. In the context of our use, ultrasonic frequencies (>20 kHz) where used to generate full and half wave vibrations for knocking organic residues from substrates.

BASIC CLEANING STEP: The basic cleaning step involves dipping the substrate into acetone, IPA and DI water sequentially and sonicating in each solvent for at least 10minutes.

AIR GUN BLOW DRYING: The Air Gun blow drying served to dried substrates and other glasswares after other process of cleaning. The air gun features nozzle operated by spring loaded lever and a hose connecting the nozzle to the air supply, when the lever is compressed air flows out with high velocity and impenge on the substrate, thereby blowing off and evaporating any liquid on the substrate.

O_2 PLASMA: Plasma cleaning entails the removal of organic residues and other impurities from substrates and surfaces through the use of high velocity plasma. Argon and oxygen are the gases of choice. [Garcia-Vaquero et al., 2017] The plasma consist of gas atoms that are excited to a high energy state, on returning to a lower state they release a photon of light that is observed as a characteristics "light blueish glow" in the case of oxygen gas. Oxygen air plasma is used in the research because it is economical and environmentally friendly.

SPUTTER DEPOSITION: High-purity source material is subjected to a energetic gas plasma (usually argon). The high velocity plasma knocks off source atoms that transverses a vacuum to condense as thin films on the substrate. This process was used in depositing gold layers on thin glass slide.[Basile, 2013]

7.7 SURFACE CHARACTERISATION METHODS

SCANNING ELECTRON MICROSCOPY: In a scanning electron microscope Scanning Electron Microscope (SEM) electrons are directed and scanned over a surface placed in a vacuum, this results in an interaction of the electron beam with the sample surface, various signals produced in the process can be processed to obtain sample topography and compositional information. The SEM was used to observed the surface topography of nanoporous gold.[Carleton, 2021]

ALIQUOTING: The process of Aliquoting involves using the eppendorf pipette to remove from stock sample a given volume of reagent and transfering it to substrate, conical vial for immediate or further use.

HEIGHT PROFILOMETRY: To make height measurements on the substrate, the substrate was placed on a linear positioner that moves in the z-axis, this linear positioner is one arm of the michelson interferometer. A collimated light source illuminate the whole substrate, light from the reference mirror and the object plane interferes into a pattern that is process via the CCD and inbuilt algorithm to obtain the topographic information. The experimental setup is shown in Figure 5.4.

RAMAN MEASUREMENT: Raman Measurements was done by placed the sample to be analyzed on sample stage of the Raman Spectrometer and then focusing a 50X objective on the substrate. The graphic user interface of the operational software of the Raman spectrometer allows for several controls to the stage, laser illumination, acquisition parameters that helps to improve the quality of obtained spectral.

7.8 SERS SUBSTRATES

Several SERS Substrates were employed in the following research study, they include Nanoporous goldNanopporous Gold (NPG), Gold coated cover glassGold Coated Cover Glass (GCCG), Gold Nanoparticles Deposited on topaz and on glass.

NANOPOROUS GOLD: NPGs were received in two boxes from a research group in torino Italy, one box contained clean samples (NPG clean), the other samples that were already functionalised were subsequently cleaned. The NPG samples were prepared by arc melting master alloy ingot of composition $Au_{20}Si_{2}OCu_{48}Ag_{7}Pd_{5}$ (at.%) with pure elements (Au: 99.99%, Si: 99.9995%, Ag, Cu, Pd: 99.99%) in inert Argon atmosphere. The melted master alloy ingot was quickly quenched and subsequently spurned on a rotating copper wheel[Scaglione et al., 2019].

GOLD COATED COVER GLASS(GCCG): This SERS substrate was made by the sputter deposition technique discussed in Section 7.6, cleaned glass was placed on glass holder of the sputter deposition machine, which is underneath the gold target, a glass cover was used to seal up the circumference of the sputtering environment and finally the gold target locked in place, the machine was subsequently evacuated to create a vacuum for an undisturbed condensation of knocked off gold from the surface of the target to the surface of glass. The conditions for gold depositions were 40mA of current, the cleaned glass was at a distance of 25mm from the gold target, vacuum pressure was 0.5mbar, deposition time was 60s and a deposition rate of 1.8nm /sec was used. Two deposition passes was done on each cleaned substrate with each pass depositing 108nm layer of gold and a total of 216nm layer of gold.

GOLD NANOPARTICLES DEPOSITED ON TOPAZ: Gold nanoparticles deposited on topaz was supplied to me by Saleh Aghajani a PHD student in the Micro and nano system engineering group. They were made by aerosol direct writing of gold nanoparticles via a nozzle to the surface of cleaned topaz in a vacuum environment. A (VSParticle G1) particle generator and a deposition unit were employed for the writing process. The particle generator uses the spark ablation method for the writing process.

8 EXPERIMENTS AND RESULTS

To the very end of achieving the already stated project goal of measuring the Raman spectrum of the Genetex SARS-CoV-2 antibody, several experiments were performed and promising results obtained. This chapter consist of a thematic presentation of these results, the experiments are broadly grouped into three, those meant for surface characterisation(e.g SEM, White intereferometry, and SERS enhancement with rhodamine 6G), Antibody immobilization(using DSP and Cysteamine Hydrochloride) and the Raman Measurement of the immobilized Antibody.

8.1 SURFACE CHARACTERISATION OF SERS SUBSTRATE WITH RHODAMINE 6G

NANOPOROUS GOLD: Nanoporous gold as the name suggest possesses a high surface area some 2–1000 times larger than a similarly SERS substrate of another fabrication type and form factor. It is a very conductive material and in recent years have received considerable attention. In order to investigate and confirm the random pore morphology of its surface area, an SEM was used to probe its surface area, the NPG sample was place on a sample stage covered with carbon black(a conductor that prevents the charging of samples in the SEM). Figure 8.1a to Figure 8.1c shows the obtained images at 12000X, 27000X and 35000X magnification respectively, while Figure **??** shows the image of the same under a Keyence Digital Microscope(VHX-7000 series).

The Three SEM images were obtained at an accelerating voltage of 20KV and at a sample working distance of 11mm to the electron gun. The spot sizes for Figure 8.1a(a) is 18nm, it is 20nm for Figure 8.1a(b) and 30nm for Figure 8.1a(c). The morphology of the nanoporous gold shows that well oriented and random pore sections exist on its surface.

For the characterisation of the various SERS Substrate already mentioned in Section 7.8, several dilute concentration of Rhodamine 6G was made from stock solution of $1mM$ Rhodamine 6G. The dilution process of any reagent is governed by the formula $M_1V_1 = M_2V_2$. where M_1 is the molarity(amount of substance per liter of solution) of the stock solution, M_2 is the molarity of the final dilute solution, V_1 is the pipetted volume of the stock solution and M_2 is the final volume of the solution with the stock solution volume inclusive. Two independent dilution steps were implemented as shown in table Table 8.1, to a 250ml volume of deionized water a 5ml and 2.5ml volume of stock rhodamine 6G reagent was diluted to 20 and 10 μM respectively. The diluted solutions were stored at -4°C.

RHODAMINE 6G ON NANOPOROUS GOLD After the dilution process above, glass slides were cleaned by sonication in acetone, IPA and DI water for 15minutes each. The cleaned slides were then blow dried with an air gun. Both cleaned and uncleaned NPG were placed gently on the cleaned glass slides with a tweezer. $10\mu l$ of diluted stock solution was then pipetted unto the nanoporous gold on each glass slide and allowed to incubate for 5 hours on each occassion. Raman measurement was done on a HORIBA Jobin Yvon LabRAM equipped with an argon ion laser operating at 514 and 633 nm, a CCD camera, an objective 50× (NA = 0.5).

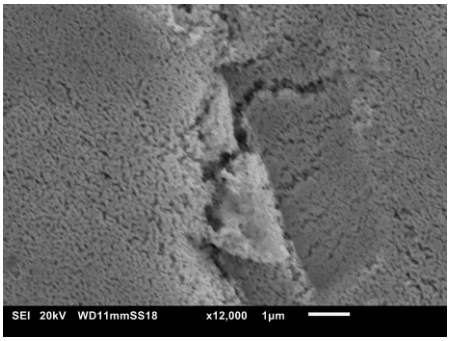

(a) A SEM image of the Nanoporous gold surface at 12000X.

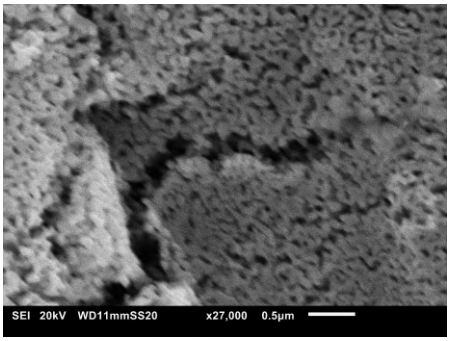

(b) A SEM image of the Nanoporous gold surface at 27000X.

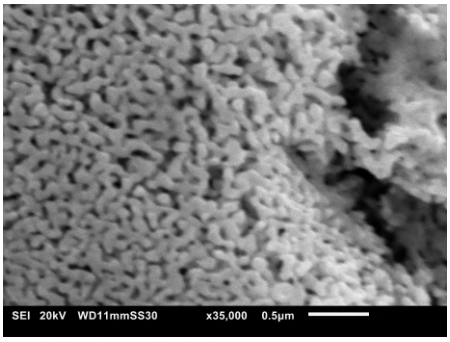

(c) A SEM image of the Nanoporous gold surface at 35000X.

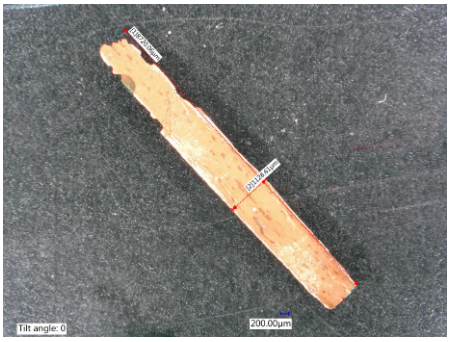

(d) A 3D microscope image of a Nanoporous gold.

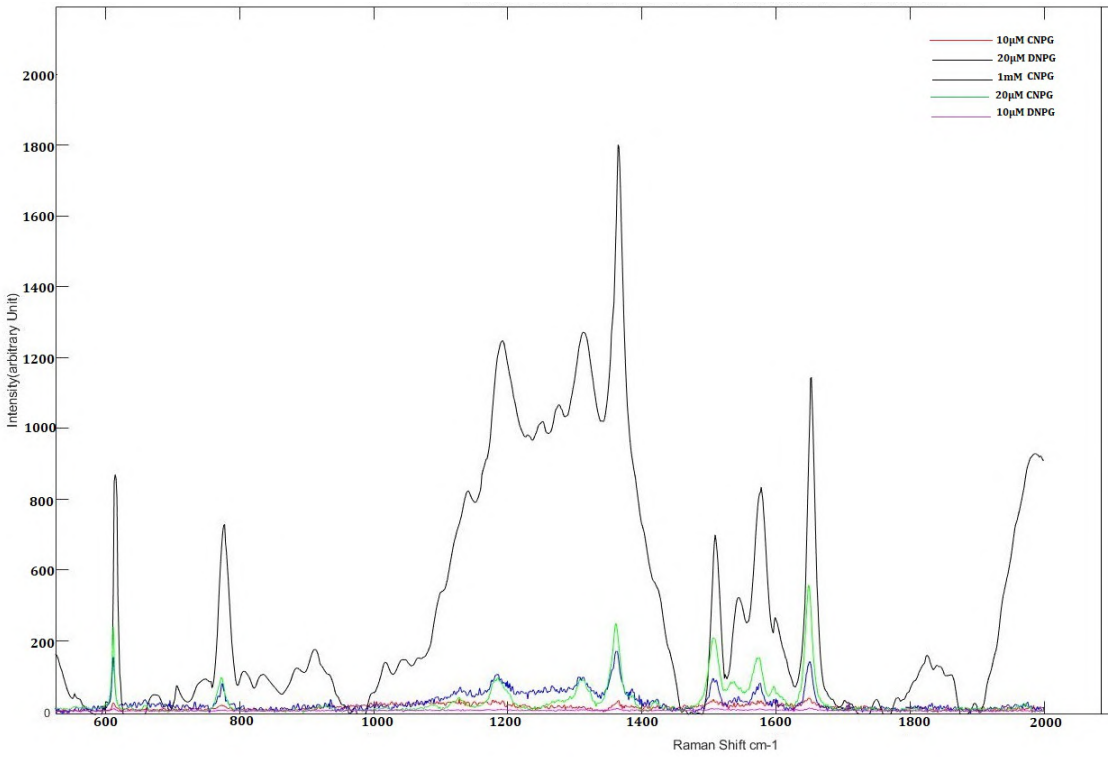

Figure 8.2: Raman Spectrum of different concentration of Rhodamine 6G on Nanoporous gold.

All SERS spectra were obtained at a laser power of $20\mu W$, with an acquisition time of 30s and 2 accumulations. The spectra were collected over the range of $500 2000 cm^{-1}$ with a spectral resolution of $\approx 0.3 cm^{-1}$.

STEPS	M_1	V_1	M_2	V_2
Step 1	1mM	5ml	$20\mu M$	250ml
step 2	1mM	2.5ml	$10\mu M$	250ml

Table 8.1: Dilution Table for Rhoadmine 6G

Band Frequency (Reference)	**Vibration modes**	**Peaks 1mM**	**Peaks 20μM**	**Peaks 10μM**
611([Aghajani et al., 2020])	C–C–C ring in-plane bending	615	611	611
659 [Aghajani et al., 2020]	Probably for xanthene ring puckering	660	–	
773([Aghajani et al., 2020])	C–H out-of-plane bending	777	774	772
1088 ([Zhong et al., 2018])	–	–	1083	–
1127([Aghajani et al., 2020])	C–H in-plane bending	1139	1126	1127
1183([Zhong et al., 2018])	CC bridge band stretching and C–H bend	1193	1185	–
1276 ([Aghajani et al., 2020])	C–O–C stretching	1275	1285	–
1310([Zhong et al., 2018])	Aromatic C–C stretching	1311	1308	–
1360 [Zhong et al., 2018]	Aromatic CC bending	1364	1360	1365
1420([Zhong et al., 2018])	CN stretching in NHC_2H_5	–	–	–
1507([Aghajani et al., 2020])	Aromatic C–C stretching	1509	1507	1508
1573 ([Aghajani et al., 2020])	Aromatic C–C stretching	1573	1574	–
1595([Zhong et al., 2018])	hybrid mode (phenyl ring with $COOC_2H_5$)	1598	1596	1597
1648([Zhong et al., 2018])	Aromatic C–C stretching	1651	1648	1648

Table 8.2: Raman Band Frequencies of Rhodamine 6G applied in concentration steps of 1mM 20 and $10\mu M$ on **CNPG** with a cleaning step after each Raman measurement

The spectral data were recorded by using LabSpec6 software, and baseline correction was done to remove the fluorescent background. see Section B.1 for more details about Raman acquisition conditions and parameters. Before the initial incubation process the cleaned bare NPG substrate was probed with the Raman spectrometer so as to observe and obtain the default surface photoluminiscence. Figure B.4 hold more information about this. After each measurement step the NPGs were cleaned in Acetone, IPA and DI water without sonication, *sonication breaks NPG into unuseable particles*.

The Raman spectrals shown in Figure 8.2 are the average of 4 measurements on different spots on the nanoporous gold, this was done to access the level of reproducibility of the SERS substrates.

It is observed that on a peak for peak basis, and at each concentration the spectral intensity for the clean nanoporous gold Clean Nanoporous Gold (CNPG) is slightly higher than that of the dirty nanoporous gold Dirty Nanoporous Gold (DNPG). This is attributed to the fact that the pore spaces of the DNPG are clogged with organic residues, thereby limiting electromagnetic enhancement possible. Table 8.2 and Table 8.3 shows the characteristic spectral peaks and this agrees with those found in literature. The information contained in tables suggest that for DNPG and CNPG with decreasing concentration, some of the characteristic peaks that are present at a higher concentration of rhodamine 6G are no longer visible in the new spectrum of a lower concentration, for the CNPG at 20μM of rhodamine 6G the number of peaks found and their position with respect those found with 1mM concentration of rhodamine 6G is very similar and correlates well with literature, with a decrease in concentration to 10μM a good number of peaks becomes absent, however the

Band Frequency	Vibration modes	Peaks 10μM	Peaks 10μM
611	C–C–C ring in-plane bending	611	611
659	Probably for xanthene ring puckering	658	-
773	C–H out-of-plane bending	773	771
1088		1076	-
1127	C–H in-plane bending	1128	-
1183	CC bridge band stretching and C–H bend	1184	1176
1276	C–O–C stretching	1265	-
1310	Aromatic C–C stretching	1312	-
1360	Aromatic CC bending	1363	1363
1420		1420	-
1507	Aromatic C–C stretching	1506	1514
1573	Aromatic C–C stretching	1577	1575
1595		1597	-
1648	Aromatic C–C stretching	1651	1651

Table 8.3: Raman Band Frequencies of Rhodamine 6G applied in concentration steps of 1mM 20 and 10μM on **DNPG** with a cleaning step after each Raman measurement

peaks present(i.e 611, 1127, 1508, 1648cmcm^{-1}) helped to characterise the presence of the aromatic dye.

The information in Table 8.3, as collated from the Raman spectrum of DNPG, maintains the same character as of a decrease in recognition capacity of the SERS substrate with continued use. In general, band frequencies varies by 4 to 10cm^{-1} due to the different conformational state of the rhodamine 6G dye on the surface of the nanoporous gold.

GOLD COATED COVER GLASS(GCCG) IN RHODAMINE 6G The Gold coated cover glass(GCCG) substrate were were adequately cleaned and sonicated as already mentioned, Before the initial incubation process the cleaned bare GCCG substrate was probed with the Raman spectrometer so as to observe and obtain the default surface photoluminiscence. Figure B.4 hold more information about this. Rhodamine 6G was drop coated on the surface of the substrate and allowed to incubate for at least 6 hours and Raman measurements were performed. Raman measurement conditions are same with those of the nanoporous gold.

The Raman spectrals obtained are an average of four measurements on different spots on the GCCG SERS substrate Figure 8.3 shows the obtained spectrum, peaks were finely defined across the concentration spread, Table 8.5 shows the Raman peaks obtained at the different concentrations, this information suggests that with decrease in concentration from 1mM to 10μM, almost characterising peaks are present however of lower intensity. The variation of peak location is relatively smaller(about 2 to 3cm^{-1}) when compared to Band frequencies in literature. The inter-concentration band frequencies differences is also of the same range.

GOLD NANO-PARTICLES ON TOPAZ Gold nanoparticles were deposited on three topaz substrate by aerosol direct writing as described in Section 7.8. All three fabricated SERS substrate were adequately cleaned and sonicated as already mentioned, before the initial incubation process the cleaned bare topaz substrates were probed with the Raman spectrometer so as to observe and obtain the default surface photoluminiscence. Figure B.4 contains more information about this. Rhodamine 6G

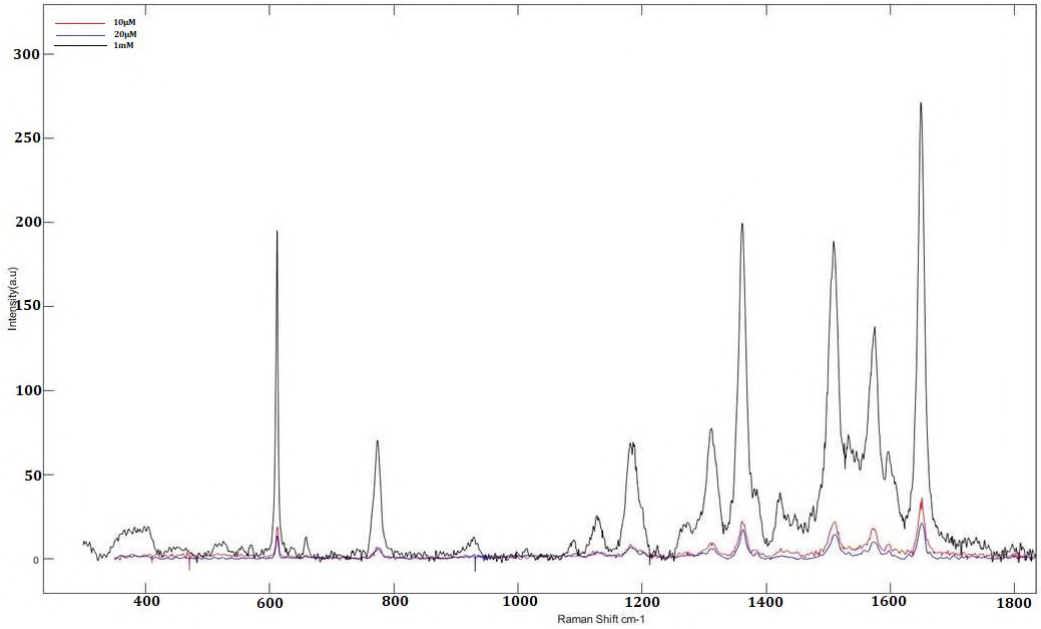

Figure 8.3: Raman Spectrum of different concentration of Rhodamine 6G on Gold coated cover glass applied in concentration steps of 1mM, 20μM and 10μM on **GCCG** with a cleaning step after each Raman measurement.

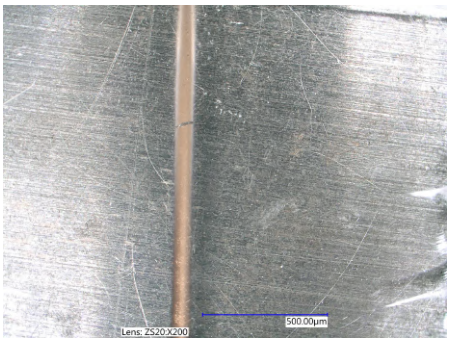

(a) A 3D microscope image of TopazA.

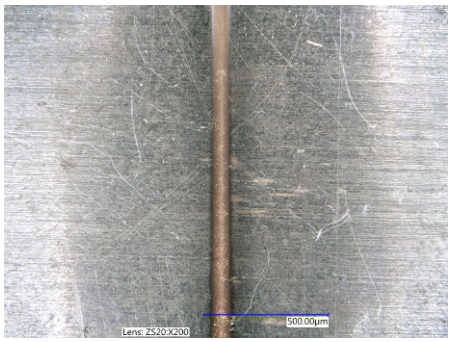

(b) A 3D microscope image of TopazB.

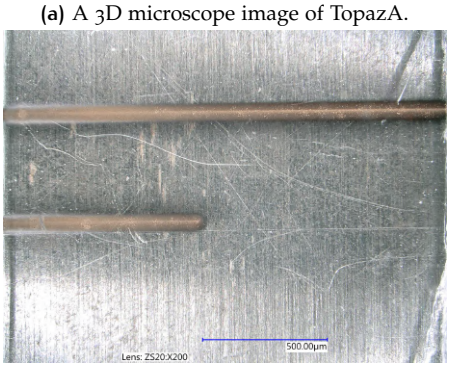

(c) A 3D microscope image of TopazC.

Figure 8.4: 3D Microscope image of three Topaz Substrate

solution of concentration 10μM was then drop coated on the surface of the substrates and allowed to incubate for at least 6 hours and Raman measurements were performed. The measurement conditions are the same as those of the nanoporous gold and GCCG.

Figure 8.4a to Figure 8.4c shows a 3D microscope image of three topaz substrates, the bounding long edges of each image appears black, this is a result of deposition of gold nanoparticles of size less than or equal to 20nm, gold nanoparticles of such

Band Frequency	Vibration modes	Peaks 1mM	Peaks 20μM	Peaks 10μM
611	C–C–C ring in-plane bending	612	612	611
659	Probably for xanthene ring puckering	658	657	–
773	C–H out-of-plane bending	773	771	774
928	-	928	-	-
1012	-	1012	-	-
1088 –	–	1090	–	1094
1127	C–H in-plane bending	1126	1120	-
1183	CC bridge band stretching and C–H bend	1185	1180	1180
1276	C–O–C stretching	1275	1285	1286
1310	Aromatic C–C stretching	1312	1313	1316
1360	Aromatic CC bending	1360	1361	1361
1420	–	1421	1422	1425
1507	Aromatic C–C stretching	1508	1511	1509
1573	Aromatic C–C stretching	1573	1574	1574
1595		1598	1599	1597
1648	Aromatic C–C stretching	1648	1648	1649

Table 8.4: Raman Band Frequencies of Rhodamine 6G applied in concentration steps of 1mM 20 and 10μM on **GCCG** with a cleaning step after each Raman measurement

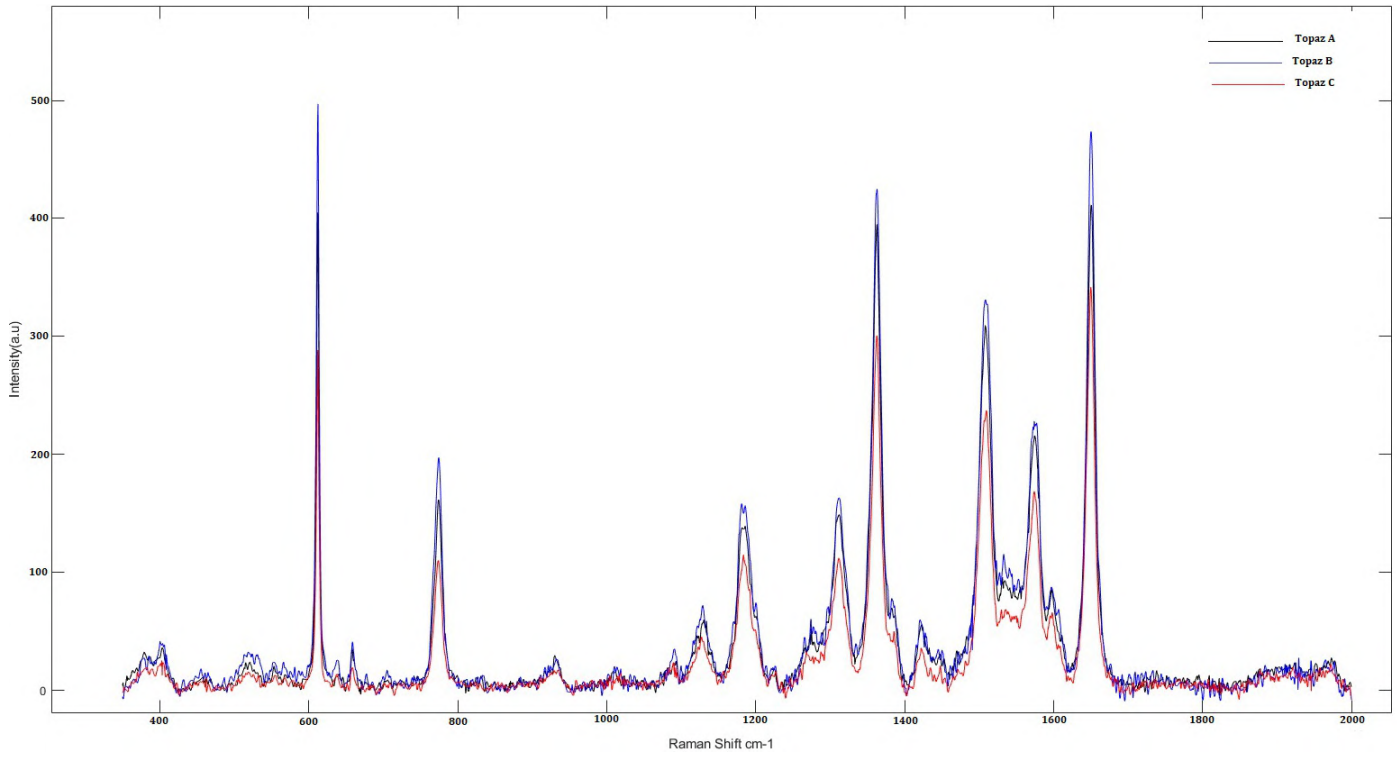

Figure 8.5: Raman Spectrum of 10μM of Rhodamine 6G physisorbed on three gold deposited Topaz substrates.

sizes mainly absorbs light with no scattering, however, in-between the bounding long edges, there is a lengthwise central region that is reflective and yellowish to

Band Frequency	Vibration modes	Topaz A	Topaz B	Topaz C
611	C–C–C ring in-plane bending	611	612	611
659	Probably for xanthene ring puckering	657	659	657
773	C–H out-of-plane bending	773	775	773
928	-	929	933	933
1088 –	–	1–	1089	1088
1127	C–H in-plane bending	1131	1127	1128
1183	CC bridge band stretching and C–H bend	1183	1185	1183
1276	C–O–C stretching	1275	1285	1286
1310	Aromatic C–C stretching	1310	1310	1310
1360	Aromatic CC bending	1363	1360	1363
1420	–	1421	1420	1423
1507	Aromatic C–C stretching	1509	1509	1508
1573	Aromatic C–C stretching	1574	1573	1573
1595		1596	1597	1598
1648	Aromatic C–C stretching	1649	1649	1649

Table 8.5: Raman Band Frequencies of 10μM Rhodamine 6G on three topaz substrates

the eyes, this section consist of gold nanoparticles of diameter 45nm and above, they do much of the light scattering.

Figure 8.5 shows the obtained spectrals for three topaz substrates(A,B, and C). These Raman spectrums are an average of four measurements on different spots on the chemisorbed Rhodamine 6G on each topaz SERS substrate. peaks were finely defined in all three spectrals, hence a good reproducibility, topaz substrate B was most sensitive, followed by substrates A and B.

Table 8.5 shows the Raman peaks obtained for the three topaz substrates at a concentration of 10μM, this information proves the presence of majority of the characterising peaks. Variation of peak wavenumber locations on each substrate is relatively small(about 1 to $2cm^{-}1$).

8.2 ELECTROMAGNETIC ENHANCEMENT FACTORS

In order to quantify the extent of amplification of the initial weak Raman scatter, the enhancement factor for each substrate is calculated from Equation 8.1

$$EF = \frac{I_{SERS}}{I_o} * \frac{C_o}{C_{SERS}} \tag{8.1}$$

where EF is Enhancement Factor, I_{SERS} represents Raman Intensity of a given peak from a SERS measurement, I_o the Raman Intensity of a given peak from a blank substrate, C_o concentration of molecule on blank substrate and C_{SERS} concentration of molecule on SERS substrate. Rhodamine 6G was drop on the blank surface of cover glass and topaz to obtain the I_o values. See Table 8.6 for details.

Parameters	CNPG	DNPG	Topaz A	Topaz B	Topaz C	GCCG
I_{SERS}	1000	375	422	472	335	275
I_o	10	5	10	14	9	10
C_o	1mM	1mM	1mM	1mM	1mM	1mM
C_{SERS}	10	$20\mu M$	$10\mu M$	$10\mu M$	$10\mu M$	10μM
EF	$1 * 10^4$	$3.75 * 10^3$	$4.22 * 10^3$	$3.371 * 10^3$	$3.722 * 10^3$	$2.75 * 10^4$

Table 8.6: A table of parameter values for calculating Enhancement Factors

8.3 SURFACE CHARACTERISATION OF SERS SUBSTRATE WITH WHITE LIGHT INTERFEROMETRY

White light interferometric measurements were performed according to the process described in Section 7.7. Measurement specifics and parameters are discussed in Section B.2. Roughness parameters are generally represented by letter R followed with a subscript. Rz is the sum of the maximum peak height calculated by averaging maximum peak to valley of five consecutive sampling lengths within a measuring length, Rpm is the average maximum peak height and Rvm the average maximum valley height, both Rpm and Rvm are calculated by summing the highest peaks and lowest valleys respectively in a measurement window.[Bhushan et al., 1995] Sa represents the arithmetic mean height while Sp is the maximum peak height, Sdq and Str stands for the root mean square gradient and texture aspect ratio respectively of the surface.[Bhushan et al., 1995]

From the roughness data obtained, 4 different sets of quantitative roughness measures were computed namely, Rz analysis, height, hybrid and spatial parameters. The parameters in color green as shown in Table 8.7, Table 8.8, Table 8.9 and Table 8.10 have been briefly described in Table 5.1.

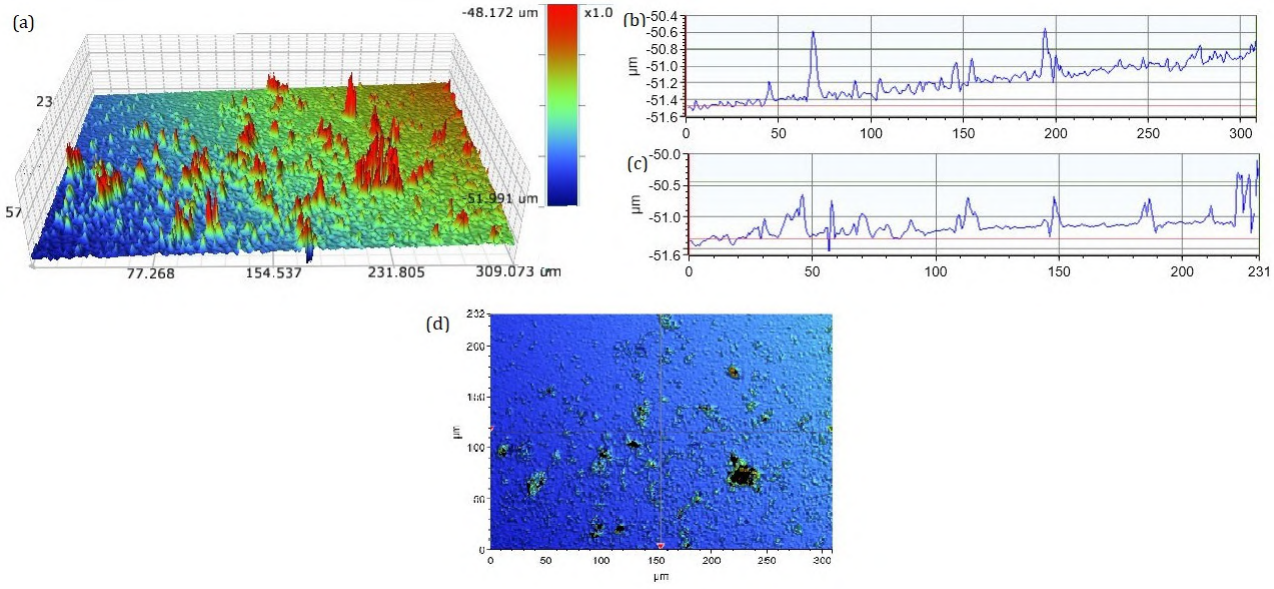

Figure 8.6: (a) Surface topography of GCCG (b)X-axis cross-section through red reference point on surface topography (c)Y-axis cross-section through red reference point on surface topography (d) Plan view of GCCG surface topography

GOLD COATED COVER GLASS In Figure 8.6 surface topographic information are presented, Figure 8.6(a) shows the roughness spread across a measurement window

of 309μm by 231μm, The surface topography shows an inherently rough profile of the gold coated cover glass sample, plateaus are green and yellow in colour, valleys are blue and red colour indicates peaks/summits (this colour grading holds true for all surface topography presented in this section. The GCCG shows an Rpm of 48.716μm and an Rvm of -51.932μm, the average depth of valleys is more than that of the average the peak heights, meaning the depths of the observed valleys will play quite a slightly more significant role in electromagnetic enhancement than the peaks as light radiation will interact with localized trapped surface electrons in this valleys leading to higher SERS activities this areas, the plateau region is the most extensive in size in the topography, the spatial dominance of the plateau region can be seen to result from the uniform deposition of the sputtering process. Analytes chemisorbing or physisorbing in plateuas may witness somewhat mid-range electromagnetic enhancement. Figure 8.6(b), (c) shows an X and Y-axis height cross-section of the surface topography through the reference point marked red in Figure 8.6(d). These cross-section shows maximum peak height of 0.9μm. The Sdq value of 9.265°shows that is some tilt in the SERS surface, an Str value of 0.856 indicates a spatially isotropic surface texture, hence peaks and heights then to be uniformly repeating.

Rz Analysis		**Height Parameters**		**Hybrid Parameters**		**Spatial Parameter**	
Rpm	48.716μm	Sa	82.64nm	Sdq	9.265°	Str	0.856
Rvm	-51.9324μm	Sp	2.884μm				
Rz	3.216μm	Sq	0.163μm				

Table 8.7: Height Profilometry Measurement for Gold Covered cover glass GCCG.

GOLD NANO-PARTICLES ON TOPAZ In Table 8.8 surface topographic information are presented while Figure 8.7(a) shows the roughness spread across a measurement window of 309μm by 231μm. The surface topography shows a more even spread of peaks, plateaus and valleys, there is however a noticeable span of plateaus across the measurement window and on approach to any peak. For topaz A substrate an Rpm of 3.749μm and an Rvm of -0.981μm is observed, this value is well below that for the GCCG substrate, this is as a result of the fabrication of the SERS surface of the topaz substrate, in all topaz substrate gold nanoparticles of average size 20nm are deposited on cleaned topaz substrate, resulting in the somewhat even spread of surface features, the areas with more peaks were directly under the deposition nozzle for a longer time. Sq(Root mean square value of peak height in the area of the measurement, it is an area roughness measure) under the height parameter column has a value 0.229μm.

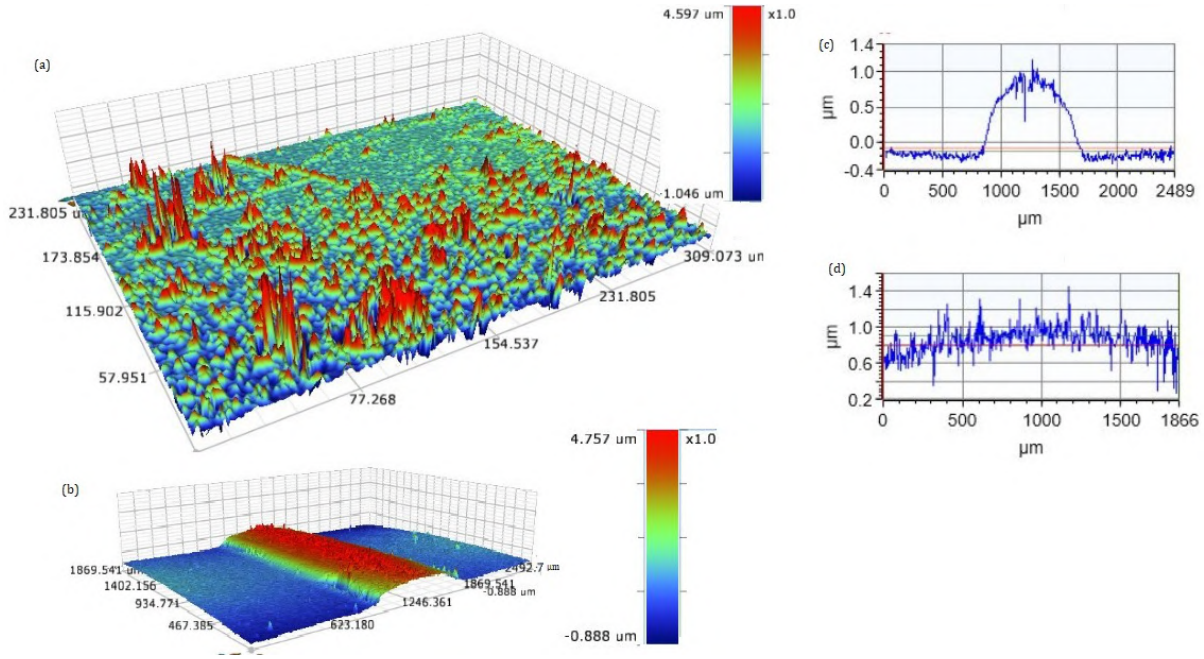

Figure 8.7: (a)Roughness Topography of Topaz A substrate (b) Surface topography of SERS region and adjacent topaz material (c)X-axis cross-section through red reference point on surface topography (d)Y-axis cross-section through red reference point on surface topography

Figure 8.7(b) shows the 1μm elevation of the SERS surface above the topaz substrate, this height is found to be sufficient for electromagnetic enhancement. Figure 8.7(c) and (d) shows an X and Y-axis height cross-section of the SERS surface elevation through the midpoint of the sampling window.

The measurement window for Topaz B substrates is 2489μm by 1866μm, while that of Topaz C is 309μm by 231μm. Topaz A substrate. When compared to all other SERS substrates topaz B substrate in Figure 8.8(a) shows the most even and ubiquitous spread of peaks and plateaus, with the presence of very few localized surface irregularities, these surface irregularities may come from fabrication or handling. Both topaz B and C shows SERS surface elevation of 1μm, which is same with GCCG and topaz A substrate.

The Rpm value of topaz B and C are both 37.% and 79.381% respectively higher than that of topaz A substrate, the Rvm values of B and C are also 9.17% and 4.17% higher than topaz A substrate, this implies that a more even distribution of peaks is suitable for getting a higher average maximum roughness value. The area roughness measure Sq for topaz A, B and C are 0.229μm, 0.235μm and 0.285μm respectively, it is inferred from this values that a region with an even spatial distribution of surface features of peaks, plateaus and valleys is more desirable for a SERS surface as the Sq value is a higher. The Sdq values for the SERS surface on topaz A, B and C are respectively 11.896, 13.327, and 12.016°, this shows that is some tilt in the SERS surface.

Rz Analysis		**Height Parameters**		**Hybrid Parameters**		**Spatial Parameter**	
Rpm	3.749μm	Sa	0.133nm	Sdq	11.896°	Str	7.314
Rvm	-0.981μm	Sp	4.598μm				
Rz	4.73μm	Sq	0.229μm				

Table 8.8: Height Profilometry Measurement for Topaz A substrate.

Rz Analysis		Height Parameters		Hybrid Parameters		Spatial Parameter	
Rpm	5.146μm	Sa	0.141nm	Sdq	13.327°	Str	0.78
Rvm	-1.071μm	Sp	7.383μm				
Rz	6.216μm	Sq	0.235μm				

Table 8.9: Height Profilometry Measurement for Topaz B substrate.

In Figure 8.9(b) the curviness of the surface topography of the topaz area adjacent to the SERS elevation emanates from the cleaned topaz surface profile before fabrication, clean and undeformed substrate can be used to prevent this. The curviness artefact does not have any functional value. Other functional, height, hybrid, and spatial parameters not discussed here will be highlighted under the chapter on discussions.

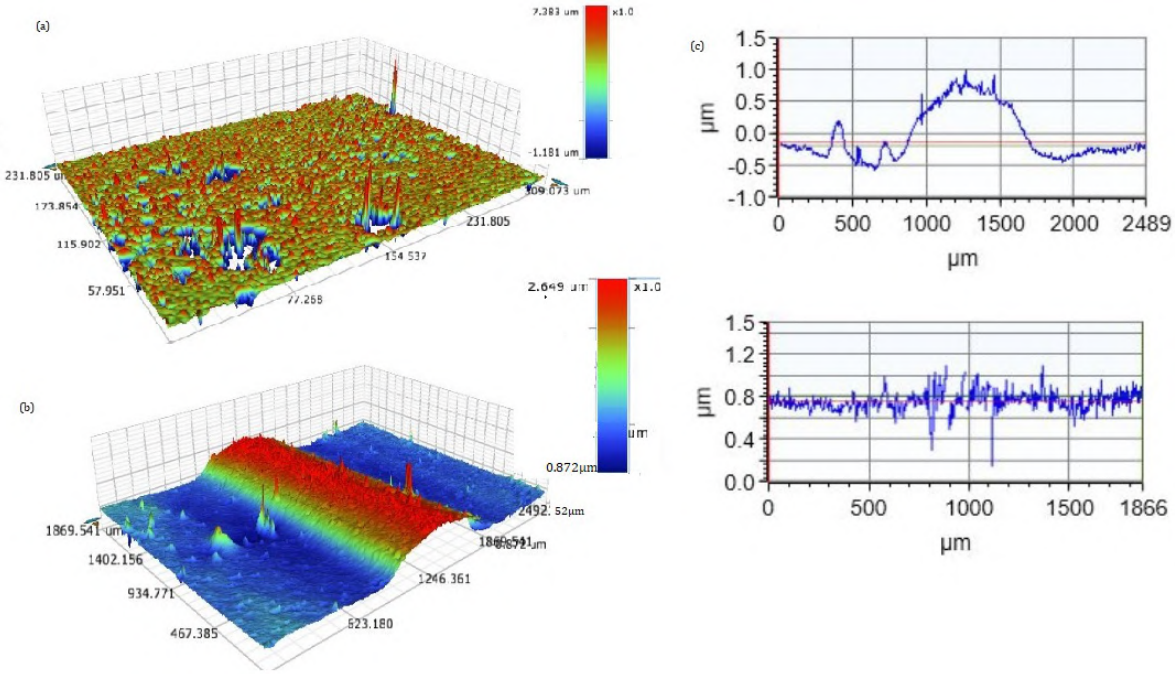

Figure 8.8: (a) Surface topography of Topaz B substrate (b) Surface topography of SERS region and adjacent topaz material (c)X-axis cross-section through red reference point on surface topography (d)Y-axis cross-section through red reference point on surface topography

Rz Analysis		Height Parameters		Hybrid Parameters		Spatial Parameter	
Rpm	6.725μm	Sa	0.121nm	Sdq	12.016°	Str	0.734
Rvm	-1.02μm	Sp	8.175μm				
Rz	7.75μm	Sq	0.285μm				

Table 8.10: Height Profilometry Measurement for Topaz C substrate.

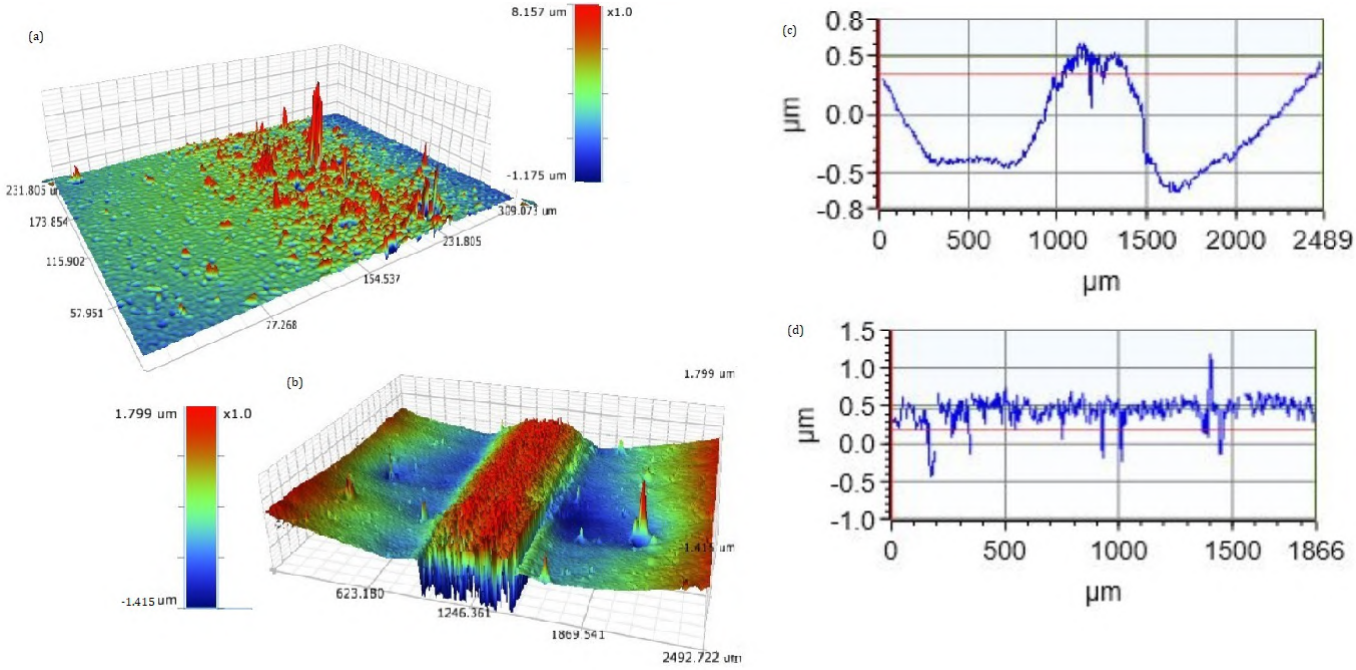

Figure 8.9: (a)Surface topography of Topaz C substrate (b) Surface topography of SERS region and adjacent topaz material (c)X-axis cross-section through red reference point on surface topography (d)Y-axis cross-section through red reference point on surface topography

8.4 ANTIBODY IMMOBILIZATION

Antibody immobilization on the SERS substrate was a logical step forward after surface characterisation with Rhodamine 6G and White light interferometry. This chapter contains details about all such efforts directed at functionalizing the SERS substrate with linker molecules and subsequently with Genetex SARS-CoV-2 antibody. Firstly the methodology of the dilution series of the Genetex antibody will be discuss, then the immobilization protocols are explained, followed by a delineation of the mechanism of the antibody immobilization, finally a series of results obtained during experiments are presented.

8.4.1 Dilution Series of Genetex SARS-CoV-2 Antibody

In other to achieve different concentration for sensitivity analysis of the SERS substrate, the antibody of molar mass 150kDa was diluted according to the scheme in Table 8.11.

The dilution scheme is achieved on the basis of 5μl stock solution of Genetex antibody, on this basis three different diluted solutions were made by pipetting 5μl of antibody in 45μl, 495μl and 4995μl of PBS resulting in a 10X, 100X and 1000X dilutions. PBS is buffer that helps maintain the antibody molecules at the required pH for optimum reactivity with linker molecules. Since the concentration of the stock antibody was 1mg/ml, the stock basis had 5μg of antibody in it, using the avogadros number ($6.023 * 10^{23}$) and its molar mass, the amount of substance(molecules) in the stock solution was $20.1 * 10^{1}2$.

Dilution Action	1mg/ml (1:1)	0.1mg/ml (1:10)	0.01mg/ml (1.100)	1μg/ml (1:1000)
Dilution of 5μl in stock in PBS.	0	45μl	495μl	4995μl
Protein mass in 5μl sample.	5μg	0.5μg	0.05μg	5ng
Number of Antibodies In 5μl sample.	$20.1 * 10^{12}$ $33.4pmol$	$2.01 * 10^{12}$ $3.349pmol$	$0.201 * 10^{12}$ $334fmol$	$20.1 * 10^{9}$ $33.4fmol$
Maximum Density of Antibody in [μmˆ-2] in focal spot of ϕ=10μm.	$1.25 * 10^{6}$ $90 * 10^{6}$	$0.125 * 10^{6}$ $9 * 10^{6}$	$1.25 * 10^{4}$ $0.9 * 10^{6}$	$1.25 * 103$ $9 * 10^{4}$
Surface area of Gold nanoparticle pixel cover per antibody(nmˆ-2).	0.8	8	80	800
Number of 5μl samples per 5μl of stock solutions.	1	10	100	1000

Table 8.11: Dilution Series Table for Genetex SARS-CoV-2 Antibody Using Phosphate buffer saline

8.4.2 Immobilization Protocols

The immobilization protocols defines the procedural steps to be taken to effect the chemisorption of linkers and antibody on the SERS substrate. Two Immobilization strategies(with DSP and Cysteamine Hydrochloride) were employed and discuss below.

Immobilization Strategy with Cysteamine Hydrochloride

1. Using a clean spatula and weighing paper, the appropriate amount of Cysteamine hydrochloride to obtain a desired concentration was fetched and deposited in a UV tight vial and a calculated avoulume of Di water was pipetted into the vial.

2. Shaked the solution so that the Cysteamine Hydrochloride solute can dissolved properly.
   Note: Across the different concentrations prepared, the solution were stored in a freezer at°C.

3. To a cleaned SERS surface of 2mm by 2mm, 7μl of cysteamine hydrochloride solution was pipetted to cover the entire surface. Alternatively, the entire SERS substrate was immerse into the linker solution and allowed to incubate for at least 5hours.

4. After a given incubation period the functionalized SERS substrate was immediately added the protein solution and incubated for 1-4 hours at room temperature.

5. Then the functionalized SERS surface was rinsed with DI water.

Immobilization Strategy with DSP (dithiobis(succinimidyl propionate))

1. Weighed DSP into a tube, and dissolve it in DMSO. To every 4mg DSP a milliliter of DMSO is necessary to cover the gold surface.
   Note: Equilibrate DSP containing bottle to room temperature before opening prevent hydrolysis of the NHS-ester.[Thermofisher, 2008]

2. Gold foil was incubated in dissolved DSP for 30 minutes at room temperature.

3. Rinsed gold foil with DMSO and then with DI water. Gold foil is expected to be activated with NHS groups.[Thermofisher, 2008]
   Note: Then Proceeded directly to the next step; if protein coupling is not performed immediately, the NHS reactive groups will hydrolyze and protein coupling will be negligible.[Thermofisher, 2008]

4. Immediately added the protein solution to the activated gold foil and incubated for 1-4 hours at room temperature.[Thermofisher, 2008]
   Note: Incubation for longer time will not adversely affect conjugation efficiency. However, conjugation does not advance significantly after the first 1-2 hours.

5. Then the functionalized SERS surface was rinsed with buffer to remove crosslinker by-products (NHS leaving groups) and unconjugated protein[Thermofisher, 2008].

8.4.3 Mechanism of the Immobilization protocols

In the immediate previous section the immobilization was presented, in this section, the mechanisms at play will be discussed for both the Cysteamine Hydrochloride and DSP immobilization strategy.

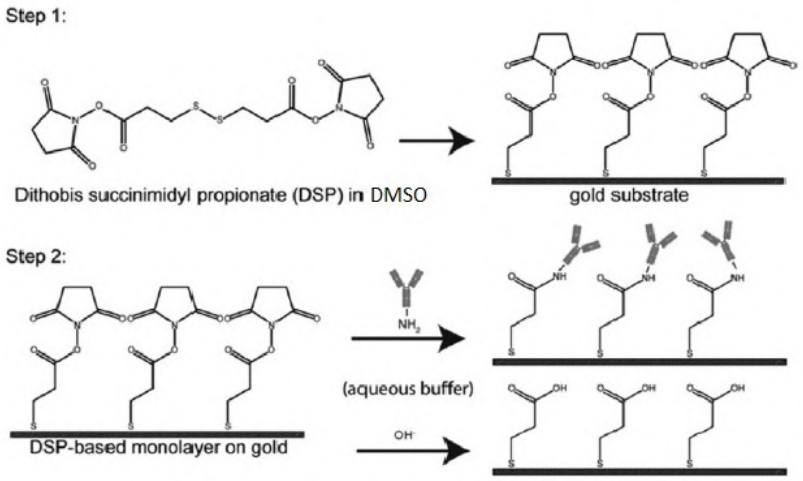

Figure 8.10: Pictorial Schematic of the immobilization of Proteins using DSP.

Mechanism of Immobilization for DSP (dithiobis(succinimidyl propionate))

The mechanism of antibody immobilization is captured in the process called aminolysis. Figure 8.10 shows a schematic two procedure for antibody immobilization using DSP. In the figure shown DSP splits at the disulphide bond and chemisorbs as SAM on the activated gold substrate. Several factors like steric effects, the relative abundance of the amine groups NH_2 and NH_{3+} in solution and the pH of reaction buffer governed the mechanism of immobilization. Amine groups of the antibody act as nucleophiles(i.e deprotonated amines, and electron pair donor).

In any given aqueous protein solution of a particular concentration and pH, there is dynamic balance between the number of NH_2 and NH_3^+ in solution, thus protons leaving NH_3^+ groups binds to the NH_2 instantaneously such that there is no specific population of amines which are protonated at any one time. The molecular specie NH_2 reacts with the NHS group, this disturbs the solution specie balance, hence

equilibrium is restored via the law of mass action with an NH_3^+ group losing a proton to become NH_2 such that the ratio of NH_2 to NH_3^+ is restored for the pH of the solution. This sequence of dynamic balancing will continue until all the molecules have reacted with the NHS. At lower concentration of NH_2 the overall reaction will proceed slowly. A higher pH will make the reaction go faster as there will be more NH_2. NHS readily hydrolysed at higher pH and competes with the reaction with the aminolysis reaction(shown under step 2 in Figure 8.10). A compromise pH of about 7.5 was used to ensure a reasonably fast reaction of the amine and enable enough NHS to survive hydrolysis. The reaction was buffer did not contain any interfering amine(unwanted nucleophiles).

Mechanism of Immobilization for Cysteamine Hydrochloride

In using Cysteamine Hydrochloride for immobilizing antibody, the adsorption of thiols to gold surface starts with the physisorption, during which the sulphur atom binds favourably with H in the sulfhydryl group(-SH). Chemisorption(Covalent bond formation) follows in the form of cleavage of the S atom from the (-SH) group to form the Au-S bond. The presence of the dissociated hydrogen can alter the pH of the reaction microenvironment, thiols are acidic, acidic medium inhibit dissociation, chemisorption to gold occurs more readily in an alkaline environment(aqueous medium) where the aqueous medium acts as a base and scavenge protons.

The Au-S bond is formed by the sharing of overlapping electrons of atomic orbitals of gold and sulphur atoms. Depending on which orbital is involved in the electron pairing, the Au-s bond can be of different length with different bond strength. Bond lengths of 2.30Å to 2.54Å have been recorded to give a bond strength of $47.72 kcal/mol$ and $17.57 kcal/mol$ respectively.

The absorbed cysteamine molecule attached via this Au-S bond coupling takes up different conformations as shown in Figure 8.11. The relative abundance of gauche and trans conformations on any surface is dependent on the concentration cysteamine. The trans conformation is the most desirable as it leaves exposed the amino group of cysteamine for further reaction with N-terminus of the protein, and occupies a smaller surface area when compared to the gauche conformations. In the gauche conformation the NH_2 is coordinated to the SERS surface, this can lead to difficulty in bonding to antibody NH_2 group.

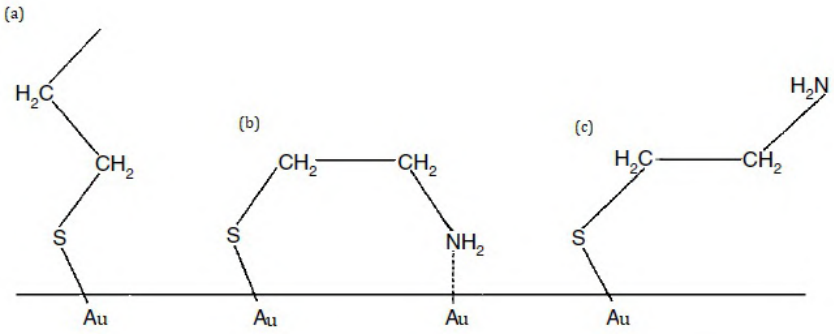

Figure 8.11: Pictorial Schematic of the Conformations of absorbed Cysteamine molecules. (a)Trans conformation (b) Gauche conformation with a amino group attached to the gold surface. (c) Gauche conformation with a amino group free.

A 0.1g mass of cysteamine hydrochloride was weighed and dissolved in 1ml of DI water contained in UV tight vials, this yielded 0.8802M aqueous solution containing $5.301 * 10^{20}$ molecules of cysteamine hydrochloride. 0.0032g of DSP was also weighed and dissolved in $800\mu l$ of DMSO yielding 9.88mM solution containing $5.96 * 10^{18}$ molecules of DSP. In both of these cases the amount of linker substance in solution was more that amount of substance contained in the most concentrated

Setup Window		Acquisition Parameter Window		Acquisition Options Windows	
Objective Lens	50X	Range	400-3500	Delay time	1s
Grating	600gr/mm	Acquisition time	80	Binning	1
ND filter	0.1%	Accumulation	3	Spike filter	Multiple Accumulations
Laser	514nm, 633nm				
Slit	600				
Hole	600				

Table 8.12: Raman Acquisition parameter for SARS-CoV-2 antibody measurements.(applies for both 514nm and 633nm wavelength laser.)

solution of the aliquoted antibody(i.e $20.1 * 10^{12}$), hence there are 100million and 1million more of cysteamine hydrocholride and DSP respectively than antibody in any given volume. Since this experiment was constantly repeated the mass of linker weighed each was a little higher than 0.1g for cysteamine and 0.0032g for DSP, but this only means more amount of linker in solution. So it is sufficient to mentioned that the concentrations stated above were the average per experiments.

The acquisition setup and parameters for Raman measurements on antibody are shown in table Table 8.12, description of the terms in the table are presented in Section B.1.

The immobilization protocol with cysteamine hydrochloride was applied to the SERS surface on topaz A and B and the protocol using DSP was employed to the SERS surface on GCCG, NPG and topaz substrate C. In the first instance all substrates were cleaned accordingly to the cleaning process described in Section 7.6. On samples using protocol with cysteamine hydrochloride, no sign of cysteamine hydrochloride was found on the SERS substrates by the Raman spectrometer, after adequate incubation period substrates employing DSP showed a blank spectral, hence no antibody was chemisorbed on it. The substrate were cleaned with the aforementioned cleaning process along with sonication for 5 minutes in each cleaning solvent, and the immobilization protocols re-applied, On both sets of substrates no signal was detected. The process of cleaning(including sonication for 10 minutes) and reapplying the immobilization protocol was then repeated some five times(there was a cleaning step in between each attempt) while employing an incubation period of at least 12 hours for each set of substrates, no signal of either cysteamine hydrochloride or the Genetex SARS-CoV-2 antibody was detected.

A careful analysis of immobilization protocols and the cleaning procedure led to the conclusion that cleaning needs to be improved, hence all SERS substrates were sonicated as already mentioned and O_2 plasma cleaned for 15minutes each, on applying the DSP immobilization protocols to the topaz C substrate, a blue colored seems to form on the surface of the topaz and flowed across the SERS surface region, this suggested that the topaz region surface of the SERS substrate have become chemically activated by the O_2 and at such reacted with DSP in DMSO producing organic material that formed a thin film that inhibited the SERS effect of the substrate. Both set of functionalized SERS substrate were left to incubate for 12 hours, Raman measurements showed no spectrum of cysteamine hydrochloride or antibody.

Due to the formation of the aforementioned blueish liquid on the surface of topaz substrate, it was decided to continue the immobilization experiments without the topaz substrates.

As a results of multiple useage and the need to obtain credible results, all the initial SERS substrates were discontinued and new SERS substrates were made. While preparing the new GCCG substrates, the cover glass were cleaned and sonicated in acetone, IPA and DI water then its surface was air dried, the cleaned dried surface

was subsequently made hydrophllic (more reactive) by O_2 plasma treatment, so that it can adhere firmly to the gold layer to be deposited according to the procedure outlined in Section 7.8. Four large samples of GCCG were prepared, it was then resolved to employed piranha for cleaning all substrates, glassware and tweezers, see Section 7.6 for a description on cleaning with piranha.

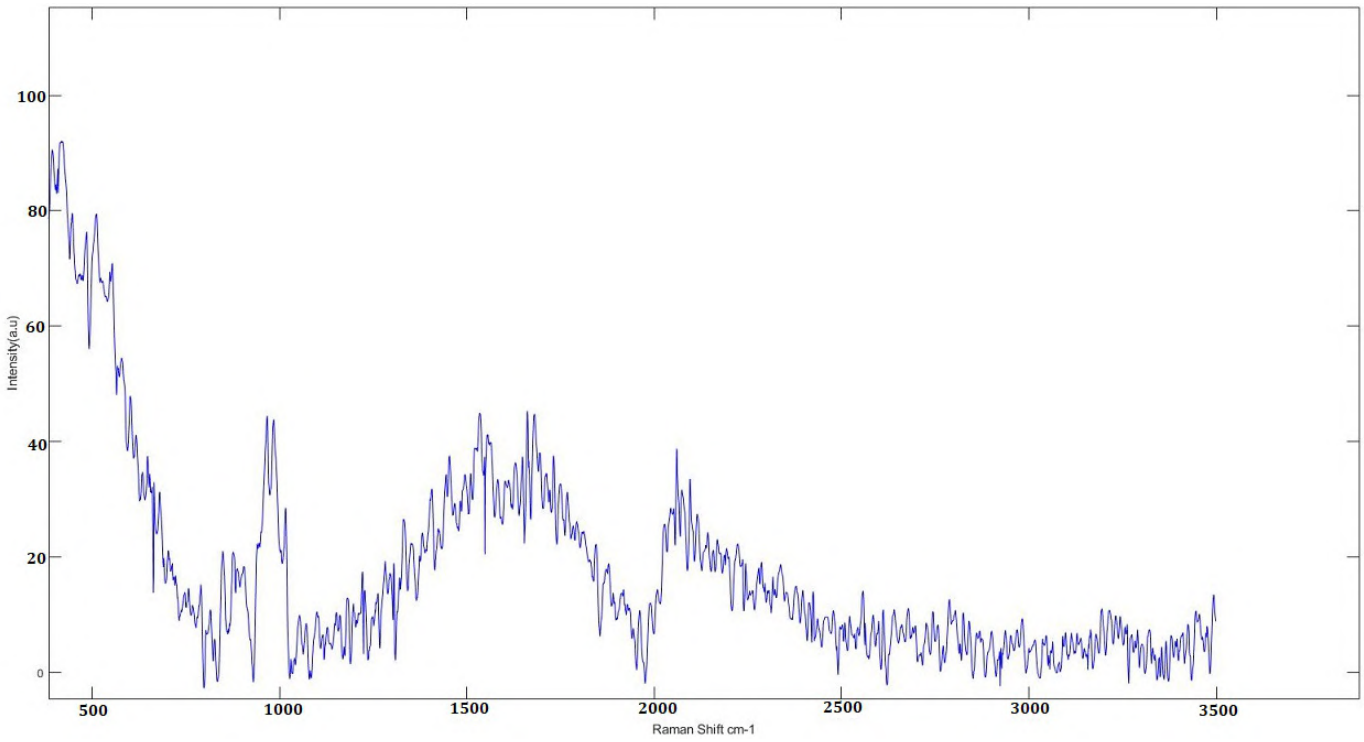

Figure 8.12: Raman Spectra of Antibody on GCCG substrate A measured at 514nm wavelength

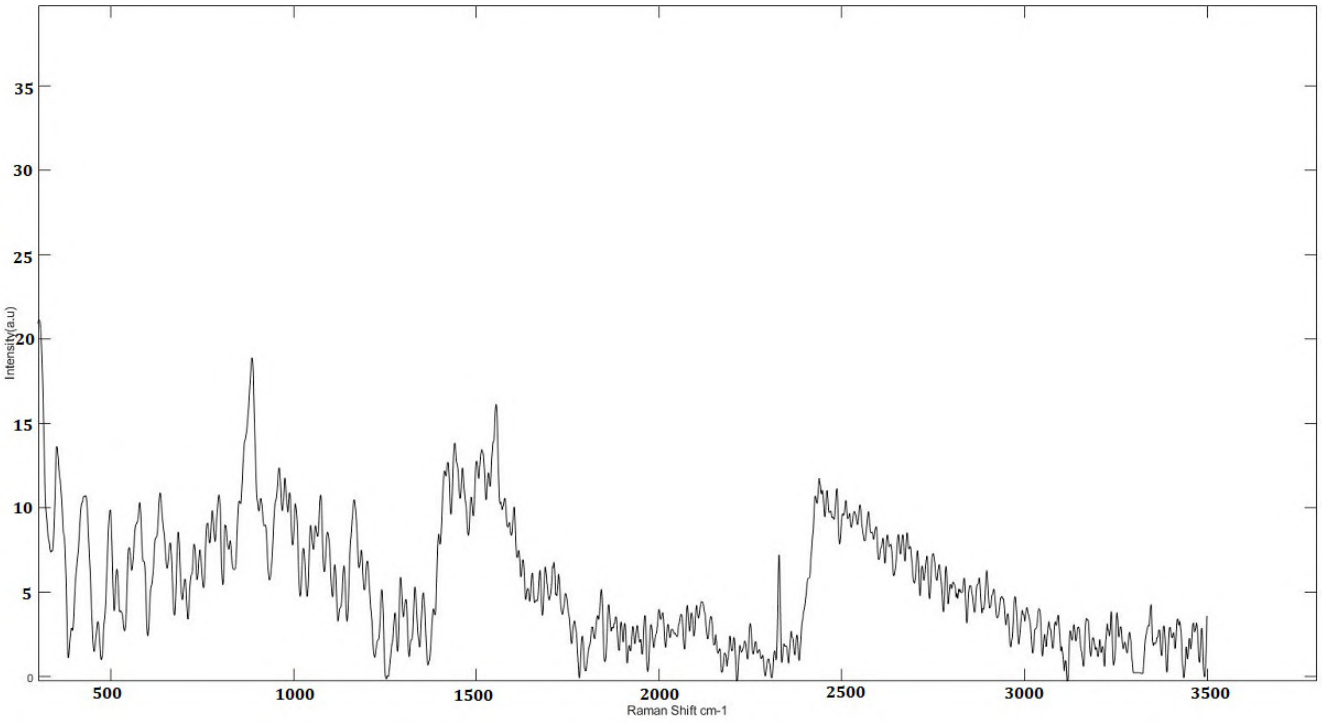

Figure 8.13: Raman Spectra of Antibody on GCCG substrate A measured at 633nm wavelength

One of the large GCCG substrate was split into 5 small gold strips(A,B,C,D and E) by diamond tipped nanoscribe, the strips were then cleaned with piranha. Gold strips A,B,C and D were functionalized with DSP and then incubated in antibody solution of dilution ratio (1:100), while strips E was functionalized with cysteamine hydrochloride solution and incubated accordingly. Figure 8.12 and Figure 8.13 shows the obtained Raman spectrum of Genetex SARS CoV-2 Antibody on substrate GCCG A measured at 514nm and 633nm laser wavelength, the spectrums are qualitatively different from each other, a lot of noise is also present in the measurement. Raman profile broadening is observed for both measurements.

Figure 8.14 and Figure 8.15 are the obtained Raman spectrum of Genetex SARS CoV-2 Antibody on substrate GCCG B measured at 514nm and 633nm laser wavelength respectively, in both spectrums, peaks are found for quantifying the amide I, III, aliphatic and aromatic region in the antibody molecule. However, the inherent presence of so many closely spaced peaks and spectrum broadening in both spectrum's suggest the presence of noise in the measurement.

Figure 8.16 and Figure 8.17 are the obtained Raman spectrum of Genetex SARS CoV-2 Antibody on substrate GCCG C measured at 514nm and 633nm laser wavelength respectively, The Raman spectrum of measurements done with the 514nm laser shows some a concentration of high peaks around 1500 and $2000cm^{-1}$ and a broadened profile around $2000cm^{-1}$, while for measurements done at 633nm high peak concentration is found around 950 and $1500cm^{-1}$ and broadening can be observed $2500cm^{-1}$.

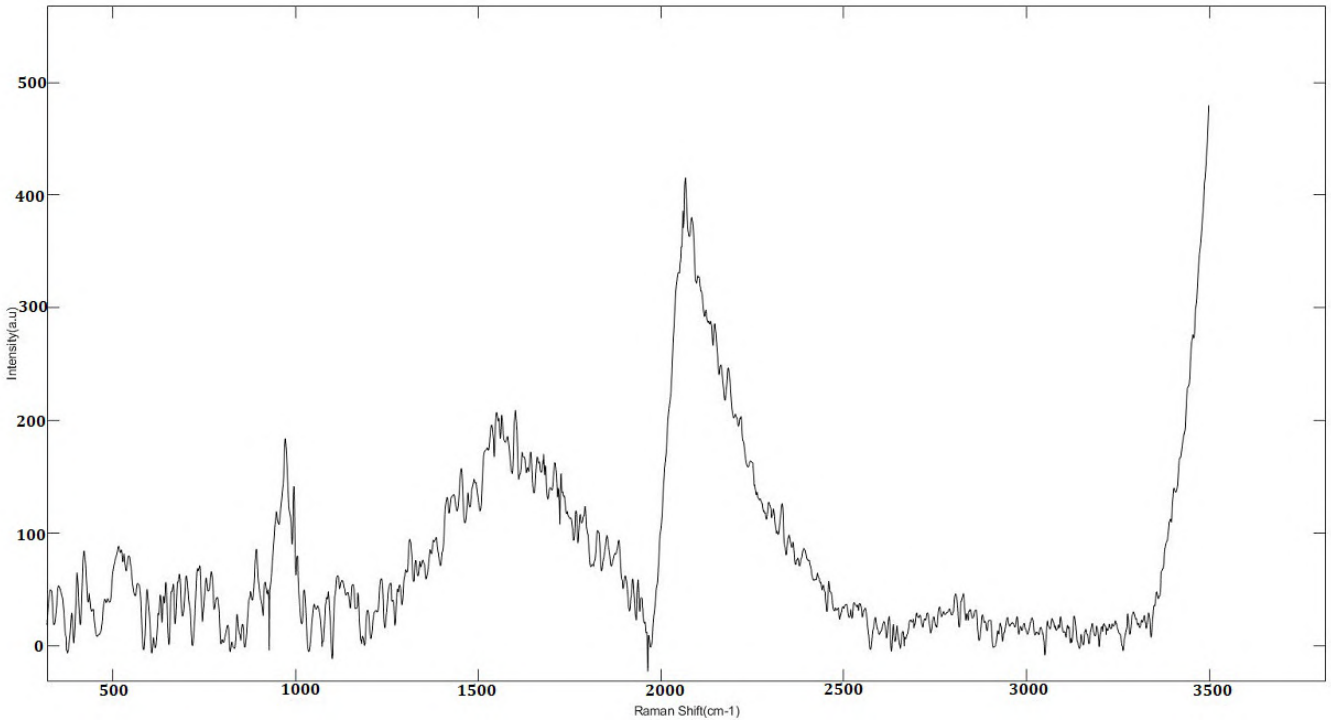

Figure 8.14: Raman Spectra of Antibody on GCCG substrate B measured at 514nm wavelength

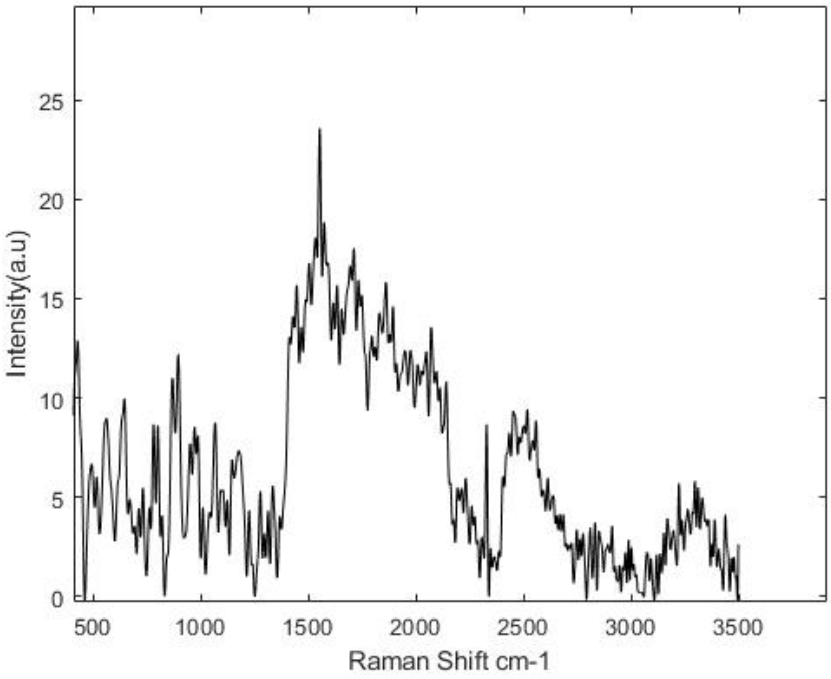

Figure 8.18: Obtained Raman Spectrum of Genetex SARS-CoV-2 Antibody using Cysteamine hydrochloride and a laser wavelength of 633nm

Gold strip D was allowed to incubate in DSP for 10days before removal, this was done in an effort to figure out if time can alter the antibody spectrum and possibly confirm or disprove other spectrum's obtained. Figure 8.19 shows the Raman spectrum obtained for this case, it bears a resemblance to other spectrum's measured at 633nm wavelength.

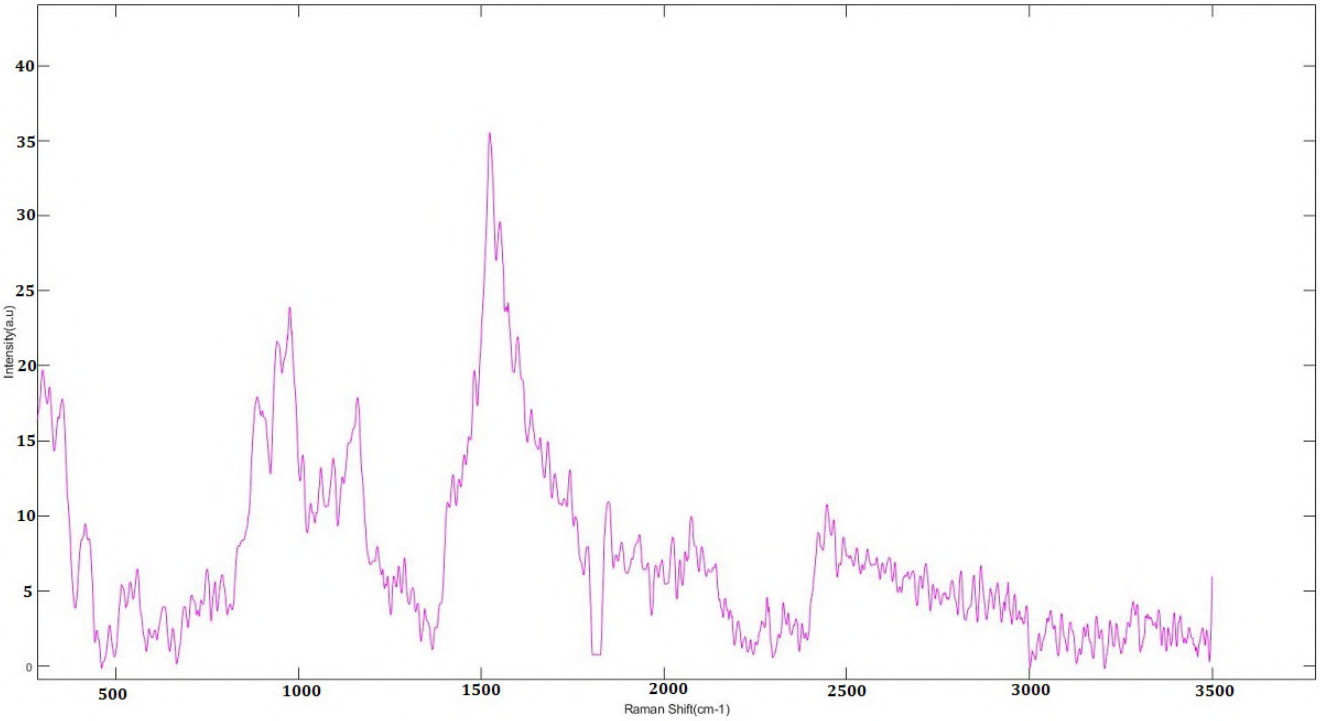

Figure 8.15: Raman Spectra of Antibody on GCCG substrate B measured at 633nm wavelength

Figure 8.18 is the Raman spectrum of the antibody linked using cysteamine hydrochloride and measured at 633nm wavelength, it is qualitatively similar to all other antibody spectrum's measured with the 633nm laser wavelength, these information suggest that the cause of the variation between antibody spectrum's measured at 514nm and 633nm laser wavelength might be substrate and or laser based, the influence of substrate instability is also possible as it is observed that during the cleaning of the gold coated substrates with piranha the gold layer on the cover glass peeled off and in some instances became thinner.

The experiments was then repeated this time to verify or refute the spectrum's already obtained. In this instance 3(X,Y,Z) new gold coated cover glass were cleaned with piranha and the Raman spectrum of these bare non functionalized gold substrates were taken, and are shown in Figure 8.20, the spectrum found for all three substrates were identical and found to possess so much noise. A notably peak in all the spectrum of non functionalized gold substrate is the $2330cm^{-1}$, it is also present in the all measured at both 514nm and 633nm, this is proof of possible substrate interference in the antibody spectrum of initial measurements.

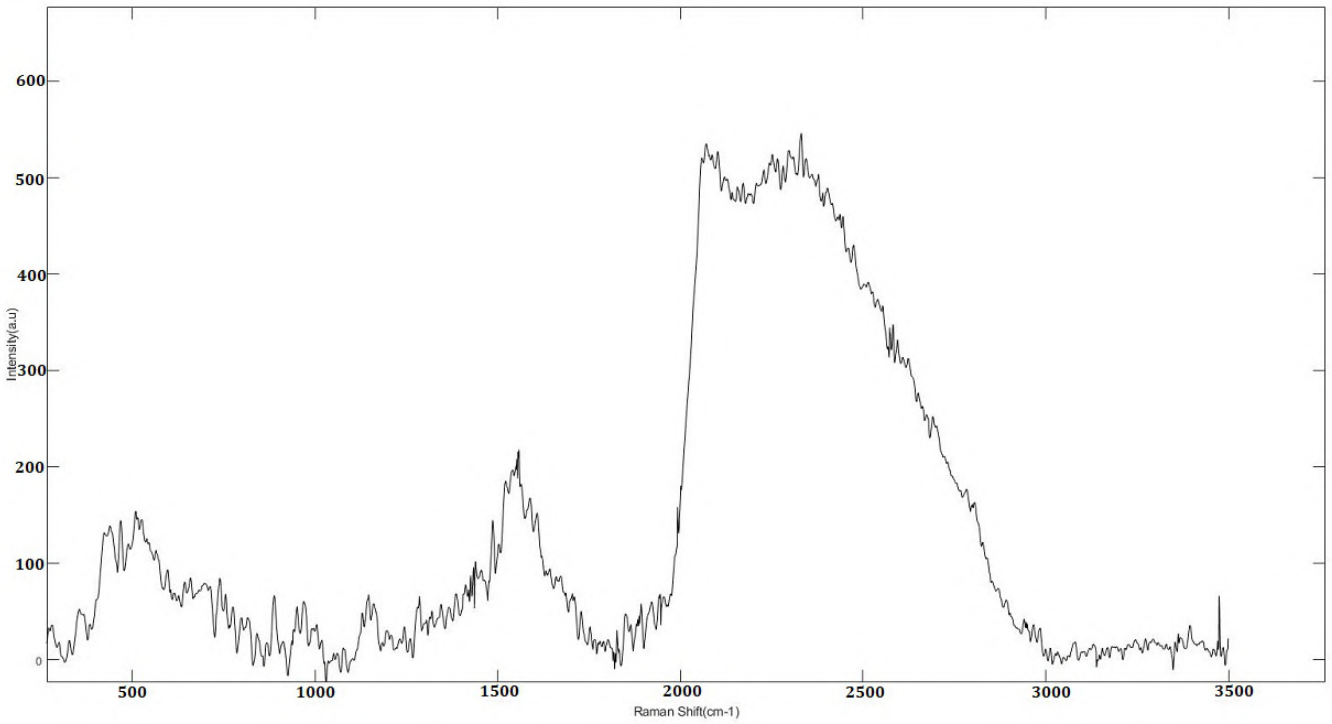

Figure 8.16: Raman Spectra of Antibody on GCCG substrate C measured at 514nm wavelength

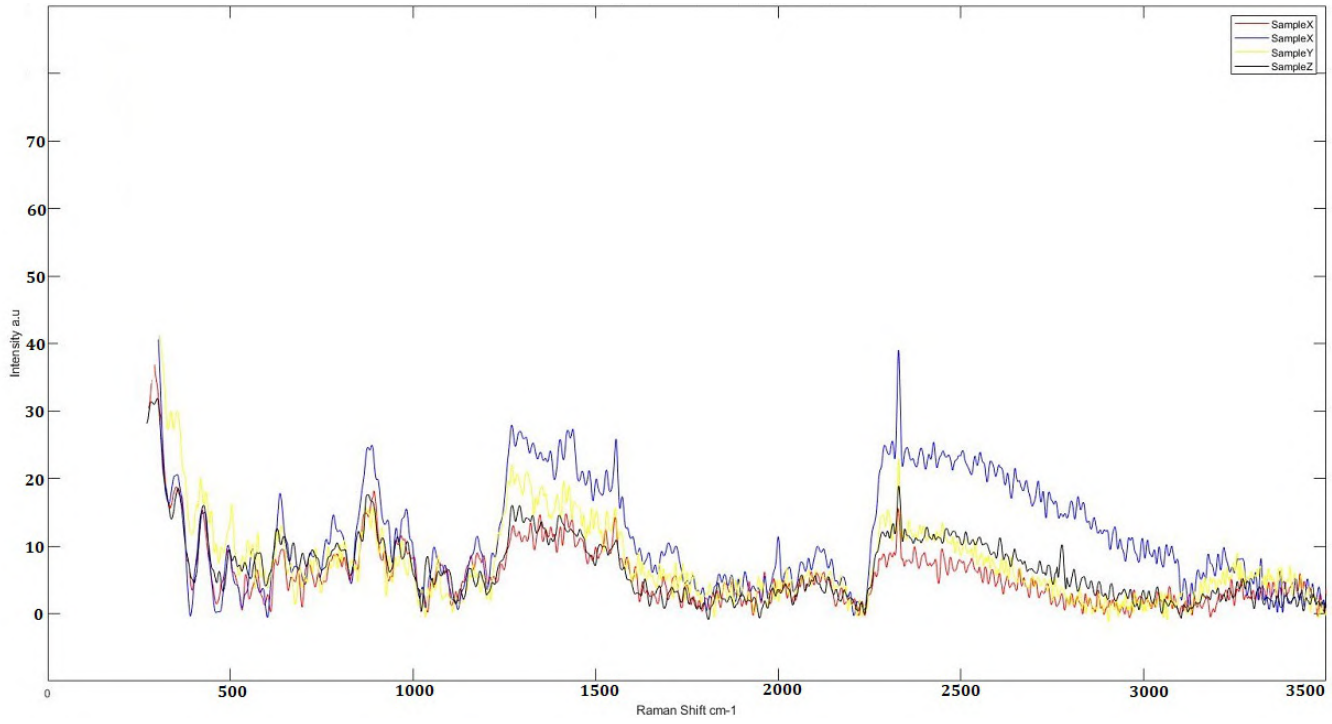

Figure 8.20: Raman spectrum of Non-functionalized GCCG(X,Y,Z)

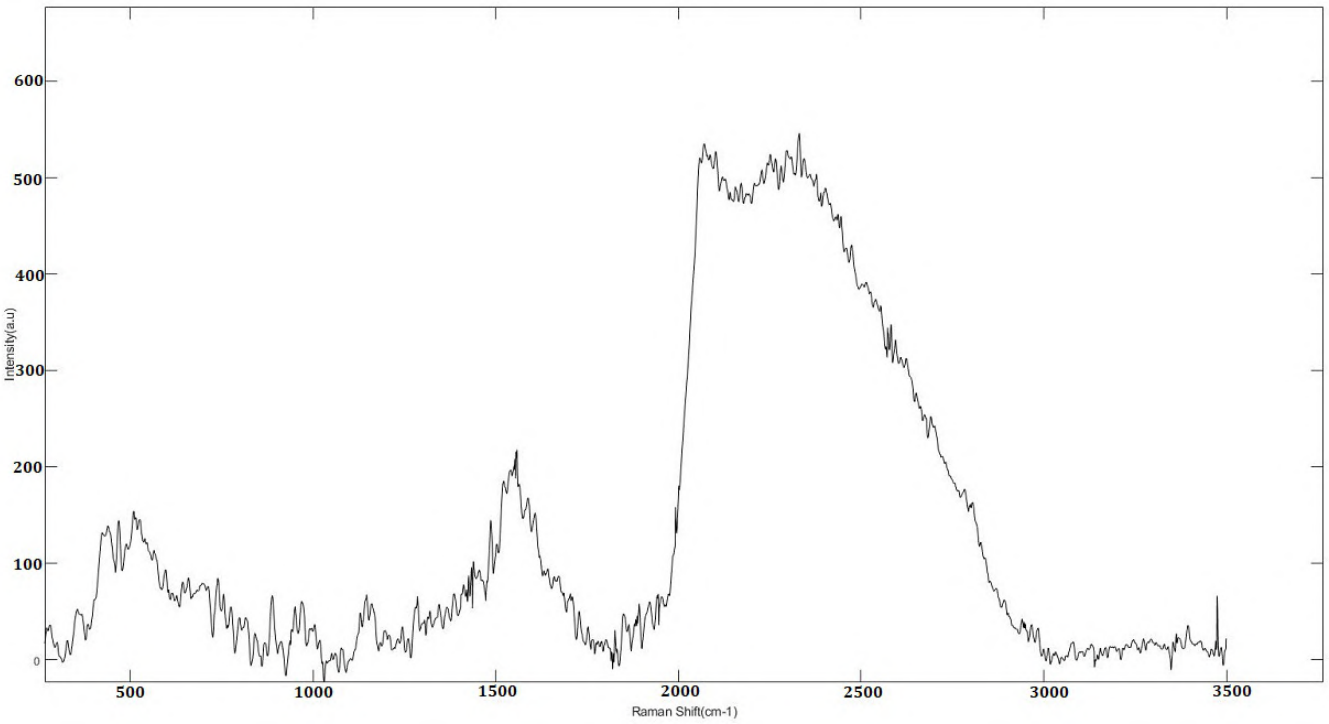

Figure 8.17: Raman Spectra of Antibody on GCCG substrate C measured using a laser wavelength of 633nm

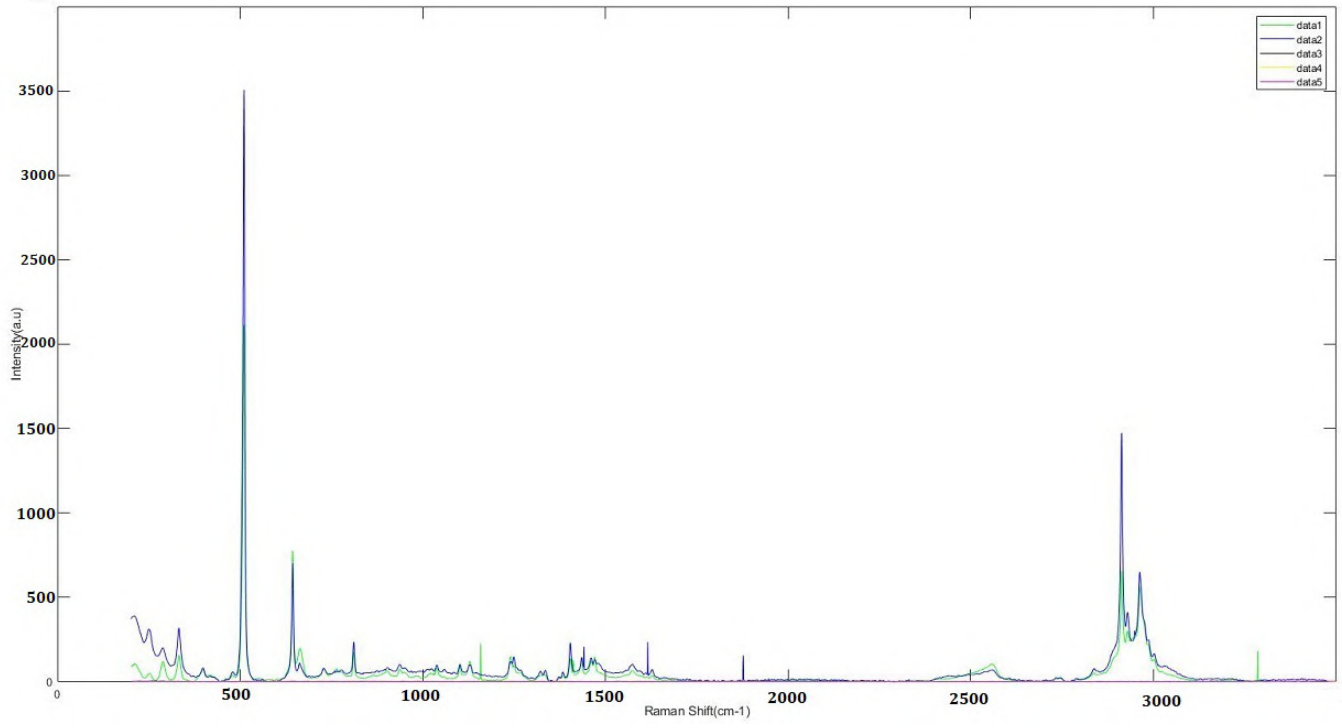

Figure 8.21: Raman spectrum of cysteamine hydrochloride monolayers on substrate GCCG Y.

In other to delineate the observed substrate interference, Substrate X from the new set of GCCG was functionalized according to the cysteamine hydrochloride protocol, Figure 8.21 shows the spectrum of cysteamine hydrochloride monolayers obatined on the surface of GCCG X, five measuremenets were taken across the

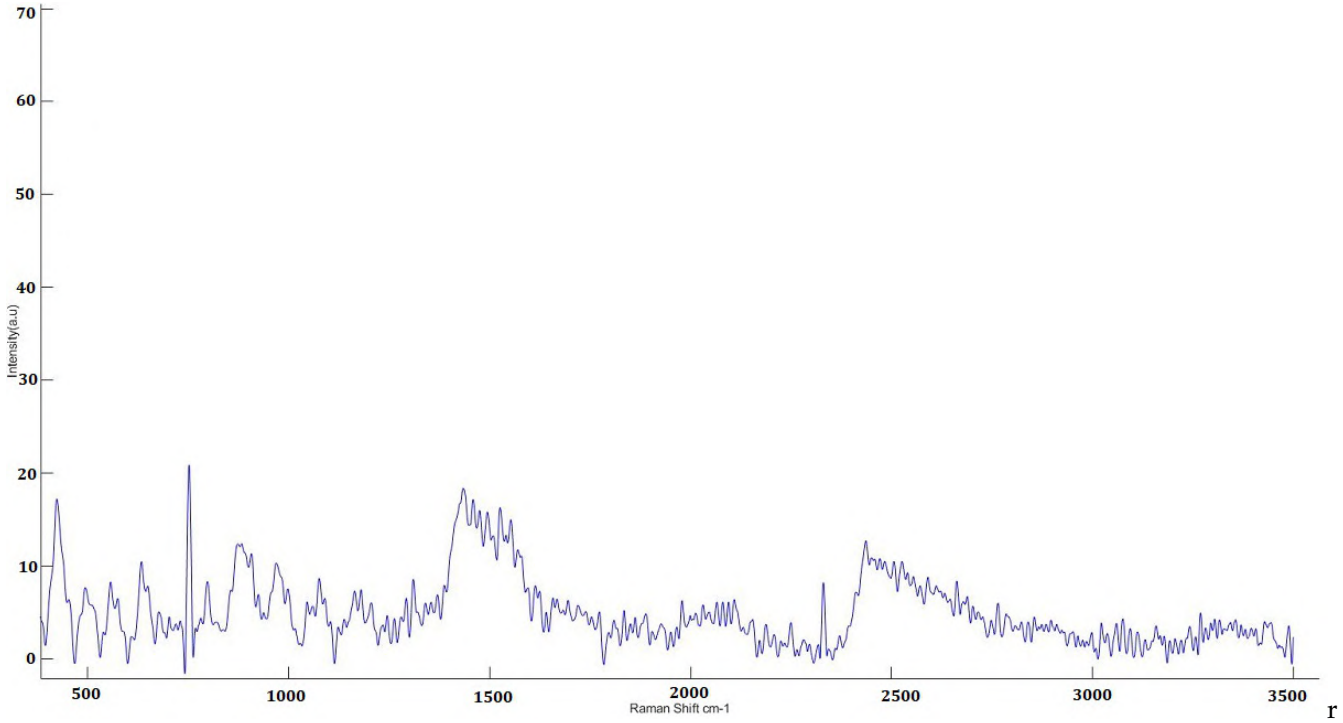

Figure 8.19: Raman Spectrum obtained of Genetex SARS-CoV-2 Antibody after incubation in DSP for 10 days and measuring with a laser wavelength of 633nm

substrate to confirmed reproducibility and evenness of the monolayers, 7μl of Genetex SARS-CoV-2 antibody(with dilution 1:10) was then pi-petted onto the top edge of the functionalized GCCG X substrate and allowed to incubate at room temperature(25°C) four hours. The petri-dish containing the GCCG X as well as other substrate under incubation was wrapped in thin foils to prevent UV denaturation of the protein molecules chemisorbing to the linker monolayers.

Wavenumber Positions(cm^{-1})	**Peak Assignment**	**References**
510	ν(S-S)	[Michota et al., 2001]
643	ν(C-S)	[Kudelski and Hill, 1999]
726	ν(C-S)	[Kudelski and Hill, 1999]
938	ν(C-C(-N))	[Kudelski and Hill, 1999]
1015	ν(C-C(-N))	[Kudelski and Hill, 1999]
2557	ν(S-H) Strongly Hydrogen bonded.	[Kudelski and Hill, 1999]
2928	$\nu_{as}(CH_2)$	[Kudelski and Hill, 1999]
2962	$\nu_s(CH_2)$	[Kudelski and Hill, 1999]

Table 8.13: Some qualifying Peaks in the Raman Spectrum of Cysteamine Hydrochloride monolayers on GCCG X.

The peak designations in Table 8.13 represents the cysteamine hydrochloride monolayers on the GCCG X substrate. The wavenumber positions of $640cm^{-1}$ signifies the existence of the gauche conformer, while 725, 938, 1015 and $2928cm^{-1}$ indicates that the trans conformer of cysteamine hydrochloride is also present.

The concentration of cysteamine hydrochloride solution used in this instance was 0.924M, this molarity value is very high when compared to other values like 5mM, 20mM in literature that had trans conformers predominating, this finding suggests that trans conformers predominated gauche conformers after adsorption from a

concentrated cysteamine solutions. In literature, it is noted that adsorption from a dilute cysteamine solution mainly containing trans conformers in an aqueous medium leads to a predominance of gauche conformers. On a SERS surface orientational and polarizability dependent Raman scattering of chemisorbed molecules dictate the presence of, or the absence of certain vibrational bands.[Kudelski and Hill, 1999]

In the spectrum of cysteamine hydrochloride, there is an absence of the S-H stretching band at $2577cm^{-1}$, this indicates the chemisorption of cysteamine via its thiol group, this occurrence as been already observed for other thiols.[Nuzzo and Allara, 1983] A curious find is observed in the S-S band at $510cm^{-1}$, its presence contradicts the premise that cysteamine was chemisorbed via S-S cleavage. A possible explanation for this occurrence might be that partially dehydrogenized cysteamine transformed to cystamine, which then seems to be adsorbed at the cysteamine-coated surfaces without cleavage of the S-S band.[Kudelski and Hill, 1999]

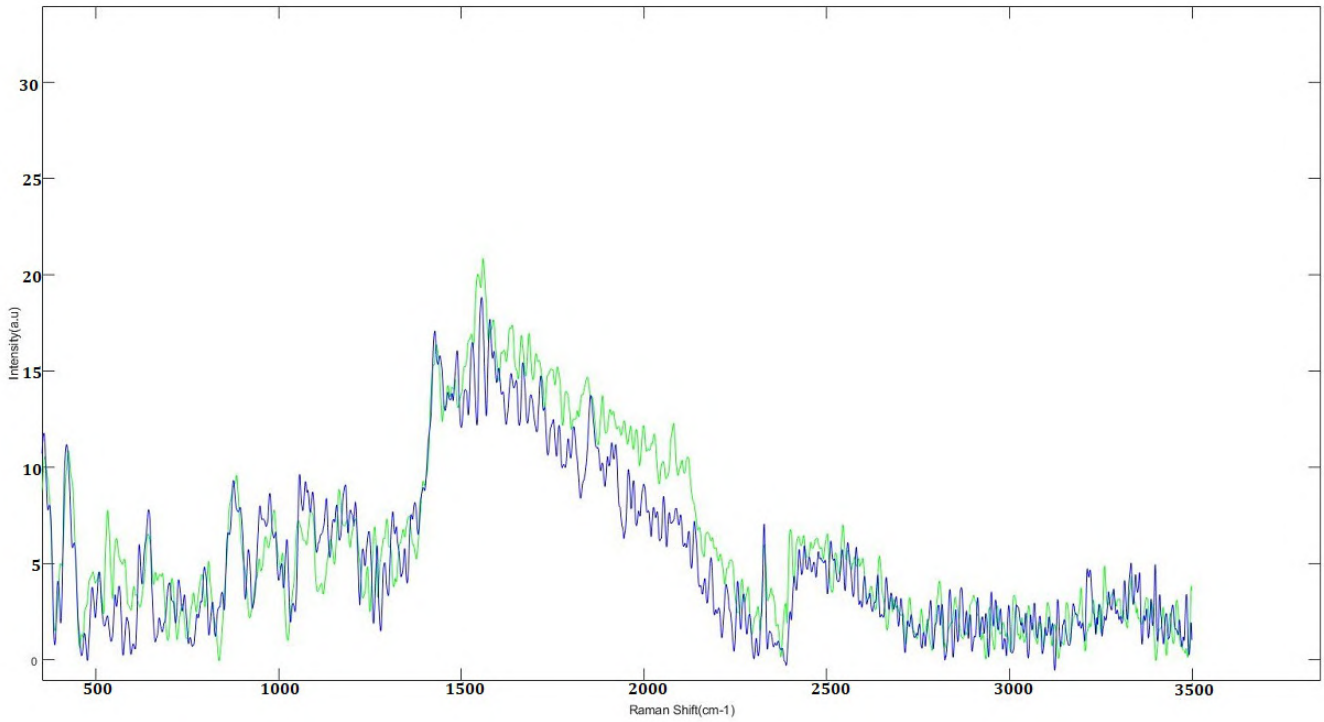

Figure 8.22: Raman Spectrum obtained of Genetex SARS-CoV-2 Antibody on Substrate X

Figure 8.22 shows two Raman measurements of the Genetex SARS-CoV-2 antibody, the measurements are qualitatively the same with a slight difference in peak intensity, the spectrum here is similar to the spectrum's of GCCG samples A,B and C measured at 633nm.

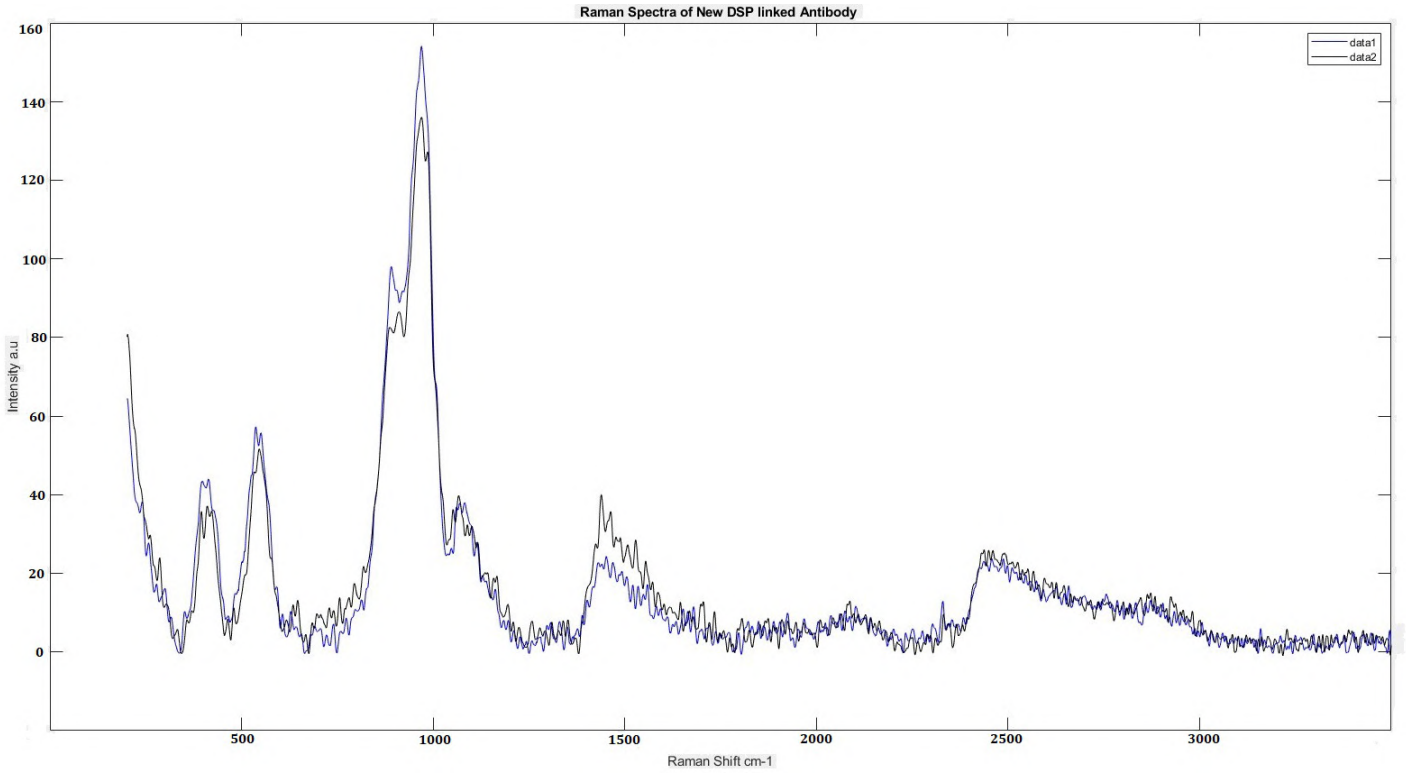

Figure 8.23: Raman Spectrum obtained of Genetex SARS-CoV-2 Antibody on Substrate Y

Substrate GCCG Y was functionalized according to the DSP protocol and 7μl of Genetex SARS-CoV-2 antibody(with dilution 1:10) was then pi-petted onto the top edge of the functionalized GCCG Y substrate and allowed to incubate at room temperature(25°C) for 4hours. It was impossible to check for the presence of NHS esters on the surface of GCCG Y because the protocol stipulated that after immersing the GCCG Y for 30 minutes in a solution of DSP in DMSO, the incubation with antibody should be done immediately to prevent hydrolysis of the NHS ester.

Figure 8.23 represents the Raman spectrum of the antibody on substrate Y before PBS cleaning of the substrate, while Figure 8.24 is the Raman Spectrum after PBS cleaning. A careful observation of Figure 8.23 shows elevated peaks around wavenumber region 500 and $1000cm^{-1}$ and a collection of peaks at a lesser intensity around 1500 to $2000cm^{-1}$. The spectrum of the cleaned substrate shows the same peak distribution, but the region 500 to $1000cm^{-1}$ is some 10 to 14 times smaller than its initial value. Since both spectrum are the same, this observation suggests that the cleaning process resulted in conformational changes of the chemisorbed antibody on the SERS surface, hence the reduced peak intensities, it is also possible that unreacted antibody and other gaseous phase compounds were cleaned off the substrate.

The spectrum's Figure 8.23 and Figure 8.24 are tentative, an analysis of the possible vibrational bands will be presented in chapter nine "Discussions".

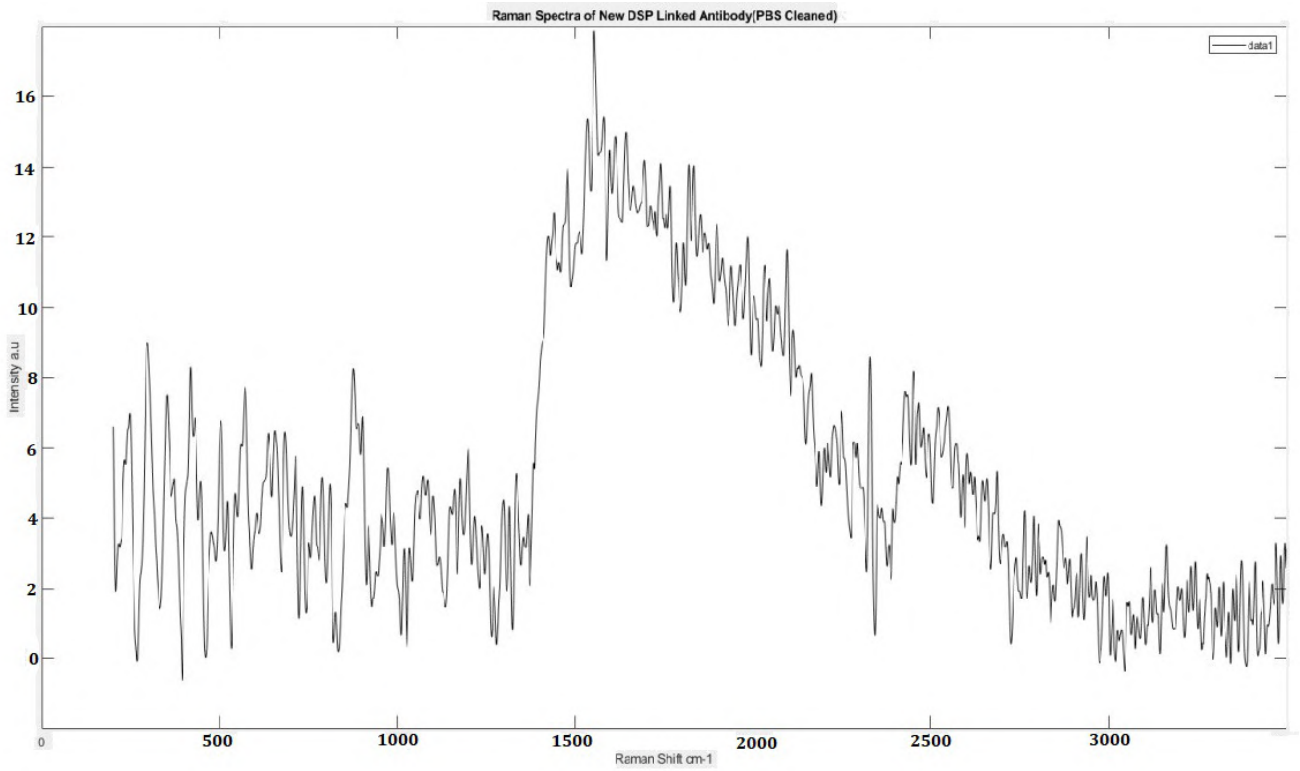

Figure 8.24: Raman Spectrum obtained of Genetex SARS-CoV-2 Antibody on Substrate Y(PBS cleaned)

9 DISCUSSIONS

This chapters contains salient submissions based on observations drawn from the experimental process and results. The problem of Contamination of Nanoporous Gold pores is addressed, surface reaction and assembly of thiols are discussed in relation to the experimental results, a tentative wavenumber assignment of Raman peaks in the obtained spectrum of the Genetex SARS-CoV-2 is presented, the chapter ends with reflections on the tentativeness of the spectrum's obtained.

9.1 CONTAMINATION OF NANOPOROUS GOLD PORES

Nanoporous gold are unique for their high surface area to volume ratio, the structure of nanoporous gold surface used is such that we do not expect to see single atom effects. Hence, the surface can still be regarded as a piece of bulk material with pore size of about 10nm. In Section 8.1 it was observed that after subsequent usage and cleanings steps, the Raman peaks become less intense, this was attributed to clogging of the nanoporous gold pores by organic residue, another explanation of this effect can be an unfavourable distribution of surface coordination atoms, Ibach and co-workers[Ibach, 1997] showed that a lower coordination number of surface atoms results in surface stresses that effect surface chemistry.[Noh and Hara, 2002] Steric hindrances may also result from multiple adsorption of Rhodamine 6G molecules inside the pores of the NPG.

The issue of contamination may also have resulted in an electromagnetic enhancement factor of orders of magnitude 10^3 and 10^4 which is lesser than an expected value of 10^6 as reported in literature.

9.2 SURFACE REACTION OF THIOLS AN GOLD

DSP is a di-n-alkyl disulfide, chemisorption of DSP on clean gold gives self assembly monolayers that are similar to those of the alkanethiols and aminothiols(Cysteamine Hydrochloride)[Biebuyck et al., 1994]. In the case of DSP which was employed as a linker for immobilizing the Genetex antibody, the mechanism of formation of SAMs involved the oxidative addition of S-S bond to the cleaned gold surface forming the Au(I) thiolate (RS-) species.[Ulman, 1996] Equation 9.1 shows the interaction of the di-n-disulfide with gold to form the thiolate species.

$$RS{-}SR + Au_n^o \longrightarrow RS^- Au^+ \cdot Au_n^o \tag{9.1}$$

In the case of aminothiol, the reaction involves an oxidative immobilization of the SH bond to the cleaned gold surface, an a subsequent elimination of hydrogen from the S-H group. [Kraack and Hamm, 2018] The reduced proton probably ends as a H_2 molecule in an exothermic reaction. Equation 9.2 shows this scheme.

$$R{-}S{-}H + Au_n^o \longrightarrow R{-}S^- Au^+ \cdot Au_n^o + \frac{1}{2}H_2 \tag{9.2}$$

The homolytic bond strength of the thiolate group to the gold surface is approximately $40 kcal mol^{-1}$.

9.3 STRUCTURE OF THIOLATES ON GOLD

The predominant bonding pattern of thiol phases on mono-crystalline Au(111) is generally accepted as $(\sqrt{3}x\sqrt{3})$R30° overlayer (R = rotated).[Poirier, 1997a] In literature there is concensus that this lattice organization adopts a secondary ordering of the chains corresponding to a a(4 × 2) superlattice.[Poirier, 1997b] where $(\sqrt{3})$ indicates that the immobilized SAM lattice is 33% larger than the hexagonal lattice arrangement of the gold atoms of the Au(111), a is the lattice constant and it represents the Au−Au interatomic distance on the Au(111) surface. [O'Dwyer et al., 2004]

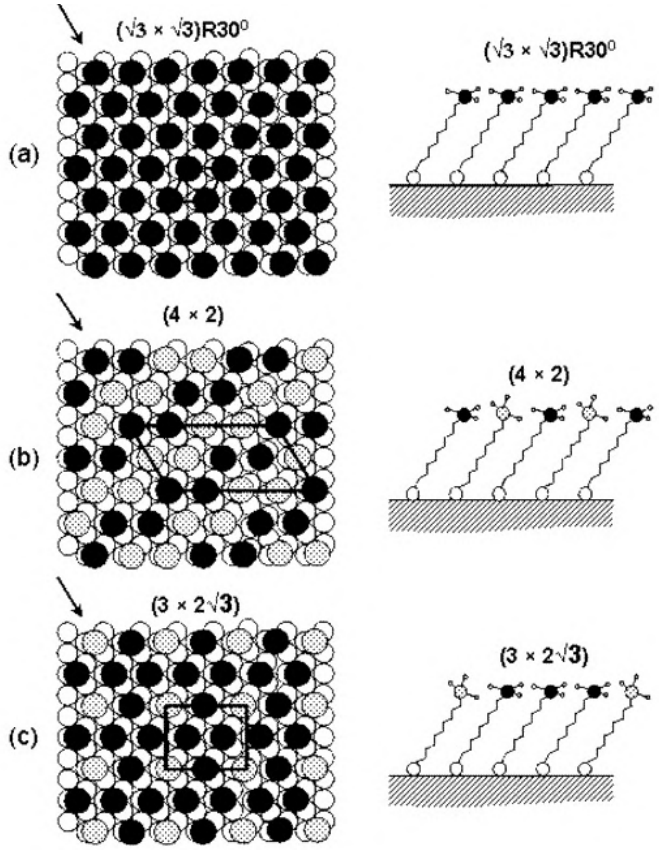

Figure 9.1: (a) Schematic diagram of molecules in the $(\sqrt{3}x\sqrt{3})$R30° lattice (b) Chemisorbed thiol molecules on Au(111) in a (4 × 2) lattice. (c) Chemisorbed thiol molecules in a (3 × 2) superlattice. [Love et al., 2005]

Figure 9.1 shows a cross-sectional view of each thiol overlayer arrangement. Each arrangement is highlighted with a unit mesh in the plan-view schematic as shown in the leftward image of Figure 9.1(a),(b) and (c). In the perfect $(\sqrt{3}x\sqrt{3})$R30° hexagonal packing, all chemisorbed molecules are oriented in the same direction and are tilted 30° from the surface normal to the Au(111), see Figure 9.1(a). Two other principal variations of chemisorbed thiols on Au exist, they both entail a slight alteration to the hexagonal arrangement of monolayers. The first of these is the (4a × 2a) lattice, a is equivalent to 0.29nm. Figure 9.1(b) represents the unit mesh for this structure. The third type is described as the (3a × 2a) superlattice outlined schematically in Figure 9.1(c), both of these additional principal variations in the structure of chemisorbed thiols are based on a hexagonal packing with a periodic variation.[O'Dwyer et al., 2004]

The substrate used in our experiments was indeed poly-crystalline and at such it contained several grains and grain boundaries, this will invariably led to a SAM coverage condition that is different from the one described above.

9.4 MECHANISM OF SELF ASSEMBLY FORMATION

The SAMs adsorbate molecules consist of three sections. The first is the thiol moiety ($-SH$) called the headgroup. The chemisorption of this headgroup to the gold substrate is a critical step in SAMs formation and organisation. The second part consists of the alkyl chain, which can be long or short. Van der Waals interactions between adjacent chains serves as the driving force for adsorbate organization. The third part is the terminal tailgroup, these tailgroups are ideally exposed outward from the surface, they exert the most direct effect on the inter-facial properties of the monolayer.[Elsevier, 2001]

The arrangement of Sulfur moieties on the metal lattice governs the number of immobilization sites available for the binding of the Genetex SARS-CoV-2 antibody, Van-der-waals, hydrogen bonding function to maximally organize the antibody into optimal adlayer structure. The flexibility of the alkyl chain can result in the steric hindrance of the tailgroup of the SAMs, which translates to a less than optimal density of antibodies molecule on the SERS substrate. $(\sqrt{3}x\sqrt{3})R30°$ is the limiting case of overlaying of thiolates. Lateral interactions of the attractive type contribute to the secondary organization of the thiol chains of the a(4×2) superlattice structure.[Kawasaki et al., 2000]

Cysteamine hydrochloride is a short chain aminothiol and as such have lower reactive sticking probabilities on gold surfaces than the longer chain of DSP does.[Zhu et al., 2006] There is a higher chance of adsorption of longer chain thiols. Hence, the formation of thiolate-based structures with limited exposures. After washing of SERS Substrate Y(see Figure 8.23 and Figure 8.24) the Raman intensity peaks decreased, this hints on a possible washing away of physisorbed thiols.

The mechanism of SAMs formation via solution is a complicated dynamic process, this complex dynamics is embodied in a kinetic progression that has a functional form approximated quantitatively by a Langmuir adsorption model [Schreiber, 2000]. As a first approximation the SAMs of thiolates grew according to the Langmuir adsorption model which is characterized by growth rate that is proportional to the number of available sites. The adsorption of thiols on the surface of gold is relatively fast and immediately followed by a much slower step of reorganization of the thiol layer in order to obtain a densely packed monolayer of straight standing molecules.

9.5 TENTATIVE WAVENUMBER ASSIGNMENT FOR THE GENETEX SARS-COV-2 ANTIBODY

This section details the tentative wavenumber assignment of Raman bands as found from experiments. It is tentative because of the amount of noise found in the measurements as already discussed in Figure 8.4.3. Other possible reasons include substrate instabilities occasioned on cleaning, sample preparation, insufficient activation temperature, and overheating of substrate and antibody molecules with laser.

Wavenumber Positions cm^{-1}		**Vibrational Mode**	**Conformation**	**References**
Sample A	Sample B			
504(501)	494(513)	$\nu(S-S)$ Stretch	GGG	[Brandt et al., 2014]
526(522)	530(529)	$\nu(S-S)$ Stretch	GGT	[Brandt et al., 2014]
544(547)	545(549)	$\nu(S-S)$ Stretch	TGT	[Brandt et al., 2014]

Table 9.1: Tentative assignment of Raman Position for the disulfide Bond on samples A and B, value without parenthesis measured at 514nm and that with parenthesis measured at 633nm.

Wavenumber Positions cm^{-1}		**Vibrational Mode**	**Secondary Conformation**	**Reference**
Sample A	Sample B			
1633(1638)	1634	H− bonded C=O	$parallel-\beta-sheet\ \alpha-Helix$	[Wen, 2007]
	(1651)	H− bonded C=O	$\alpha-helix$	[Wen, 2007]
1641(1644)	-	H− bonded C=O	Stretch loose $beta-sheet$	[Wen, 2007]
1662(1669)	-	H− bonded C=O	$\beta-turn$	[Wen, 2007]
(1679)	1670	H− bonded C=O	$\beta-sheet$ and $\beta-Barrel$	[Wen, 2007]

Table 9.2: Tentative assignment of Raman Position for Amide I Bond on samples A and B value without parenthesis measured at514nm and that with parenthesis measured at 633nm.

Wavenumber Positions cm^{-1}		**Vibrational Mode**	**Secondary Conformation**	**References**
Sample A	Sample B			
1231(1224)	-	$\delta(N–H)$ and $\nu(C–H)$	$\beta-sheet$	[Mikhonin et al., 2004]
1258(1257)	-(1245)	$\delta(N–H)$ and $\nu(C–H)$	Random Coil	[Williams, 1986]
1307(1301)	1304,1321 (1312,1314)	$\delta(N–H)$ and $\nu(C–H)$	$\alpha-Helix$	
1330(1338)	1330 (1327)	$\delta(N–H)$ and $\nu(C–H)$	$\alpha-Helix$	[Wen, 2007]

Table 9.3: Tentative assignment of Raman Position for Amide III Bond on samples A and B value without parenthesis measured at 514nm and that with parenthesis measured at 633nm.

Wavenumber Positions cm^{-1}		**Vibrational Mode**	**References**
Sample A	Sample B		
-(653)	-(657)	$\nu(C-S)$	[Williams, 1986]
668(-)	664(-)	$\nu(C-S)$	
710(710)	713,(716)	$\nu(C-S)$	[Mikhonin et al., 2004]
833(834)	825,839(833)	Tyr $\nu-ring$	
938(-)	-	$\nu(CC)\ \alpha-helix$	
1004(1000)	1003(1010)	Phe $\nu-ring$	[Mikhonin et al., 2004]
1401(1407)	-	$\nu_s COO^{-1}$(Asp, Glu)	
1433(1430)	1431(1439)	$\delta_{as}(CH_3), \delta_s(CH_2), \delta(CH)$	[Wen, 2007]
1625(1630)	1626,1620(1638)	$\nu(S-H)$	
2554(2553)	2555,(2556)	$\nu(S-H)$	[Williams, 1986]
2821(2820)	2821(2832)	$\nu(S-H)$	
2859(2854)	2862(2866)	$\nu(S-H)$	[Williams, 1986]
2947(2947)	2938(2939)	$\nu(S-H)$	

Table 9.4: Tentative assignment of Raman Position for Aliphatic and Aromatic side chains on samples A and B value without parenthesis measured at 514nm and that with parenthesis measured at 633nm.

Wavenumber Positions cm^{-1}		**Vibrational Mode**	**Conformation**
Sample X	Sample Y		
494(508)	504	$\nu(S-S)$	GGG
514(520)	522	$\nu(S-S)$	GGT
547()538	544	$\nu(S-S)$	TGT

Table 9.5: Tentative assignment of Raman Position for Disulfide bond on samples X(Cysteamine linked) and Y(DSP linked) value without parenthesis are from first sets of experiment measured at 633nm and that with parenthesis are from the second set of experiments measured at 633nm.

Wavenumber Positions cm^{-1}		**Vibrational Mode**	**Secondary Conformation**
Sample X	Sample Y		
1636(1638)	-	H− bonded C=O	$parallel-\beta-sheet$
1665(1662)	1662	H− bonded C=O	$\beta-turn$
1677	-	H− bonded C=O	$\beta-sheet$ and $\beta-barrel$

Table 9.6: Tentative assignment of Raman Position for Amide I conformations on samples X(Cysteamine linked) and Y(DSP linked) value without parenthesis are from first sets of experiment measured at 633nm and that with parenthesis are from the second set of experiments measured at 633nm.

The above provisional assignment of wavenumbers submits to an analytical mind the need for improvement in the experimental process and measurements methods. The temperature of incubation is key to the chemisorption of thiols and the binding of antibody to the thiolated gold surface.

The Self Assembly Monolayers (SAMs) on the gold surface usually have a high density of defects known as vacany islands, thermal annealing of the SAMs at some 70°to 100°C was reported by Yamada et.al[Yamada et al., 2000] to be optimum for healing defects. However, this annealing process also give room for contamination of the SAMs, a precise control of temperature is required to prevent desorption of

Wavenumber Positions cm^{-1}		**Vibrational Mode**	**Secondary Conformation**
Sample X	Sample Y		
-(1237)	-		$\beta - strand$
1250(1251)	1253		Irregular
-	1272		$\alpha - helix$
1311,1325(1328)	1295		$\alpha - helix$

Table 9.7: Tentative assignment of Raman Position for Amide III conformations on samples X(Cysteamine linked) and Y(DSP linked) value without parenthesis are from first sets of experiment measured at 633nm and that with parenthesis are from the second set of experiments measured at 633nm.

Wavenumber Positions cm^{-1}		**Vibrational Mode**
Sample X	Sample Y	
653(656)	653	$\nu(C-S)$
		$\nu(C-S)$
740(709)	712	$\nu(C-S)$
831(836)		Tyr $\nu - ring$
944(947)		$\nu(CC)\ \alpha - helix$
1005	1008	Phe $\nu - ring$
1400(1402)		$\nu_s COO^{-1}$(Asp, Glu)
1423(1428)	1436	$\delta_{as}(CH_3), \delta_s(CH_2), \delta(CH)$
1557(1552)	1553	Trp $\nu - ring$
1635,1677(-)	1625	$\nu(S-H)$
2542,2678(2557)	2558	$\nu(S-H)$
2718(2823)	2821	$\nu(S-H)$
(2850)	2859	$\nu(S-H)$
(2945)	2945	$\nu(S-H)$

Table 9.8: Tentative assignment of Raman Position for Aliphatic and Aromatic side chains on samples X(Cysteamine linked) and Y(DSP linked) value without parenthesis are from first sets of experiment measured at 633nm and that with parenthesis are from the second set of experiments measured at 633nm.

the thiols from gold. The temperature of the thiol solution is also vital in increasing the certainty of well ordered thiolation and the subsequent antibody immobilization, a higher solution temperature results in larger and well structured $(\sqrt{3}x\sqrt{3})$R30° domains. E. Delamarche et.al[Delamarche et al., 1994] reported that with annealing polycrystalline grains of SAMS fuse from smaller domains into larger ones consequently leading to defect disappearance

10 CONCLUSIONS

Several types of SERS substrate namely NPG, gold nanoparticles on topaz, gold sputtered(coated) on cover glass were fabricated. Nanoporous gold was fabricated by arc-melting of pure noble metal ingots in an argon atmosphere to avoid oxidation. Using the SEM, the porosity of the NPG was verified, SERS characterisation by Rhodamine 6G dye proved an electromagnetic enhancement factor of 10^4 for the clean NPG and 10^3 for the uncleaned NPG, it is also worthy of mentioned that the pores of the NPG were found to be clogged after several use and cleaning steps.

The SERS substrate with gold deposited on cleaned glass showed an EF of 10^4, while all topaz substrate furnished an EF of 10^3. The Root mean square value of surface roughness of SERS substrate(GCCG, NPG and Topaz) increases with the height and width of Gold deposited. An average height of 0.9-1μm was observed across all substrate as been sufficient for the SERS enhancement.

Genetex SARs-CoV-2 antibody immobilization was done with two linkers Cysteamine Hydrochloride and Lomant's reagent, both reagents allowed for the chemisorption of thiols on the surface of cleaned polycrystalline gold surface, emphasis on piranha cleaning due to failure of previous immobilization experiments without this form of substrate cleaning.

The Raman spectrum obtained was same for both protocols, however noise and substrate instability was observed. The presence of Cysteamine Hydrochloride monolayers was confirmed by the Raman peaks $510, 643, 726, 938, 1015, 2557, 2928, and$ $2962cm^{-1}$ each respectively assigned to $\nu(S-S), \nu(C-S), \nu(C-S), \nu(C-C(-N))$, $\nu(C-C(-N)), \nu(S-H), \nu_{as}(CH_2)$ and $\nu_2(CH_2)$.

The characteristic disufide band $500cm^{-1}$, Aliphatic and Aromatic bands, Amide I(1636, 1665, $1678cm^{-1}$) and Amide III(1231, 1258, 1307,1330 cm^{-1}) bands were identified for both linking protocols and tentatively assigned and correlated to secondary protein conformation. Since adsorption of the thiol monolayers was from solution a Langmuir growth model is proposed as the means of thiol growth and orientation.

11 RECOMMENDATIONS

The room for improvement is the biggest room ever, this chapter details brief suggestions on how to improve on the work already done and ultimately achieve the stated goal of developing a point of care device foe the rapid diagnosis of the SARS-CoV-2 virus.

he use of 3− dimensional nanoporous SERS ligament will allow for more surface area for covalent chemisorption of thiols and protein molecules, there will also be a higher chance for electromagnetic enhancement as the array of ligaments will make for ready hotspots.

Due to the instability reported for gold coated on cover glass, I suggest the use of other commercially available SERS substrates like those based on copper and silver.

I propose the use of a different covalent immobilization technique like those based on Amine-glutaraldehyde-Amine, Amine-In-situ generated aldehyde, Amine-N-hydroxysuccinimide NHS, Carboxylate—1-ethyl-3-(3-dimethylamonipropyl) Carbodiimide EDC—amine, Carboxylate + NHS + EDC-Amine, Amine/Sulfhdryl Epoxide, and Amine Isothiocyanate,[Kim and Herr, 2013] this will help to provide corroboration to the already implemented assay.

I suggest in order to improve on the immobilization of the SARS-CoV-2 antibody on gold, an appropriate temperature at which the forward reaction predominates is desirable, a temperature higher than 25°C but less than 40°C.[Johnstone et al., 1990]

BIBLIOGRAPHY

(2020a). Amino acid. Page Version ID: 997226943.

(2020b). Antigen-antibody interaction. Page Version ID: 982628486.

(2020c). Numerical aperture. Page Version ID: 996610963.

(2021). Diffusion. Page Version ID: 999607381.

Absolom, D. R. and van Oss, C. J. (1986). The nature of the antigen-antibody bond and the factors affecting its association and dissociation. *CRC Critical reviews in immunology*, 6(1):1–46.

Aghajani, S., Accardo, A., and Tichem, M. (2020). Aerosol Direct Writing and Thermal Tuning of Copper Nanoparticle Patterns as Surface-Enhanced Raman Scattering Sensors. *ACS Applied Nano Materials*, 3(6):5665–5675.

Albrecht, M. G. and Creighton, J. A. (1977). Anomalously intense Raman spectra of pyridine at a silver electrode. *Journal of the American Chemical Society*, 99(15):5215–5217.

Arevalo, J. H., Taussig, M. J., and Wilson, I. A. (1993). Molecular basis of crossreactivity and the limits of antibody–antigen complementarity. *Nature*, 365(6449):859–863.

Arp, Z., Autrey, D., Laane, J., Overman, S. A., and Thomas, G. J. (2001). Tyrosine Raman Signatures of the Filamentous Virus Ff Are Diagnostic of Non-Hydrogen-Bonded Phenoxyls: Demonstration by Raman and Infrared Spectroscopy of *p* -Cresol Vapor † , ‡. *Biochemistry*, 40(8):2522–2529.

ASME (2020). *Surface texture: surface roughness, waviness, and lay*. OCLC: 1197629204.

Aubrey, K. and Thomas, G. (1991). Raman spectroscopy of filamentous bacteriophage Ff (fd, M13, f1) incorporating specifically-deuterated alanine and tryptophan side chains. Assignments and structural interpretation. *Biophysical Journal*, 60(6):1337–1349.

Banes, P. (2020). Factors affecting the first stage of agglutination - Haemolytic Anaemia.

Barrett, E. J., Revkin, J. H., Young, L. H., Zaret, B. L., Jacob, R., and Gelfand, R. A. (1987). An isotopic method for measurement of muscle protein synthesis and degradation in vivo. *Biochemical Journal*, 245(1):223–228.

Barron, L. D., Hecht, L., and Wilson, G. (1997). The Lubricant of Life: A Proposal That Solvent Water Promotes Extremely Fast Conformational Fluctuations in Mobile Heteropolypeptide Structure †. *Biochemistry*, 36(43):13143–13147.

Basha, I. H. K., Ho, E. T. W., Yousuff, C. M., and Hamid, N. H. B. (2017). Towards Multiplex Molecular Diagnosis-A Review of Microfluidic Genomics Technologies. *Micromachines*, 8(9).

Basile, A., editor (2013). *Handbook of membrane reactors*. Number number 55-56 in Woodhead Publishing Series in Energy. WP, Woodhead Publishing, Oxford ; Philadelphia. OCLC: ocn839934164.

Beebe, D. J., Mensing, G. A., and Walker, G. M. (2002). Physics and Applications of Microfluidics in Biology. *Annual Review of Biomedical Engineering*, 4(1):261–286.

Bhatia, R. B., Brinker, C. J., Gupta, A. K., and Singh, A. K. (2000). Aqueous SolGel Process for Protein Encapsulation. *Chemistry of Materials*, 12(8):2434–2441.

Bhattacharyya, A. and Klapperich, C. M. (2007). Design and testing of a disposable microfluidic chemiluminescent immunoassay for disease biomarkers in human serum samples. *Biomedical Microdevices*, 9(2):245–251.

Bhushan, B. (2000). *Modern Tribology Handbook, Two Volume Set*. CRC Press, 0 edition.

Bhushan, B., Israelachvili, J. N., and Landman, U. (1995). Nanotribology: friction, wear and lubrication at the atomic scale. *Nature*, 374(6523):607–616.

Biebuyck, H. A., Bain, C. D., and Whitesides, G. M. (1994). Comparison of Organic Monolayers on Polycrystalline Gold Spontaneously Assembled from Solutions Containing Dialkyl Disulfides or Alkanethiols. *Langmuir*, 10(6):1825–1831.

bioinformatics, S. (2021). Protein Secondary Structure, Alpha Helices, Beta Sheets, Hairpins And Loops.

Bissonnette, L. and Bergeron, M. G. (2012). Infectious Disease Management through Point-of-Care Personalized Medicine Molecular Diagnostic Technologies. *Journal of Personalized Medicine*, 2(2):50–70.

Blackstock, J. C. (1989). Amino acids and proteins. In *Guide to Biochemistry*, pages 32–52. Elsevier.

Bojorge Ramírez, N., Salgado, A. M., and Valdman, B. (2009). The evolution and developments of immunosensors for health and environmental monitoring: problems and perspectives. *Brazilian Journal of Chemical Engineering*, 26(2):227–249.

Brandt, N., Chikishev, A., Golovin, A., Kruzhilin, V., and Zalevsky, A. (2014). Raman spectroscopy of disulfide bridges in thrombin. *Biomedical Spectroscopy and Imaging*, 3(3):287–292.

Branden, C.-I. and Tooze, J. (1999). *Introduction to protein structure*. Garland Pub, New York, 2nd ed edition.

Butler, J. C., Crengle, S., Cheek, J. E., Leach, A. J., Lennon, D., O'Brien, K. L., and Santosham, M. (2001). Emerging infectious diseases among indigenous peoples. *Emerging Infectious Diseases*, 7(3 Suppl):554–555.

bwtek (2021). Theory of Raman Scattering.

Campion, A., Ivanecky, J. E., Child, C. M., and Foster, M. (1995). On the Mechanism of Chemical Enhancement in Surface-Enhanced Raman Scattering. *Journal of the American Chemical Society*, 117(47):11807–11808.

Carleton (2021). Scanning Electron Microscopy (SEM).

Carr, S. M. (2021). MGA2_03-25.

Chafai, M., Jaouhari, A., Torres, A., Antón, R., Martın, E., Jiménez, J., and Mitchel, W. C. (2001). Raman scattering from LO phonon-plasmon coupled modes and Hall-effect in *n* -type silicon carbide 4H–SiC. *Journal of Applied Physics*, 90(10):5211–5215.

Chalmers, J. M., Edwards, H. G. M., and Hargreaves, M. D., editors (2012). *Infrared and Raman spectroscopy in forensic science*. Wiley, Oxford. OCLC: 781670697.

Chemistry, W. (2021). Chapter 2: Protein Structure – Chemistry.

Chin, C. D., Linder, V., and Sia, S. K. (2007). Lab-on-a-chip devices for global health: Past studies and future opportunities. *Lab Chip*, 7(1):41–57.

Chittaranjan Sahay, S. G. (2018). Conference Overview American Society for Engineering Education.

Chiu, M. L., Goulet, D. R., Teplyakov, A., and Gilliland, G. L. (2019). Antibody Structure and Function: The Basis for Engineering Therapeutics. *Antibodies*, 8(4):55.

Cirimele, V., Kintz, P., Lohner, S., and Ludes, B. (2003). Enzyme Immunoassay Validation for the Detection of Buprenorphine in Urine. *Journal of Analytical Toxicology*, 27(2):103–105.

Colman, P. M. (1989). Protein-Protein Interactions and Immune Recognition. In Melchers, F., Albert, E. D., von Boehmer, H., Dierich, M. P., Du Pasquier, L., Eichmann, K., Gemsa, D., Götze, O., Kalden, J. R., Kaufmann, S. H. E., Kirchner, H., Resch, K., Riethmüller, G., Schimpl, A., Sorg, C., Steinmetz, M., Wagner, H., and Zachau, H. G., editors, *Progress in Immunology*, pages 1240–1245. Springer Berlin Heidelberg, Berlin, Heidelberg.

Colthup, N. B. (1990). *Introduction to infrared and Ramanspectroscopy [electronic resource*. Academic Press, Boston. OCLC: 952857968.

Combs, A., McCann, K., Autrey, D., Laane, J., Overman, S. A., and Thomas, G. J. (2005). Raman signature of the non-hydrogen-bonded tryptophan side chain in proteins: experimental and ab initio spectra of 3-methylindole in the gas phase. *Journal of Molecular Structure*, 735-736:271–278.

Convery, N. and Gadegaard, N. (2019). 30 years of microfluidics. *Micro and Nano Engineering*, 2:76–91.

Covachem (2021). DSP Crosslinker.

Darwish, I. A. (2006). Immunoassay Methods and their Applications in Pharmaceutical Analysis: Basic Methodology and Recent Advances. *International journal of biomedical science: IJBS*, 2(3):217–235.

Davies (1988). Antibody-antigen complexes. *The Journal of Biological Chemistry*, 263(22):10541–10544.

Davison, A. (2020). ICTV 9th Report (2011).

Deepak, F. L., editor (2018). *Metal Nanoparticles and Clusters: Advances in Synthesis, Properties and Applications*. Springer International Publishing : Imprint: Springer, Cham, 1st ed. 2018 edition.

Delamarche, E., Michel, B., Kang, H., and Gerber, C. (1994). Thermal Stability of Self-Assembled Monolayers. *Langmuir*, 10(11):4103–4108.

Dick, L. A., Haes, A. J., and Van Duyne, R. P. (2000). Distance and Orientation Dependence of Heterogeneous Electron Transfer: A Surface-Enhanced Resonance Raman Scattering Study of Cytochrome *c* Bound to Carboxylic Acid Terminated Alkanethiols Adsorbed on Silver Electrodes. *The Journal of Physical Chemistry B*, 104(49):11752–11762.

Downes, A. and Elfick, A. (2010). Raman Spectroscopy and Related Techniques in Biomedicine. *Sensors*, 10(3):1871–1889.

Dresel, T., Häusler, G., and Venzke, H. (1992). Three-dimensional sensing of rough surfaces by coherence radar. *Applied Optics*, 31(7):919.

Ducrée, J. (2012). Special Issue: Microfluidic Lab-on-a-Chip Platforms for High-Performance Diagnostics. *Diagnostics (Basel, Switzerland)*, 2(1):1.

ECDC (2020). Coronaviruses. *European Centre for Disease Prevention and Control*.

Edelman, G. M. and Benacerraf, B. (1962). ON STRUCTURAL AND FUNCTIONAL RELATIONS BETWEEN ANTIBODIES AND PROTEINS OF THE GAMMA-SYSTEM. *Proceedings of the National Academy of Sciences*, 48(6):1035–1042.

Efremov, E. V., Buijs, J. B., Gooijer, C., and Ariese, F. (2007). Fluorescence rejection in resonance Raman spectroscopy using a picosecond-gated intensified charge-coupled device camera. *Applied Spectroscopy*, 61(6):571–578.

Elsevier (2001). *Encyclopedia of materials: science and technology*. Elsevier, Amsterdam ; New York.

Elveflow (2021). The history of microfluidics.

Enjuanes, L., Smerdou, C., Castilla, J., Antón, I. M., Torres, J. M., Sola, I., Golvano, J., Sánchez, J. M., and Pintado, B. (1995). Development of Protection against Coronavirus Induced Diseases: A Review. 380:197–211.

Faccio, G. (2018). From Protein Features to Sensing Surfaces. *Sensors (Basel, Switzerland)*, 18(4).

Fauci, A. S. (2001). Infectious diseases: considerations for the 21st century. *Clinical Infectious Diseases: An Official Publication of the Infectious Diseases Society of America*, 32(5):675–685.

Fauci, A. S. and Morens, D. M. (2016). Zika Virus in the Americas — Yet Another Arbovirus Threat. *New England Journal of Medicine*, 374(7):601–604.

Fehr, A. R. and Perlman, S. (2015). Coronaviruses: An Overview of Their Replication and Pathogenesis. 1282:1–23.

Fischer, E. (1894). Einfluss der Configuration auf die Wirkung der Enzyme. *Berichte der deutschen chemischen Gesellschaft*, 27(3):2985–2993.

Fleischmann, M., Hendra, P., and McQuillan, A. (1974). Raman spectra of pyridine adsorbed at a silver electrode. *Chemical Physics Letters*, 26(2):163–166.

Fluigent (2021). Physics of Microfluidics - Basic Properties of Microfluidic Flows.

Garcia-Vaquero, M., Rajauria, G., O'Doherty, J., and Sweeney, T. (2017). Polysaccharides from macroalgae: Recent advances, innovative technologies and challenges in extraction and purification. *Food Research International*, 99:1011–1020.

Getzoff, E. D., Geysen, H. M., Rodda, S. J., Alexander, H., Tainer, J. A., and Lerner, R. A. (1987). Mechanisms of antibody binding to a protein. *Science (New York, N.Y.)*, 235(4793):1191–1196.

Goldberg, R. J. (1952). A Theory of Antibody—Antigen Reactions. I. Theory for Reactions of Multivalent Antigen with Bivalent and Univalent Antibody ². *Journal of the American Chemical Society*, 74(22):5715–5725.

goldbio (2021). Cysteamine hydrochloride | GoldBio.

Goldsby, R. A. and Goldsby, R. A., editors (2003). *Immunology*. W.H. Freeman, New York, 5th ed edition.

Gralinski, L. E. and Menachery, V. D. (2020). Return of the Coronavirus: 2019-nCoV. *Viruses*, 12(2).

Grossberg, A. L. and Pressman, D. (1968). Modification of arginine in the active sites of antibodies. *Biochemistry*, 7(1):272–279.

Gu, J., Han, B., and Wang, J. (2020). COVID-19: Gastrointestinal Manifestations and Potential Fecal-Oral Transmission. *Gastroenterology*, 158(6):1518–1519.

Guarrotxena, N., Liu, B., Fabris, L., and Bazan, G. C. (2010). Antitags: Nanostructured Tools for Developing SERS-Based ELISA Analogs. *Advanced Materials*, 22(44):4954–4958.

Hammes, G. G. and Hammes, G. G. (2005). *Spectroscopy for the biological sciences*. Wiley-Interscience, Hoboken, N.J. OCLC: 175314353.

Hamming, I., Timens, W., Bulthuis, M. L. C., Lely, A. T., Navis, G. J., and van Goor, H. (2004). Tissue distribution of ACE2 protein, the functional receptor for SARS coronavirus. A first step in understanding SARS pathogenesis. *The Journal of Pathology*, 203(2):631–637.

Hermanson, G. T. (2008). *Bioconjugate techniques*. Academic Press, San Diego, 2nd edition edition.

Herrero, A. M. (2008). Raman Spectroscopy for Monitoring Protein Structure in Muscle Food Systems. *Critical Reviews in Food Science and Nutrition*, 48(6):512–523.

HORIBA (2017). Horiba labspec suite operating manual.

HORIBA (2020). Raman Accessories - Specialised Objectives - HORIBA.

Hu, B., Guo, H., Zhou, P., and Shi, Z.-L. (2020). Characteristics of SARS-CoV-2 and COVID-19. *Nature Reviews Microbiology*.

Hu, J., Wang, S., Wang, L., Li, F., Pingguan-Murphy, B., Lu, T. J., and Xu, F. (2014). Advances in paper-based point-of-care diagnostics. *Biosensors and Bioelectronics*, 54:585–597.

Huang, M., Galarreta, B. C., Cetin, A. E., and Altug, H. (2013). Actively transporting virus like analytes with optofluidics for rapid and ultrasensitive biodetection. *Lab on a Chip*, 13(24):4841.

Ibach, H. (1997). The role of surface stress in reconstruction, epitaxial growth and stabilization of mesoscopic structures. *Surface Science Reports*, 29(5-6):195–263.

ibsen (2020). Raman Instrumentation - Check Out our Guide.

Inc, R. (2021). Viscosity of Newtonian and Non-Newtonian Fluids.

inPhotonics (2020). InPhotonics: Our product line for Raman spectroscopy.

integratedoptics (2020). Raman Spectroscopy.

Iridian (2020). Optical Filters, Raman Spectroscopy.

Israelachvili, J. N. (2011). *Intermolecular and surface forces*. Elsevier, Academic Press, Amsterdam, third edition edition. OCLC: 249272556.

Janeway (2001). *Immunobiology: the immune system in health and disease ; [animated CD-ROM inside]*. Garland Publ. [u.a.], New York, NY, 5. ed edition. OCLC: 47320420.

Jeanmaire, D. L. and Van Duyne, R. P. (1977). Surface raman spectroelectrochemistry. *Journal of Electroanalytical Chemistry and Interfacial Electrochemistry*, 84(1):1–20.

Jenkins, G. and Mansfield, C. D. (2013). *Microfluidic Diagnostics: Methods and Protocols*, volume 949 of *Methods in Molecular Biology*. Humana Press, Totowa, NJ.

Jensen, L., Aikens, C. M., and Schatz, G. C. (2008). Electronic structure methods for studying surface-enhanced Raman scattering. *Chemical Society Reviews*, 37(5):1061.

Johnstone, R. W., Andrew, S. M., Hogarth, M. P., Pietersz, G. A., and McKenzie, I. F. (1990). The effect of temperature on the binding kinetics and equilibrium constants of monoclonal antibodies to cell surface antigens. *Molecular Immunology*, 27(4):327–333.

Jones, R. R., Hooper, D. C., Zhang, L., Wolverson, D., and Valev, V. K. (2019). Raman Techniques: Fundamentals and Frontiers. *Nanoscale Research Letters*, 14(1):231.

Kawasaki, M., Sato, T., Tanaka, T., and Takao, K. (2000). Rapid Self-Assembly of Alkanethiol Monolayers on Sputter-Grown Au(111). *Langmuir*, 16(4):1719–1728.

KhanAcademy (2021). Protein structure: Primary, secondary, tertiary & quatrenary (article).

Kim, D. and Herr, A. E. (2013). Protein immobilization techniques for microfluidic assays. *Biomicrofluidics*, 7(4):041501.

Kino, G. S. and Chim, S. S. C. (1990). Mirau correlation microscope. *Applied Optics*, 29(26):3775.

Koch, A. W., editor (1998). *Optische Meßtechnik an technischen Oberflächen: praxisorientierte lasergestützte Verfahren zur Untersuchung technischer Objekte hinsichtlich Form, Oberflächenstruktur und Beschichtung ; mit 4 Tabellen und 418 Literaturstellen*. expert-Verl, Renningen-Malmsheim. OCLC: 75768763.

Kraack, J. P. and Hamm, P. (2018). Solvent-Controlled Morphology of Catalytic Monolayers at Solid–Liquid Interfaces. *The Journal of Physical Chemistry C*, 122(4):2259–2267.

Krimm, S. and Bandekar, J. (1986). Vibrational Spectroscopy and Conformation of Peptides, Polypeptides, and Proteins. In *Advances in Protein Chemistry*, volume 38, pages 181–364. Elsevier.

Kudelski, A. and Hill, W. (1999). Raman Study on the Structure of Cysteamine Monolayers on Silver. *Langmuir*, 15(9):3162–3168.

Kukura, P., McCamant, D. W., and Mathies, R. A. (2007). Femtosecond stimulated Raman spectroscopy. *Annual Review of Physical Chemistry*, 58:461–488.

Kumagai, I. and Tsumoto, K. (2002). Antigen-Antibody Binding. In John Wiley & Sons, Ltd, editor, *Encyclopedia of Life Sciences*, page a0001117. John Wiley & Sons, Ltd, Chichester, UK.

Lai, M. (2002). Coronavirus. page emm0280.

Larkin, K. G. (1996). Efficient nonlinear algorithm for envelope detection in white light interferometry. *Journal of the Optical Society of America A*, 13(4):832.

Larkin, P. (2018). *Infrared and Raman spectroscopy: principles and spectral interpretation*. Elsevier, Amsterdam, Netherlands ; Oxford, United Kingdom ; Cambridge, MA, United States, second edition edition. OCLC: ocn992523631.

Lee, A. G., Beebe, D. J., and Palecek, S. P. (2012). Quantification of kinase activity in cell lysates via photopatterned macroporous poly(ethylene glycol) hydrogel arrays in microfluidic channels. *Biomedical Microdevices*, 14(2):247–257.

Letko, M., Marzi, A., and Munster, V. (2020). Functional assessment of cell entry and receptor usage for SARS-CoV-2 and other lineage B betacoronaviruses. *Nature Microbiology*, 5(4):562–569.

Levitt, M. and Park, B. H. (1993). Water: now you see it, now you don't. *Structure (London, England: 1993)*, 1(4):223–226.

Levy, Y. and Onuchic, J. N. (2006). WATER MEDIATION IN PROTEIN FOLDING AND MOLECULAR RECOGNITION. *Annual Review of Biophysics and Biomolecular Structure*, 35(1):389–415.

Little, D. J. and Kane, D. M. (2013). Measuring nanoparticle size using optical surface profilers. *Optics Express*, 21(13):15664.

Lombardi, J. R. and Birke, R. L. (2009). A Unified View of Surface-Enhanced Raman Scattering. *Accounts of Chemical Research*, 42(6):734–742.

Long, D. A. (2002). *The Raman effect: a unified treatment of the theory of Raman scattering by molecules*. Wiley, Chichester; New York. OCLC: 51955503.

Loudon, R. (1965). Theory of the resonance Raman effect in crystals. *Journal de Physique*, 26(11):677–683.

Love, J. C., Estroff, L. A., Kriebel, J. K., Nuzzo, R. G., and Whitesides, G. M. (2005). Self-Assembled Monolayers of Thiolates on Metals as a Form of Nanotechnology. *Chemical Reviews*, 105(4):1103–1170.

Lubrizolcdmo (2019). Protein Structure: Primary, Secondary, Tertiary, Quatenary Structures.

Manz, A., Graber, N., and Widmer, H. (1990). Miniaturized total chemical analysis systems: A novel concept for chemical sensing. *Sensors and Actuators B: Chemical*, 1(1-6):244–248.

Mariuzza, R. A., Phillips, S. E. V., and Poljak, R. J. (1987). The Structural Basis of Antigen-Antibody Recognition. *Annual Review of Biophysics and Biophysical Chemistry*, 16(1):139–159.

Masters, P. S., Kuo, L., Ye, R., Hurst, K. R., Koetzner, C. A., and Hsue, B. (2006). Genetic and Molecular Biological Analysis of Protein-Protein Interactions in Coronavirus Assembly. 581:163–173.

Mateo, C., Palomo, J. M., Fernandez-Lorente, G., Guisan, J. M., and Fernandez-Lafuente, R. (2007). Improvement of enzyme activity, stability and selectivity via immobilization techniques. *Enzyme and Microbial Technology*, 40(6):1451–1463.

McBride, R., van Zyl, M., and Fielding, B. (2014). The Coronavirus Nucleocapsid Is a Multifunctional Protein. *Viruses*, 6(8):2991–3018.

McCreery, R. L. (2000). *Raman spectroscopy for chemical analysis*. John Wiley & Sons, New York. OCLC: 43115053.

McNay, G., Eustace, D., Smith, W. E., Faulds, K., and Graham, D. (2011). Surface-Enhanced Raman Scattering (SERS) and Surface-Enhanced Resonance Raman Scattering (SERRS): A Review of Applications. *Applied Spectroscopy*, 65(8):825–837.

Metiu, H. and Das, P. (1984). The Electromagnetic Theory of Surface Enhanced Spectroscopy. *Annual Review of Physical Chemistry*, 35(1):507–536.

Michota, A., Kudelski, A., and Bukowska, J. (2001). Influence of electrolytes on the structure of cysteamine monolayer on silver studied by surface-enhanced Raman scattering. *Journal of Raman Spectroscopy*, 32(5):345–350.

Mikhonin, A. V., Ahmed, Z., Ianoul, A., and Asher, S. A. (2004). Assignments and Conformational Dependencies of the Amide III Peptide Backbone UV Resonance Raman Bands. *The Journal of Physical Chemistry B*, 108(49):19020–19028.

Mitsutake, H., Poppi, R., and Breitkreitz, M. (2019). Raman Imaging Spectroscopy: History, Fundamentals and Current Scenario of the Technique. *Journal of the Brazilian Chemical Society*.

Morens, D. M., Folkers, G. K., and Fauci, A. S. (2004). The challenge of emerging and re-emerging infectious diseases. *Nature*, 430(6996):242–249.

Moskovits, M. (1985). Surface-enhanced spectroscopy. *Reviews of Modern Physics*, 57(3):783–826.

mpbio (2021). Dimethyl sulfoxide, cell culture reagent.

Networks, T. (2021). Amino Acids – the Building Blocks of Proteins.

NIH (2020). Potent antibodies found in people recovered from COVID-19.

Noh, J. and Hara, M. (2002). Final Phase of Alkanethiol Self-Assembled Monolayers on Au(111). *Langmuir*, 18(6):1953–1956.

Nuzzo, R. G. and Allara, D. L. (1983). Adsorption of bifunctional organic disulfides on gold surfaces. *Journal of the American Chemical Society*, 105(13):4481–4483.

O'Dwyer, C., Gay, G., Viaris de Lesegno, B., and Weiner, J. (2004). The Nature of Alkanethiol Self-Assembled Monolayer Adsorption on Sputtered Gold Substrates. *Langmuir*, 20(19):8172–8182.

Otto, A. (2005). The 'chemical' (electronic) contribution to surface-enhanced Raman scattering. *Journal of Raman Spectroscopy*, 36(6-7):497–509.

Overbeek, C. A. (2008). Some Data on Emulsions of Steroid Hormones. In Wolstenholme, G. E. W., editor, *Novartis Foundation Symposia*, pages 254–262. John Wiley & Sons, Ltd, Chichester, UK.

Park, W.-H. and Kim, Z. H. (2010). Charge Transfer Enhancement in the SERS of a Single Molecule. *Nano Letters*, 10(10):4040–4048.

Parsa, H., Chin, C. D., Mongkolwisetwara, P., Lee, B. W., Wang, J. J., and Sia, S. K. (2008). Effect of volume- and time-based constraints on capture of analytes in microfluidic heterogeneous immunoassays. *Lab on a Chip*, 8(12):2062.

Petrone, P. M. and Garcia, A. E. (2004). MHC–Peptide Binding is Assisted by Bound Water Molecules. *Journal of Molecular Biology*, 338(2):419–435.

Physics, R. (2021). Laminar Flow vs. Turbulent Flow.

Pilot, Signorini, Durante, Orian, Bhamidipati, and Fabris (2019). A Review on Surface-Enhanced Raman Scattering. *Biosensors*, 9(2):57.

Poirier, G. E. (1997a). Characterization of Organosulfur Molecular Monolayers on Au(111) using Scanning Tunneling Microscopy. *Chemical Reviews*, 97(4):1117–1128.

Poirier, G. E. (1997b). Mechanism of Formation of Au Vacancy Islands in Alkanethiol Monolayers on Au(111). *Langmuir*, 13(7):2019–2026.

Poljak, R. J., Amzel, L. M., Avey, H. P., Chen, B. L., Phizackerley, R. P., and Saul, F. (1973). Three-Dimensional Structure of the Fab' Fragment of a Human Immunoglobulin at 2.8-A Resolution. *Proceedings of the National Academy of Sciences*, 70(12):3305–3310.

Poljak, R. J., Amzel, L. M., Chen, B. L., Phizackerley, R. P., and Saul, F. (1974). The Three-Dimensional Structure of the Fab' Fragment of a Human Myeloma Immunoglobulin at 2.0-A Resolution. *Proceedings of the National Academy of Sciences*, 71(9):3440–3444.

Porto, S. P. S. and Wood, D. L. (1962). Ruby Optical Maser as a Raman Source. *Applied Optics*, 1(S1):139.

Princeton (2021). Piranha Solutions.

Pro-Sci (2020). Antibody Structure and Properties.

Proscience (2020). What is an Epitope? | ProSci Inc.

Purcell, E. M. (1977). Life at low Reynolds number. *American Journal of Physics*, 45(1):3–11.

Putnam, F. W., Liu, Y. S., and Low, T. L. (1979). Primary structure of a human IgA1 immunoglobulin. IV. Streptococcal IgA1 protease, digestion, Fab and Fc fragments, and the complete amino acid sequence of the alpha 1 heavy chain. *The Journal of Biological Chemistry*, 254(8):2865–2874.

Quinn, P. J. and Wang, X., editors (2008). *Lipids in health and disease*. Number v. 49 in Subcellular biochemistry. Springer, London?] ; [New York. OCLC: ocn233788403.

Raman, C. V. and Krishnan, K. S. (1928). A New Type of Secondary Radiation. *Nature*, 121(3048):501–502.

Reverberi, R. and Reverberi, L. (2007). Factors affecting the antigen-antibody reaction. *Blood Transfusion*.

Robbiani.et.al (2020). Convergent antibody responses to SARS-CoV-2 in convalescent individuals. *Nature*, 584(7821):437–442.

Rodier, F., Bahadur, R. P., Chakrabarti, P., and Janin, J. (2005). Hydration of protein-protein interfaces. *Proteins: Structure, Function, and Bioinformatics*, 60(1):36–45.

Rusmini, F., Zhong, Z., and Feijen, J. (2007). Protein Immobilization Strategies for Protein Biochips. *Biomacromolecules*, 8(6):1775–1789.

Scaglione, F., Alladio, E., Damin, A., Turci, F., Baggiani, C., Giovannoli, C., Bordiga, S., Battezzati, L., and Rizzi, P. (2019). Functionalized nanoporous gold as a new biosensor platform for ultra-low quantitative detection of human serum albumin. *Sensors and Actuators B: Chemical*, 288:460–468.

Schreiber, F. (2000). Structure and growth of self-assembling monolayers. *Progress in Surface Science*, 65(5-8):151–257.

Sciencefacts (2015). Raman Spectroscopy.

Sela-Culang, I., Kunik, V., and Ofran, Y. (2013). The Structural Basis of Antibody-Antigen Recognition. *Frontiers in Immunology*, 4.

Sethu, P., Sin, A., and Toner, M. (2006). Microfluidic diffusive filter for apheresis (leukapheresis). *Lab Chip*, 6(1):83–89.

Sharp, K., Adrian, R., Santiago, J., and Molho, J. (2005). *Liquid flows in microchannels*, pages 10–1–10–46. CRC Press.

Sheehan, P. E. and Whitman, L. J. (2005). Detection Limits for Nanoscale Biosensors. *Nano Letters*, 5(4):803–807.

Shipp, D. W., Sinjab, F., and Notingher, I. (2017). Raman spectroscopy: techniques and applications in the life sciences. *Advances in Optics and Photonics*, 9(2):315.

Siamwiza, M. N., Lord, R. C., Chen, M. C., Takamatsu, T., Harada, I., Matsuura, H., and Shimanouchi, T. (1975). Interpretation of the doublet at 850 and 830 cm $^{-1}$ in the Raman spectra of tyrosyl residues in proteins and certain model compounds. *Biochemistry*, 14(22):4870–4876.

Simpson, P. C., Roach, D., Woolley, A. T., Thorsen, T., Johnston, R., Sensabaugh, G. F., and Mathies, R. A. (1998). High-throughput genetic analysis using microfabricated 96-sample capillary array electrophoresis microplates. *Proceedings of the National Academy of Sciences*, 95(5):2256–2261.

Sinobiological (2020). Antibody Structure and Function | Sino Biological.

Smekal, A. (1923). Zur Quantentheorie der Dispersion. *Die Naturwissenschaften*, 11(43):873–875.

Smith, E. and Dent, G. (2005). *Modern Raman spectroscopy: a practical approach*. J. Wiley, Hoboken, NJ.

Smith, G. P., McGoverin, C. M., Fraser, S. J., and Gordon, K. C. (2015). Raman imaging of drug delivery systems. *Advanced Drug Delivery Reviews*, 89:21–41.

Squires, T. M., Messinger, R. J., and Manalis, S. R. (2008). Making it stick: convection, reaction and diffusion in surface-based biosensors. *Nature Biotechnology*, 26(4):417–426.

St John, A. and Price, C. P. (2014). Existing and Emerging Technologies for Point-of-Care Testing. *The Clinical Biochemist. Reviews*, 35(3):155–167.

Stadler, K., Masignani, V., Eickmann, M., Becker, S., Abrignani, S., Klenk, H.-D., and Rappuoli, R. (2003). SARS–beginning to understand a new virus. *Nature Reviews. Microbiology*, 1(3):209–218.

Steward, M. W. (1984). Antibody—antigen interaction. In *Antibodies*, pages 37–66. Springer Netherlands, Dordrecht.

Teplyakov, A., Obmolova, G., Malia, T. J., Luo, J., Muzammil, S., Sweet, R., Almagro, J. C., and Gilliland, G. L. (2016). Structural diversity in a human antibody germline library. *mAbs*, 8(6):1045–1063.

Thermofisher (2008). Thermo Scientific - US.

To, K. K., Chan, J. F., Tsang, A. K., Cheng, V. C., and Yuen, K.-Y. (2015). Ebola virus disease: a highly fatal infectious disease reemerging in West Africa. *Microbes and Infection*, 17(2):84–97.

Trilling, A. K., Hesselink, T., Houwelingen, A. v., Cordewener, J. H., Jongsma, M. A., Schoffelen, S., Hest, J. C. v., Zuilhof, H., and Beekwilder, J. (2014). Orientation of llama antibodies strongly increases sensitivity of biosensors. *Biosensors and Bioelectronics*, 60:130–136.

Tripp, J. H. (1998). Rough Surface Characterization. In Bhushan, B., editor, *Tribology Issues and Opportunities in MEMS*, pages 135–148. Springer Netherlands, Dordrecht.

Tsuneda, T., Iwasa, T., and Taketsugu, T. (2019). Roles of silver nanoclusters in surface-enhanced Raman spectroscopy. *The Journal of Chemical Physics*, 151(9):094102.

Turrell, G. and Corset, J. (1996). *Raman microscopy: developments and applications*. Academic Press, London. OCLC: 1204723127.

Ulman, A. (1996). Formation and Structure of Self-Assembled Monolayers. *Chemical Reviews*, 96(4):1533–1554.

van Oss, C. J. (2000). Nature of Specific Ligand-Receptor Bonds, in Particular the Antigen-Antibody Bond. *Journal of Immunoassay*, 21(2-3):109–142.

Verdecchia, P., Cavallini, C., Spanevello, A., and Angeli, F. (2020). The pivotal link between ACE2 deficiency and SARS-CoV-2 infection. *European Journal of Internal Medicine*, 76:14–20.

Verma, S. P. and Wallach, D. F. (1977). Raman spectra of some saturated, unsaturated and deuterated C18 fatty acids in the HCH-deformation and CH-stretching regions. *Biochimica et Biophysica Acta (BBA) - Lipids and Lipid Metabolism*, 486(2):217–227.

Vítek, P., Novotná, K., Hodaňová, P., Rapantová, B., and Klem, K. (2017). Detection of herbicide effects on pigment composition and PSII photochemistry in Helianthus annuus by Raman spectroscopy and chlorophyll a fluorescence. *Spectrochimica Acta Part A: Molecular and Biomolecular Spectroscopy*, 170:234–241.

Wadman, M., Couzin-Frankel, J., Kaiser, J., MatacicApr. 17, C., 2020, and Pm, . (2020). How does coronavirus kill? Clinicians trace a ferocious rampage through the body, from brain to toes.

Wang, Z., Zong, S., Wu, L., Zhu, D., and Cui, Y. (2017). SERS-Activated Platforms for Immunoassay: Probes, Encoding Methods, and Applications. *Chemical Reviews*, 117(12):7910–7963.

Watson, J. D., editor (2014). *Molecular biology of the gene*. Pearson, Boston, seventh edition edition.

Weatherall, D. J. (2011). The Specificity of Serological Reactions by KarlLandsteiner (1936), Charles C. Thomas, Springfield, Illinois. *The FASEB Journal*, 25(8):2513–2514.

Wen, Z. (2007). Raman spectroscopy of protein pharmaceuticals. *Journal of Pharmaceutical Sciences*, 96(11):2861–2878.

WHO (2020). Technical guidance publications.

Wikipedia (2020a). Hydrogen bond.

Wikipedia (2020b). Inelastic scattering. Page Version ID: 976265625.

wikipedia (2020a). Microfluidics. Page Version ID: 994643695.

wikipedia (2020b). Phosphate-buffered saline. Page Version ID: 993088751.

wikipedia (2020c). Reynolds number. Page Version ID: 991265974.

Wikipedia (2020). Surface plasmon resonance. Page Version ID: 977836558.

wikipedia (2021a). Acetone. Page Version ID: 1000348707.

wikipedia (2021b). Fick's laws of diffusion. Page Version ID: 997658386.

wikipedia (2021c). Isopropyl alcohol. Page Version ID: 998265586.

wikipedia (2021d). Purified water. Page Version ID: 1000274717.

Wikipedia (2021). Rhodamine 6G. Page Version ID: 1000211516.

Williams, R. W. (1986). [14] Protein secondary structure analysis using Raman amide I and amide III spectra. In *Methods in Enzymology*, volume 130, pages 311–331. Elsevier.

WITec (2020). Knowledge Base || WITec Raman Imaging.

Wu, W., Giese, R., and van Oss, C. (1994). Linkage between -potential and electron donicity of charged polar surfaces 1. Implications for the mechanism of flocculation of particle suspensions with plurivalent counterions. *Colloids and Surfaces A: Physicochemical and Engineering Aspects*, 89(2-3):241–252.

Xu, Z., He, Z., Song, Y., Fu, X., Rommel, M., Luo, X., Hartmaier, A., Zhang, J., and Fang, F. (2018). Topic Review: Application of Raman Spectroscopy Characterization in Micro/Nano-Machining. *Micromachines*, 9(7):361.

Yakovleva, J., Davidsson, R., Lobanova, A., Bengtsson, M., Eremin, S., Laurell, T., and Emnéus, J. (2002). Microfluidic Enzyme Immunoassay Using Silicon Microchip with Immobilized Antibodies and Chemiluminescence Detection. *Analytical Chemistry*, 74(13):2994–3004.

Yamada, R., Wano, H., and Uosaki, K. (2000). Effect of Temperature on Structure of the Self-Assembled Monolayer of Decanethiol on Au(111) Surface. *Langmuir*, 16(13):5523–5525.

Yin, Y. and Wunderink, R. G. (2018). MERS, SARS and other coronaviruses as causes of pneumonia. *Respirology (Carlton, Vic.)*, 23(2):130–137.

Zaat, J. (2004). World Health Report: WHO. The World Health Report 2004; changing history. Genève: WHO, 2004. 169 pagina's, $27,50. ISBN 92-4-156265-X. *Huisarts en Wetenschap*, 47(11):239–239.

Zhan, W., Seong, G. H., and Crooks, R. M. (2002). Hydrogel-Based Microreactors as a Functional Component of Microfluidic Systems. *Analytical Chemistry*, 74(18):4647–4652.

Zheng, Y. and Narayanaswamy, A. (2011). Lifshitz theory of van der Waals pressure in dissipative media. *Physical Review A*, 83(4):042504.

Zhong, F., Wu, Z., Guo, J., and Jia, D. (2018). Porous Silicon Photonic Crystals Coated with Ag Nanoparticles as Efficient Substrates for Detecting Trace Explosives Using SERS. *Nanomaterials*, 8(11):872.

Zhu, N., Zhang, D., Wang, W., Li, X., Yang, B., Song, J., Zhao, X., Huang, B., Shi, W., Lu, R., Niu, P., Zhan, F., Ma, X., Wang, D., Xu, W., Wu, G., Gao, G. F., Tan, W., and China Novel Coronavirus Investigating and Research Team (2020). A Novel Coronavirus from Patients with Pneumonia in China, 2019. *The New England Journal of Medicine*, 382(8):727–733.

Zhu, Z., Daniel, T. A., Maitani, M., Cabarcos, O. M., Allara, D. L., and Winograd, N. (2006). Controlling Gold Atom Penetration through Alkanethiolate Self-Assembled Monolayers on Au{111} by Adjusting Terminal Group Intermolecular Interactions. *Journal of the American Chemical Society*, 128(42):13710–13719.

A APPENDIX

A.1 SAFETY DATA SHEET FOR CYSTEAMINE HYDROCHLORIDE FROM SIGMA ALDRICH

The Safety data Sheet for Cysteamine Hydrochloride https://www.sigmaaldrich.com/MSDS/MSDS/DisplayMSDSPage.do?country=NL&language=EN-generic&productNumber=M6500&brand=SIGMA&PageToGoToURL=https%3A%2F%2Fwww.sigmaaldrich.com%2Fcatalog%2Fproduct%2Fsigma%2Fm6500%3Flang%3Den

A.2 SAFETY DATA SHEET FOR DSP FROM SIGMA ALDRICH

The Safety data Sheet for DSP extends from pages https://www.thermofisher.com/document-connect/document-connect.html?url=https%3A%2F%2Fassets.thermofisher.com%2FTFS-Assets%2FLSG%2FSDS%2FPG82082_MTR-EULT_BE.pdf&title=UEc4MjA4Mg==

A.3 SAFETY DATA SHEET FOR DMSO FROM SIGMA ALDRICH

The Safety data Sheet for DMSO extends from pages https://www.sigmaaldrich.com/MSDS/MSDS/DisplayMSDSPage.do?country=NL&language=EN-generic&productNumber=276855&brand=SIAL&PageToGoToURL=https%3A%2F%2Fwww.sigmaaldrich.com%2Fcatalog%2Fproduct%2Fsial%2F276855%3Flang%3Den

A.4 SAFETY DATA SHEET FOR GENETEX SARS-COV-2 ANTIBODY

The Safety data Sheet for the Genetex SARS-CoV-2 antibody extends from pages 105 to 107

SARS-CoV / SARS-CoV-2 (COVID-19) spike antibody [1A9]

Cat No. GTX632604

Host	Mouse
Clonality	Monoclonal
Isotype	IgG1
Application	WB, ICC/IF, IHC-P, FACS, IP, ELISA, sELISA, IHC-P (cell pellet)
Reactivity	SARS Coronavirus, SARS Coronavirus 2

Reference (12)

★★★★★ Review (9)

Package
100 µl, 25 µl

APPLICATION

Application Note

*Optimal dilutions/concentrations should be determined by the researcher.

Suggested dilution	Dilution
WB	1:500-1:3000
ICC/IF	1:100-1:2000
IHC-P	Assay dependent
FACS	Assay dependent
IP	Assay dependent
ELISA	Assay dependent
sELISA	Assay dependent
IHC-P (cell pellet)	Assay dependent

Note : Capture : GTX632604, Detection: GTX635654/GTX135356/GTX635672/GTX135386/GTX135360

Not tested in other applications.

Specificity/Sensitivity	This antibody detects both SARS-CoV spike and SARS-CoV-2 spike proteins (S2 subunit). Our internal testing indicates no cross-reactivity with MERS-CoV spike protein.

PROPERTIES

Form	Liquid
Buffer	PBS
Storage	Store as concentrated solution. Centrifuge briefly prior to opening vial. For short-term storage (1-2 weeks), store at 4°C. For long-term storage, aliquot and store at -20°C or below. Avoid multiple freeze-thaw cycles.
Concentration	1 mg/ml (Please refer to the vial label for the specific concentration.)
Immunogen	The immunogen used to generate this antibody corresponds to SARS-CoV S∆10 (within S2 domain) protein (1029-1192 a.a.).

GeneTex, Inc. (North America)
t-877-436-3839 (Toll-Free) t-949-305-2888 sales@genetex.com

GeneTex International Corporation (Global)
886-3-5208988 886-3-5208989 infoasia@genetex.com

GeneTex Datasheet

Purification	Affinity purified by Protein G.
Conjugation	Unconjugated
Note	For laboratory use only. Not for any clinical, therapeutic, or diagnostic use in humans or animals. Not for animal or human consumption.

DATA IMAGES

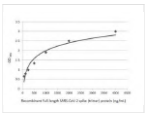

GTX632604 ELISA Image

Sandwich ELISA detection of recombinant full-length SARS-CoV-2 spike (trimer) protein using GTX632604 as capture antibody at concentration of 5 µg/mL and GTX635672 as detection antibody at concentration of 1 µg/mL. Rabbit IgG antibody (HRP) (GTX213110-01) was diluted at 1:10000 and used to detect the primary antibody.

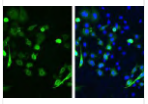

GTX632604 ICC/IF Image

SARS-CoV / SARS-CoV-2 (COVID-19) spike antibody [1A9] detects SARS-CoV-2 (COVID-19) spike protein by immunofluorescent analysis.
Sample: BHK-21 cells transfected with full-length SARS-CoV-2 spike were fixed in 4% paraformaldehyde at RT for 30 min.
Green: SARS-CoV-2 (COVID-19) spike stained by SARS-CoV / SARS-CoV-2 (COVID-19) spike antibody [1A9] (GTX632604) diluted at 1:2000.

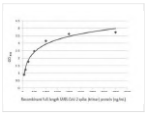

GTX632604 ELISA Image

Sandwich ELISA detection of recombinant full-length SARS-CoV-2 spike (trimer) protein using GTX632604 as capture antibody at concentration of 5 µg/mL and GTX635654 as detection antibody at concentration of 1 µg/mL. Rabbit IgG antibody (HRP) (GTX213110-01) was diluted at 1:10000 and used to detect the primary antibody.

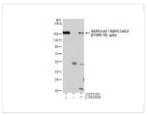

GTX632604 IP Image

Immunoprecipitation of SARS-CoV-2 Spike transfected 293T whole cell extracts using 2 µg of SARS-CoV / SARS-CoV-2 (COVID-19) spike antibody [1A9] (GTX632604).
Western blot analysis was performed using SARS-CoV / SARS-CoV-2 (COVID-19) spike antibody [1A9] (GTX632604).
EasyBlot HRP-conjugated anti mouse IgG antibody (GTX221667-01) was used to detect the primary antibody.

For full product information, images and publications, please visit our website.

GeneTex, Inc. (North America)
t-877-436-3839 (Toll-Free) t-949-305-2888 sales@genetex.com

GeneTex International Corporation (Global)
886-3-5208988 886-3-5208989 infoasia@genetex.com

© 2018 GeneTex Inc. All rights reserved.

B APPENDIX

B.1 RAMAN ACQUISITION PARAMETERS FOR SERS SUBSTRATE SAMPLE CHARACTERISATION

The Raman Acquisition details includes the setup information, calibrations and Noise filtering.

B.1.1 Setup Information

The setup windows allows for controlling the positioning stage of the Raman spectrometer with used of the marzhauser, the objective selected was the 50X, grating was set at 1800gr/mm, a neutral density filter of 0.1% was selected to avoid CCD saturation and the denaturation of the molecule physisorbed on the SERS substrate. The slit and hole were set to 1000 each for optimum spectral resolution, see Figure B.1.

The Acquisition parameter windows allowed for setting the range of the wavenumber to be investigated, an acquisition time of 30second and an accumulation of 2 was found to be optimum see Figure B.2.

The Acquisition options window allowed for setting a delay time of 1s, a binning factor of 1 and the spike filter to multiple accumulation. The binning factor of 1 means the full number of data points is used to create the spectrum, a higher binning factor reduces resolution and close peaks and other spectrum artifacts can be lost if set higher than 1.

The spike filter a sophisticated algorithm that help clears out unwanted and information-less spikes that appear in some spectral as a result of a cosmic ray event during measurement, for this filter to work well, the number of accumulations in the acquisition parameter window should be set to at least 2 and the spike filter set to multiple acquisition, see Figure B.3.

B.1.2 Calibrations

Calibration was done to ensure that the highest possible intensity is obtained during measurements. A Silicon substrate was placed on the sample stage and a laser light of wavelength 514nm focused on it, then the spectro entry box of the acquisition parameter window was set to $520.67cm-1$, which is the wavenumber location of a prominent peak in silicon Raman spectrum; the neutral density filter was set to 100% and the hole to 200, then a live Raman spectrum of the silicon was obtained at exactly this point, the hole was now set to 1000 with all other setting remaining same and another Raman spectrum of silicon obtained, since the spectrum was live, a knob behind the 514nm laser was used to adjust the Raman intensity of the $520.67cm-1$ to the highest possible. The ratio of the peaks at hole setting 1000 and 200 was always above 50, this was deemed appropriate by the manufacturer of the Raman Spectrometer.

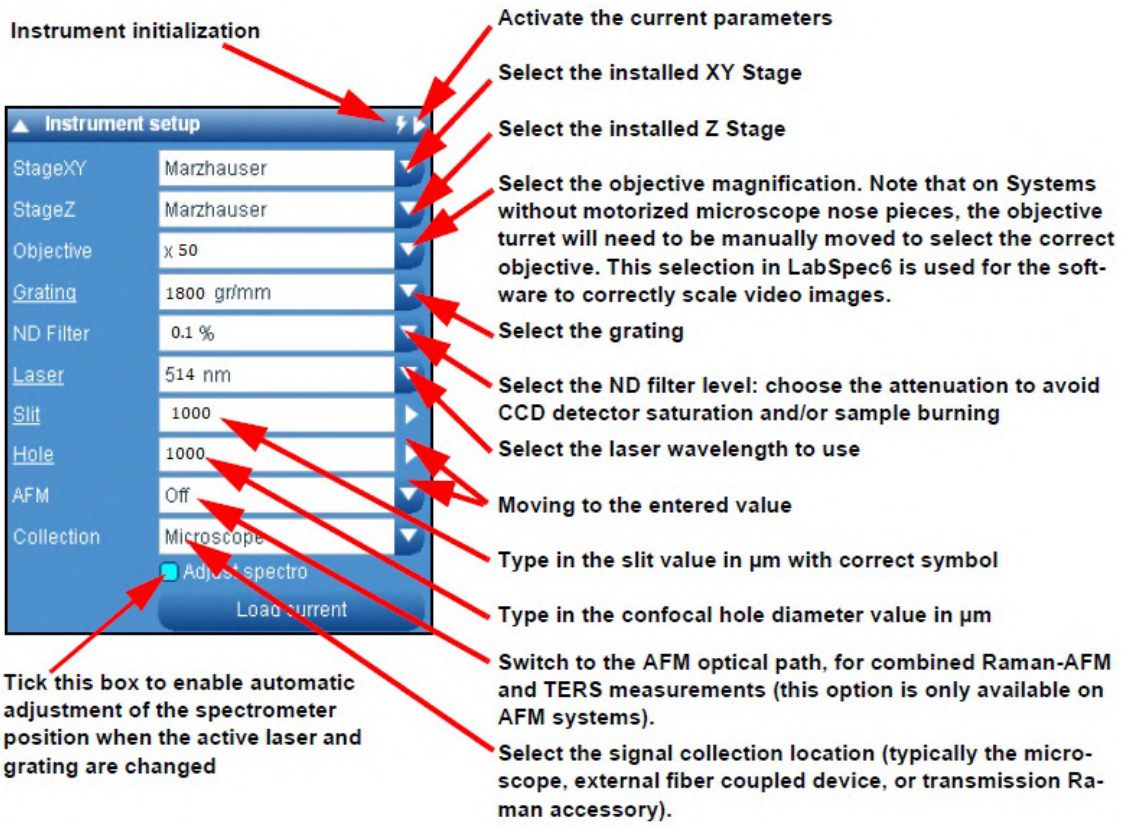

Figure B.1: The setup window of the Labspec software

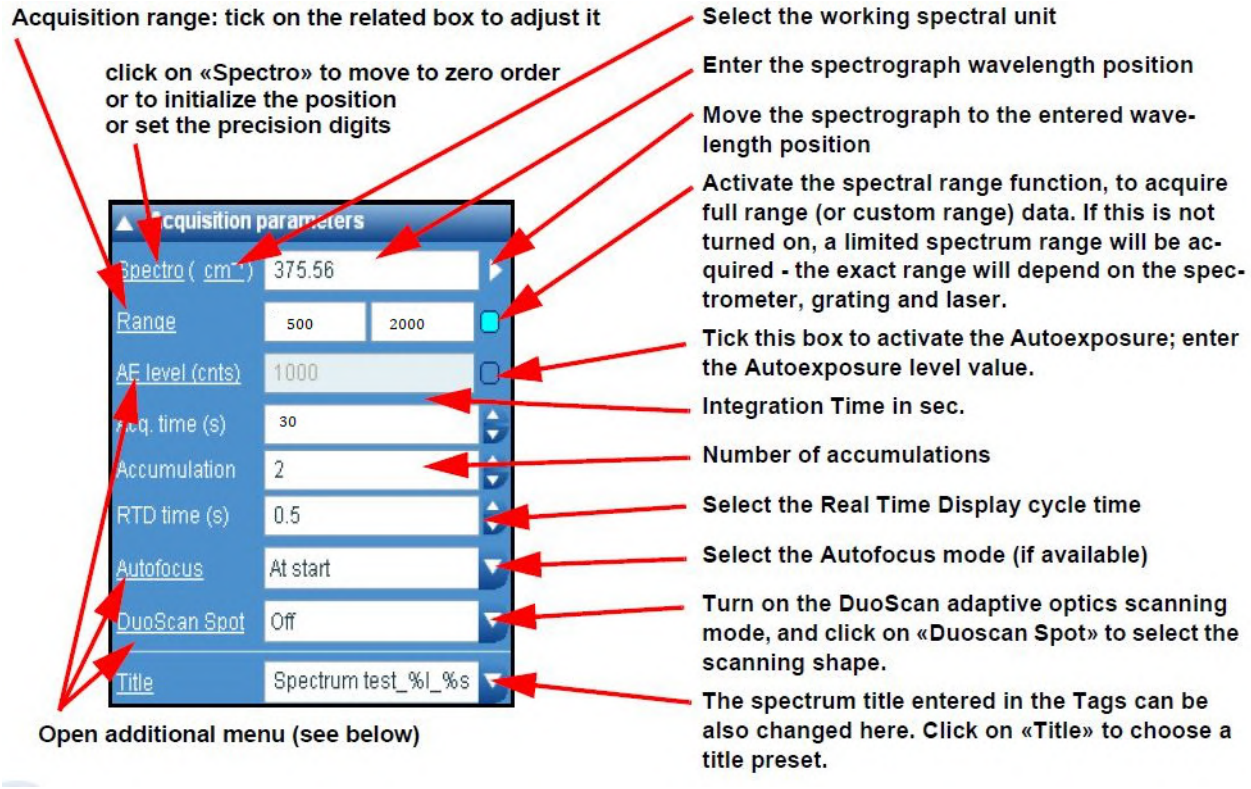

Figure B.2: The Acquisition parameter window of the Labspec software[HORIBA, 2017]

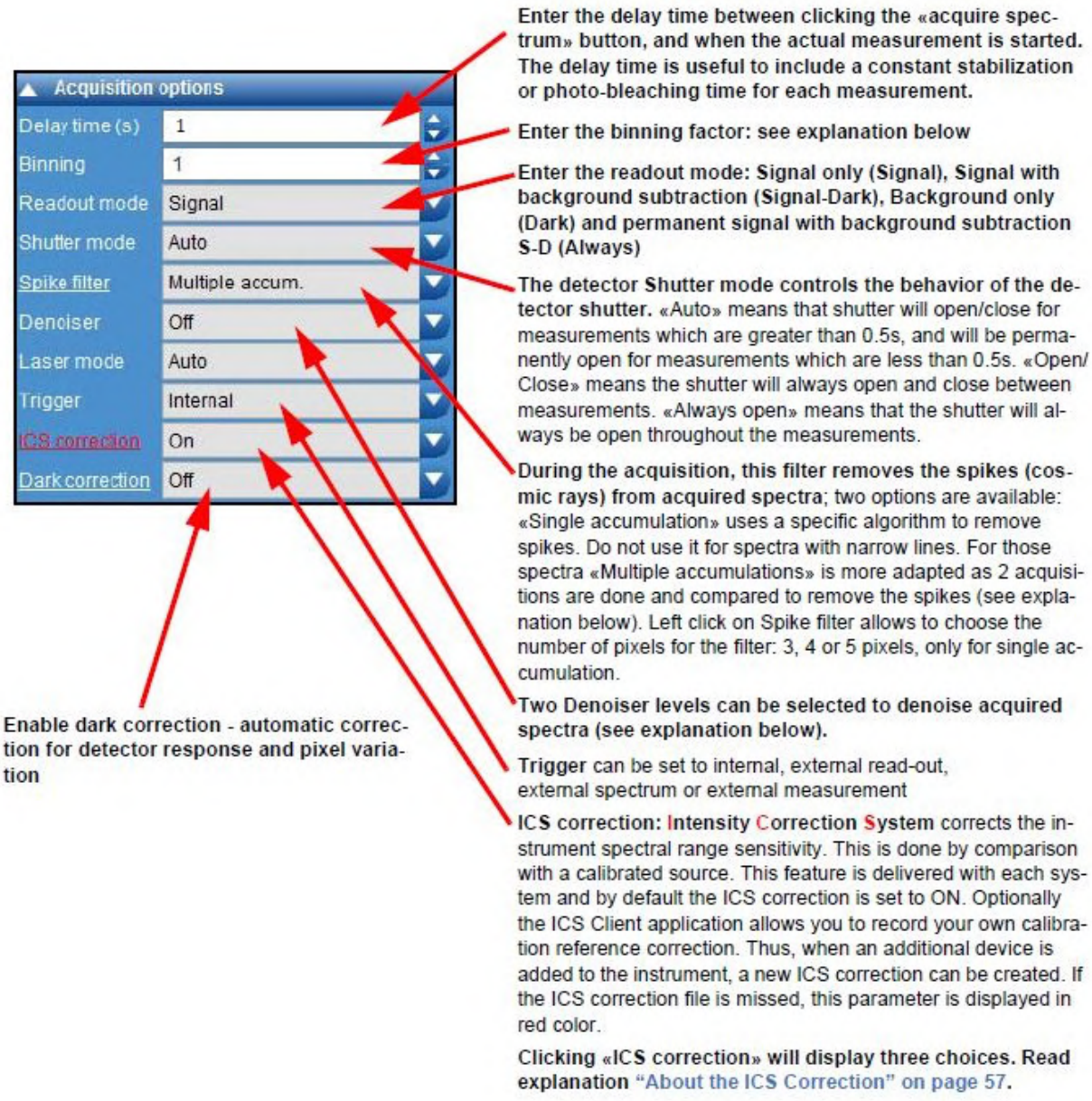

Figure B.3: The Acquisition Options window of the Labspec software[HORIBA, 2017]

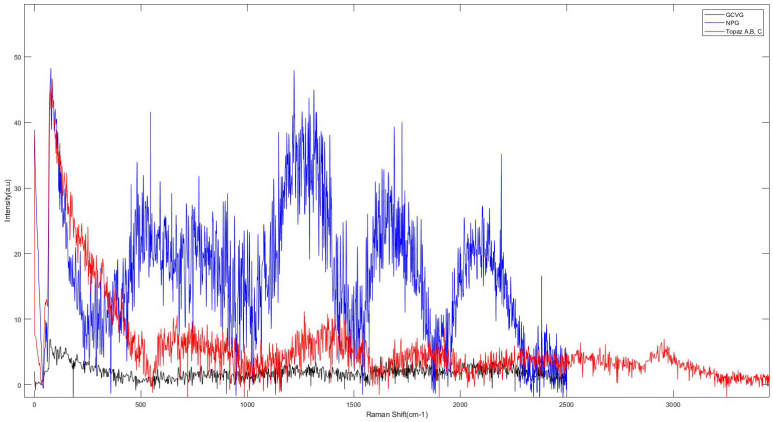

Figure B.4: Recorded Photoluminescence of GCVG, Gold nanoparticles on Topaz and NPG

B.1.3 Smoothing and Noise Filtering

Raw Spectral data obtained required smoothing and filtering to remove noise, to do this, filters employing various algorithms, namely, Savitzky-Golay, median and Fast fourier tranform used. Absolute care was taken to ensure that the smoothing and denoiseing process did not lead to any loss of spectral peaks.

Polynomial

The Polynomial filter utilises the Savitzky-Golay algorithm to fit polynomials of higher degrees through a range of sizes and replaces those pixels with polynomial curve.

Median Filter

The Median filter algorithm smooths spectrals by replacing a data point by the median of all data point in a given data window.

Fast Fourier Transform

The is based on a novel mathematically transformation, in this method a given spectrum is converted from the wavenumber domain to the frequency domain by Fourier transforms. In this process high frequencies are discarded and low frequencies retained. The de-noised spectrum is then converted by to the wavenumber for presentation.

B.1.4 Background Photoluminescence of Bare SERS Substrates

Bareground photoluminescence of both bare and functionalized SERS substrate were recorded so as to give an idea of the scattering capability of each substrate. For the functionalize substrate this photoluminescence was removed by baseline subtration using the LabSpec software.

The Raman measurement conditions for acquiring photoluminescence data was same as those for measurement with rhodamine 6G, from Figure B.4 the blue curve was obtained from the average of four measurements on nanoporous gold, the red curve was the average of 12 measurements from 4 different points on Topaz A, B and C, one curve is presented because all 12 spectrum data were very similar. Finally, the black curve represents the average data from four measurements on GCVG, for the GCVG substrate the photoluminscence is smaller.

B.2 WHITE LIGHT INTERFEROMETRY ACQUISITION PARA-METERS FOR SERS SUBSTRATE SURFACE CHARAC-TERISATION

In obtaining measurements, the vertical scanning interferometry (VSI) mode was used as described in Section 7.7. In this mode, the white light source is neutral density filtered, this ensures an appropriate coherence length of white light and the system measures the degree of interference fringe modulation.

System performance is quantified by range and resolution. Range is defined as the greatest vertical distance the profiler can accurately measure, for the VSI mode it is 2mm.[Little and Kane, 2013]

Resolution refers to the smallest lateral or vertical distance the Bruker surface profilometer can accurately measure.

Lateral resolution is a function of the magnification objective and the detector array size selected. For each magnification objective(2.5X and 20X) used.

Since VSI mode was used in all measurements, multiple measurements 3 pertime were average to get the final value. The averaging of multiple measurements lead to a resolution of less than 1nm.

B.2.1 Terms of Removal

Bruker Interferometer provides allows for the removal of characteristics(artefacts) that are either inherent in a sample or that are introduced due to the sloppiness of the sample stage. In the course of measurement, terms of removal was achieved via Tilt only and curvature tilt removal setup window.